



UNIVERSITY OF LEEDS

Numerical Simulations of Dusty Colliding Wind Binaries



Joseph Eatson
University of Leeds
School of Physics and Astronomy

Submitted in accordance with the requirements for the degree of

Doctor of Philosophy

January, 2022

This thesis is dedicated to my Mum, without her help these past 26 years there's
no way I would have gotten this far.

I'll pay you back I promise.

Acknowledgements

If you're reading this ahead of time and wondering where you are, don't worry, I'm getting to you, just writing the thesis first!

I suppose a good place to start when thanking people in a thesis is to start with family. To my mum, when I asked you to for help funding my doctoral degree, you said yes, instantly, and without hesitation, considering all you have done and sacrificed for me throughout my life, your agreeing to help was another act of kindness that I can barely repay (trust me, I've done the numbers). You've been there for me, every step of the way, I could not ask for a more wonderful mum, and I hope I can make you proud.

I also owe a debt to my supervisor, Dr. Julian Pittard, you've gone above and beyond when it came to my supervision, you've solved bugs, found mistakes and gotten me out of a jam more times in this project than I can count. I'm still amazed how you can rattle off a paper or three from memory, when I've come into your office asking questions about a very specific part of my work, honestly, how do you do that? It's very impressive.

No good thesis¹ wouldn't be complete without a commitment to the authors friends. I first met some of you on the literal first day of my undergraduate degree, it's really quite incredible how you've all tolerated my nonsense for so long. From essentially forcing my way into Rob's house so I could cook some disastrous fried chicken, to playing *Super Smash Bros.* all night long on its release day, to watching trashy movies over the internet at the height of a global pandemic, these are moments I'll treasure for the rest of my life. In particular, those who are still in Leeds, Rob, Matt, Kelsie, Alex and Sam; as well as those who aren't, Martin, Caz, Andy, and Devon. Thank you all, for filling my life with joy this past decade. To my partner Pruthvi, I cannot stress how unlikely it is that the two of us even met - two people finding and falling for each other on the more esoteric circles of the internet is like two particles colliding in the tenuous interstellar medium, if you'll excuse the extremely trite metaphor. You've been loving, kind, helpful, and the most wonderful partner anyone could ask for. I truly am blessed to know you and love you.

I would also like to thank the fantastic team at Leeds' ARC High Performance Computing department, considering the bulk of this work involves many 3D numerical simulations my use of ARC 4's compute nodes can be described as somewhere

¹Though the quality of this one is debatable.

from “excessive” to “taking the piss”. I also apologise for running my earlier simulations on the login nodes for multiple days, I swear it was an accident.

I would also like to thank two figures from my formative years for inspiring me. The first is my 9th year Physics teacher, Isobel Why, who re-kindled my interest in the field, she was the finest teacher I ever had, turning me from an underachieving student to a keen and committed aspiring physicist. She truly had faith in all of her students, and pushed them far beyond what they thought themselves capable of. Whilst she left teaching shortly after that year, I will never forget her impact on my life and my work. Another is quite indirect, but still important, I would be amiss to thank Winchell “Nyrath” Chung, curator of the website [Atomic Rockets](#). Winchell’s work is perhaps one of the most complete and exhaustive archive of real life and fictional rocketry and space exploration resources - whilst I haven’t called on his work much during my career in astrophysics, I pored over this website when I was younger (perhaps reading it more thoroughly than any of my course textbooks). It was fascinating, insightful and inspiring not only to me, but thousands of readers; the number of projects, from hard SFF novellas to honest-to-goodness research proposals hinge on his tireless efforts to catalogue humankind’s exploration of space in both reality and fiction. I learned of his cancer diagnosis whilst writing this thesis, and it cut me to my core, without his work I don’t think I would have turned a fascination with space into a lifelong passion. Thank you so much, both of you, you may not realise it, you may not ever read this, but you changed my life.

Finally, I would like to thank Leandro Panizzon and his wife, Margarita, though Methylphenidate was originally synthesised by him to treat her low blood pressure, it also works quite well for dragging my attention-deficit disorder riddled brain through this PhD.

Abstract

CONTENTS

1	Introduction & Motivation	1
1.1	Dust Formation in Colliding Wind Binary Systems	2
1.2	Motivation	2
1.3	Thesis Structure	2
2	Background	3
2.1	Early-Type Stars	4
2.1.1	OB-type stars	4
2.1.2	Wolf-Rayet stars	7
2.2	Stellar Winds	8
2.2.1	Stellar winds in low mass stars	9
2.2.2	Stellar winds in high mass stars	9
2.2.3	The CAK formalism	13
2.3	Interstellar Dust	13
2.3.1	The importance of interstellar dust	13
2.3.2	Interstellar dust in massive star systems	13
2.3.3	Radiation processes in interstellar dust	13
2.4	Colliding Wind Binary Systems	13
2.4.1	The Wind Collision Region	14
2.4.2	Cooling in the WCR	15
2.4.3	Dust formation in CWB systems	19
2.4.4	Important WCd systems	23
2.4.5	WR+WR systems	23
2.4.6	Contemporary research in extragalactic low-metallicity WCd systems . .	23

CONTENTS

3 Methodology & Numerical Simulation	25
3.1 The History & Mathematics of Numerical Simulations	26
3.2 The Purpose of Numerical Simulations	28
3.3 Computational Hydrodynamics	30
3.3.1 Comparison of hydrodynamical methods	30
3.3.2 The MG hydrodynamical code	30
3.4 The Athena++ hydrodynamical code	31
3.5 Mesh Refinement	33
3.6 Visualisation	35
3.7 Simulating CWB systems	36
3.7.1 Assumptions	36
3.7.2 Wind propagation & refinement	36
3.7.3 Cooling in numerical simulations	36
3.7.4 Model implementation	46
3.8 The BODMAS Adverted Scalar Dust Model	50
3.8.1 BODMAS features	50
3.8.2 Implementation	50
3.8.3 Contemporary dust Models	51
3.8.4 Future dust models	52
4 A Parameter Space Exploration of Dust Formation	55
4.1 Introduction	56
4.2 Methodology	58
4.2.1 Gas and dust cooling	61
4.2.2 Numerical modelling of dust through advected scalars	64
4.3 Model Parameters	67
4.3.1 Cooling mechanisms	67
4.3.2 Wind momentum ratio	68
4.3.3 Separation distance	70
4.3.4 Data collection	70
4.4 Results	71
4.4.1 Mass loss rate variation	77
4.4.2 Terminal velocity variation	77
4.4.3 Separation variation	81

CONTENTS

4.5	Conclusions	83
4.5.1	Wind mixing within the WCR	85
4.6	Summary	85
4.7	Acknowledgements	87
5	Hydrodynamical Simulation of WR140	89
5.1	Introduction	90
5.2	Methodology	91
5.2.1	Hydrodynamics	91
5.2.2	Dust model and cooling	93
5.2.3	Simulated systems	94
5.2.4	Radiative transfer modelling	96
5.3	Results	96
6	Influence of Wind Velocity on Dust Formation	101
6.1	Introduction	102
6.2	Methodology	102
6.3	Model Parameters	102
6.4	Results	102
7	Final Notes and Conclusions	105
7.1	Conclusions	106
7.1.1	Causes of dust formation in WCB systems	106
7.1.2	The role of eccentricity in dust formation	106
7.2	Future Study	106
7.2.1	More complex models	106
7.2.2	Further simulations of observed systems	106
7.2.3	Radiative transfer	106
7.2.4	WR+WR systems	106
7.2.5	Next generation telescopes	106
7.3	Other Observations	106
7.3.1	<i>How I Learned to Stop Worrying and Love Numerics</i>	106
7.3.2	Join the physics department, see the world	106
7.3.3	Paul Erdős was probably onto something	106
7.3.4	Carinae Strain: PhD research in a time of pandemic	106

CONTENTS

7.3.5	WR 104 as a local GRB candidate	106
7.3.6	Research software acknowledgements	106
A	Astrophysical Shocks	109
B	Software Carpentry	111
B.1	Amdahl’s Law	112
B.2	Version Control	112
	References	113

LIST OF FIGURES

2.1	Planck's law radiance comparison with resonance lines	11
2.2	M1-67 nebula around WR 124	12
2.3	ρ_w comparison of main sequence winds	14
2.4	WC & solar abundance plasma cooling curves	16
2.5	Dust cooling vs. plasma cooling	17
2.6	H_{el} and H_{coll} comparison	19
2.7	L' photometry of episodic dust making stars	22
2.8	Multiwavelength aperture synthesis image of WR98a	24
3.1	Initial conditions of a Riemann problem	26
3.2	Adaptive mesh refinement comparison	34
3.3	Comparison of dust and plasma cooling rates in post-shock environment	40
3.4	h_e integration accuracy comparison	41
3.5	Dust lookup table methods comparison	43
3.6	Electron transparency method accuracy - h_e	44
3.7	Electron transparency method accuracy - H_{el}/H_{coll}	45
3.8	Electron transparency method accuracy - Λ_d	45
3.9	Ionisation fraction for OB and WC stars	47
3.10	Cooling sub-step method evolution comparison	48
3.11	Cooling sub-step method accuracy comparison	50
3.12	Hendrix et al. (2016) synthetic astronomy	54
4.1	Static mesh refinement example	60
4.2	WR and OB $\Lambda(T)$ cooling curves	63
4.3	OB and WR electron-ion ratios	64

LIST OF FIGURES

4.4	Comparison of electron transparency methods	65
4.5	Comparison of threshold values for over-density method	72
4.6	Comparison of dust formation rates with cooling methods	73
4.7	Comparison of dust and plasma cooling rates in post-shock environment	73
4.8	Instabilities due to cooling	74
4.9	Density comparison of simulations with differing radiative processes	75
4.10	Temperature comparison of simulations with differing radiative processes	76
4.11	Baseline simulation z , full extent	76
4.12	Dust production rate for simulations varying mass loss rate	77
4.13	Comparison of dust production rate for simulations varying wind terminal velocity	78
4.14	Dust density comparison of terminal velocity varying systems	80
4.15	OB terminal velocity wind dust comparison	81
4.16	Wind colour comparison of $\eta = 0.04$ winds	82
4.18	Dust formation rate versus binary separation distance	84
4.19	A comparison of the structures of simulations varying d_{sep}	84
4.20	Wind mixing due to radiative methods	86
5.1	Orbital path comparison	95
5.2	χ change over system orbit	97
5.3	Density plot of WR140 periastron passage	98
5.4	Dust density plot of WR140 periastron passage	99

LIST OF TABLES

2.1	Stellar wind comparison	13
2.2	Cooling processes at various temperature ranges	15
2.3	Numer of confirmed WCd systems	20
2.4	Wind properties of systems simulated in this thesis.	23
2.5	Orbital properties of systems simulated in this thesis.	23
3.1	Dust cooling calculation comparison	46
3.2	Cooling method accuracy comparison	51
3.3	Cooling method performance comparison	51
4.1	Abundances used for OB and WR stars	62
4.2	Wind properties of the baseline system.	67
4.3	Baseline system orbital properties.	67
4.4	Cooling series simulation parameters	68
4.5	Mass loss rate series wind parameters	69
4.6	Terminal velocity series wind parameters	69
4.7	Parameters of simulations varying separation distance.	70
4.8	Rates of dust production for radiative simulation set.	75
4.9	Rates of dust production for mass loss rate simulation set.	78
4.10	Rates of dust production for terminal velocity simulation set.	83
4.11	Rates of dust production for separation distance set.	83
5.1	Parameters for the WR140 system	95
5.2	Parameters for the WR140 system	95
6.1	WR parameters	103

LIST OF TABLES

6.2 OB parameters	104
-----------------------------	-----

Abbreviations

List of common abbreviations, if an abbreviation is important enough to warrant a section in this thesis, the section will be referenced.

BODMAS	Binary Orbit Dust Model with Accretion and Sputtering	Section 3.8
CWB	Colliding Wind Binary	Section 2.1.1
GMC	Giant Molecular Cloud	Section 2.1.1
LBV	Luminous Blue Variable	Section 2.1.1
OB	O or B type star	Section 2.1.1
RSG	Red Supergiant	Section 2.1.1
WC	WR Carbon Phase	Section 2.1.2
WCd	Dust forming WC star	Section 2.4.3
WCR	Wind Collision Region	Section 2.4.1
WN	WR Nitrogen Phase	Section 2.1.2
WO	WR Oxygen Phase	Section 2.1.2
WR	Wolf-Rayet	Section 2.1.2

Common Symbols

List of common symbols, if symbol requires a derivation, the appropriate equation within this thesis will be referenced. If the symbol is a unit, the value in CGS units will be provided instead.

a	Grain radius	
C	Courant-Friedrichs-Lowy condition	
h_e	Electron transparency	Section 2.4.2
H_{coll}	Grain heating rate due to ions	
H_{el}	Grain heating rate due to electrons	
L_*	Stellar luminosity	
M_*	Stellar mass	
\dot{M}	Mass loss rate	
v_∞	Wind terminal velocity	
z	Dust-to-gas mass ratio	
β	Electron ion ratio	
η	Wind momentum ratio	
$\Lambda(T)$	Plasma Cooling function	
$\Lambda_d(h, a, T)$	Dust cooling function	
ξ	Grain sticking efficiency	
θ_c	WCR conic opening angle	Equation 2.10
τ_{KH}	Kelvin-Helmholtz timescale	Equation 2.1a
τ_{ff}	Free-fall timescale	Equation 2.1b
τ_{cool}	Cooling timescale	Equation 2.11a
τ_{esc}	Escape timescale	Equation 2.11b
μ	Mean molecular mass	
κ	Sub-timestep fraction	3.15
χ	Cooling parameter	Equation 2.12

M_{\odot}	Solar mass	1.988×10^{33} g
$M_{\odot} \text{ yr}^{-1}$	Solar mass per year	6.301×10^{25} g s $^{-1}$
L_{\odot}	Solar Luminosity	3.828×10^{33} erg s $^{-1}$
AU	Astronomical Unit	1.496×10^{13} cm
pc	Parsec	3.086×10^{18} cm
“warm”	Warm temperature regime	Between 10^4 and 10^5 K, personally

LIST OF TABLES

CHAPTER 1

Introduction & Motivation

1. INTRODUCTION & MOTIVATION

1.1 Dust Formation in Colliding Wind Binary Systems

1.2 Motivation

1.3 Thesis Structure

CHAPTER 2

Background

2. BACKGROUND

2.1 Early-Type Stars

The term Early-type stars is quite possibly the epitome of bad naming conventions in astrophysics, it's a very old term, coming from the dawn of astrophysics itself, quite opaque as to what it means, and also by definition *completely wrong*. In fact it is one of the most wrong pieces of terminology I can think of.¹ The first generation of astrophysicists found themselves asking very important questions such as “what even *are* stars?” and “what possible mechanism can allow a star to burn for so long?” Each of these questions was rather pressing for the burgeoning field, and the scientific community was aching for an answer.

Of course, like all pressing questions of the 19th century, it fell to Lord Kelvin to provide a convincing but incorrect answer. Kelvin assumed that gravitational collapse was the mechanism for a stars long-term heating, with younger, “early” type stars shining the brightest. Not only was the mechanism incorrect, but typically older main sequence stars are more luminous than their younger counterparts of a similar mass! However, as is the case with astrophysical terminology, the term stuck, to the confusion of many young astrophysicists.

Instead, we now know that stars produce their energy through fusion. These reactions vary from sub-stellar deuterium and lithium burning, to main sequence p-p & CNO hydrogen burning processes, and finally to the triple- α and other exotic fusion processes for evolved massive stars. The more massive the star the greater the internal pressure, allowing for more exotic fusion processes. The bigger a star, the greater the core pressure and temperature, as all fusion reactions are highly dependent on temperature, stars with only a few dozen solar masses are thousands of times more luminous than our sun, but only live a fraction of the time (Carroll & Ostlie, 2014).

2.1.1 OB-type stars

And with that we shift our gaze to high-mass stars, with the most massive of all being the O and B type stars, these are extremely luminous ($\sim 10^4 L_\odot$), and relatively short lived (~ 10 Myr) stars. The age-old adage of a candle burning twice as bright lasting half as long applies to our studies of the cosmos, but it is more apt to compare a candle and a stick of dynamite when

¹Aside from astrophysicists calling something “warm”, of course. That can quite literally mean anything from 10 to 10,000 Kelvin, depending on who you ask, what they’re writing about, or how they’re feeling at that particular moment. In fact, I’ll probably end up falling into this same trap somewhere in this thesis as well!

2.1 Early-Type Stars

considering stars on opposing ends of the Harvard classification system.

The most common formation mechanism of stars is through the collapse of a giant molecular cloud¹, an enormous cool cloud many parsecs across with a mass of around $10^4 M_\odot$. As this GMC collapses and radiates energy, lowering the radius of thermostatic equilibrium for the cloud, as collapsing progresses the cloud fragments into many smaller regions with a critical density, capable of collapsing further, forming a star. The collapse of a GMC can be described with a series of timescale. First, the Kelvin-Helmholtz timescale, τ_{KH} , which describes the timescale required for the radiating cloud to collapse. The second important timescale is the free-fall timescale, τ_{ff} , which is the time taken for a cloud to collapse. These timescales are described by the following equations:

$$\tau_{KH} \approx \frac{GM_*^2}{R_*L_*}, \quad (2.1a)$$

$$\tau_{ff} = \sqrt{\frac{3\pi}{32G\rho}}, \quad (2.1b)$$

where M_* is the protostellar mass, R_* is the protostellar radius, L_* is the protostellar luminosity, and ρ is the mean density of the collapsing cloud (Ward-Thompson & Whitworth, 2011).

Perhaps the most important distinction between massive star formation and its better understood counterpart is as a young protostar approaches the main sequence, the KH timescale is less than the free-fall timescale, meaning the material at the center of the collapsing cloud begins fusion while the bulk of core has collapsed onto the site of the future star. This burgeoning star begins to drive the weakly gravitationally coupled collapsing material away due to its sheer luminosity, driving this material outwards, causing it to accrete and shock material within the GMC.

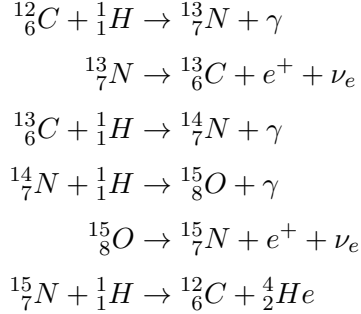
Another important consideration is the role of angular momentum as the star collapses. The particularly massive cloud involved in massive star formation is more prone to fragmentation, meaning that massive stars typically form with an orbital partner, whilst approximately 2/3^{rds} of low-mass stars are part of a binary or multiple system, this value is near-total. As such, the environment within an OB association after star formation consists of numerous young stars in

¹GMC

2. BACKGROUND

tightly-knit groups disrupting the entire local area.¹

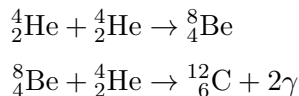
Above a stellar mass of $1.3M_{\odot}$ pressures and temperatures within a stellar core favour the fusion of hydrogen into helium through the catalytic CNO cycle, instead of the more direct p-p fusion process.



The reaction rate of CNO rises much faster, resulting in a convective core, surrounded by a radiative envelope (Salaris & Cassisi, 2005). This is the driving force behind the incredible luminosities of an OB star as it hurtles along the main sequence.

Unfortunately for massive stars, pesky fundamental laws such as the conservation of energy come into play. With only an order of magnitude or two of additional mass more than our sun and shining 10^4 times as brightly, this curtails the life of the brightest stars to lifespans not much more than 10^7 years. If we define a galactic year as the time it takes for a star to orbit the Milky Way, these poor stars don't even make it to their first birthdays, which is quite sad really.²

As the available hydrogen begins to become depleted, the lowering reaction rates force the star to shrink, this raises the internal temperature until the core begins to burn helium through the triple- α process:



¹This is a bit like living in Headingley, Hyde Park, or any other area with lots of Undergraduates.

²Continuing this analogy our sun can drink, might have voted if they felt like it, and may be racking up vast quantities of student debt.

The sudden spike in energy radiating from the core shifts the calculus of hydrostatic equilibrium in the favour of outward forces, causing the star to rapidly expand in the form of a Red Supergiant or Luminous Blue Variable (Ryan & Norton, 2010). During this phase the energy output of the star is even greater, with a timescale of $\sim 10^6$ years, this is only temporarily prolonging the life of the star, which will inevitably begin burning heavier and heavier elements, faster and faster. Once the star starts producing iron its fate is sealed, the star stops fusing, and collapses, annihilating itself in the form of a supernova and leaving behind a remnant of its core in the form of a neutron star or black hole (Ward-Thompson & Whitworth, 2011).

Whilst the stars end is as inevitable as it is violent, the intermediate stage as the star leaves the main sequence is in itself extremely interesting, and for the context of this thesis, no product of this stage is more interesting than the Wolf-Rayet.

2.1.2 Wolf-Rayet stars

As we now know, Wolf-Rayets¹ are evolved forms of O-type stars, and are a short lived component of the life-cycle of massive stars, typically lasting for around 5×10^5 years (Crowther, 2007). Despite this relatively transient length of this stage, the influence of a WR star on its local medium is extremely outsized. WR stars in particular are known for having dense, fast winds, typically between 2 and 3 orders of magnitude than their main sequence O-type progenitors, with mass loss rates on the order of $10^{-5} M_{\odot} \text{ yr}^{-1}$ and wind velocities of $1.5 \times 10^3 \text{ km s}^{-1}$. This extremely dense wind is driven by the highly energetic helium burning core, which is luminous enough as to drive away the outer layers of the stars envelope, exposing the core. The observed spectroscopic lines are due to heating of the envelope from the core, which is enriched with by-products of hydrogen and helium burning, the lack of hydrogen lines is due to the stars evolved nature, as all the hydrogen has been burned, there is simply nothing left to observe!

Wolf-Rayet stars can be subcategorised through spectroscopic observation, which indicates enrichment in a particular element, the 3 major sub-types, WN, WC and WO are defined by their strong nitrogen, carbon and oxygen lines respectively. The important distinction between WN and WC/WO stars is that WN stars are enriched through hydrogen burning, whilst WC and WO are enriched through the by-products of helium burning (Vink, 2015).

As a Wolf-Rayet continues to lose its envelope, additional products of fusion processes are

¹Abbreviated to WR.

2. BACKGROUND

dredged up from the centre of the star. In the case of the WN sub-type, the broad nitrogen lines correspond to the outer layer of the envelope, enriched through the CNO process; after this outer envelope is cast off, the remainder of the envelope exhibits carbon and oxygen lines, indicating enrichment from the triple- α process. Finally, the star evolves further and the innermost region of the envelope is revealed, observed as the strong oxygen lines of a WO sub-type (Neugent & Massey, 2019; Oswalt & Barstow, 2013).

As an O-type star transitions to a Wolf-Rayet, it typically undergoes an intermediary LBV or RSG stage as helium burning begins, this is mass dependent, with the various transitional states described by Crowther, 2007:

$$O \rightarrow LBV/RSG \rightarrow WN(H\text{-poor}) \rightarrow WC \rightarrow SN\ 1b, \text{ for } 25 M_{\odot} < M_{WR} < 40 M_{\odot}$$

$$O \rightarrow LBV \rightarrow WN(H\text{-poor}) \rightarrow WC \rightarrow SN\ 1c, \text{ for } 40 M_{\odot} < M_{WR} < 75 M_{\odot}$$

$$O \rightarrow WN(H\text{-rich}) \rightarrow LBV \rightarrow WN(H\text{-poor}) \rightarrow WC \rightarrow SN\ 1c, \text{ for } M_{WR} > 75 M_{\odot}$$

Wolf-Rayet stars are important in the context of this work due to their outsized influence within a WR+OB binary pair. The WR component of a WR+OB binary has an outsized contribution in returning material to the ISM, whilst also dominating the dynamics of the system, with their winds completely overpowering those of their O-type neighbours. In some cases, the dense, fast wind from the WR can collide with the much more tenuous wind from its partner, forming a strong shock, and a variety of fascinating effects. However, I wouldn't want to spoil too much too soon, but you can skip ahead to section 2.4, where this phenomena is covered in more detail.

2.2 Stellar Winds

Stellar winds have already been discussed to some extent in the previous section, however, due to the significance of winds within this body of work, further detailing of winds must be discussed to gain a better understanding of the dynamics of Colliding Wind Binary systems. This section will cover in brief the study of stellar winds, particularly driving mechanisms from low and high mass stars.

The study of stellar winds is of course, rather hard from our vantage point on Earth, as direct observation of a non-stellar solar wind is difficult, and sampling of the winds themselves

significantly more difficult than that due to the inconvenient distances involved in interstellar travel. Because of this, extrasolar wind properties are derived from spectrography, with velocities derived through Doppler shift. The important parameters to consider in a wind, especially for this thesis, is the mass loss rate, \dot{M} , the wind terminal velocity, v^∞ and the abundances within the wind.

$$\frac{dM}{dt} = 4\pi\rho(\mathbf{r})v(\mathbf{r})\mathbf{r}^2, \quad (2.5)$$

$$\rho_w = \frac{\dot{M}}{4\pi v^\infty r^2}, \quad (2.6)$$

This section will cover the different driving mechanisms winds from low and high mass stars, the typical wind parameters and driving mechanisms are broken down in table 2.1.

2.2.1 Stellar winds in low mass stars

Low mass stellar main sequence stellar winds are quite paltry for an astrophysical phenomenon, the sun, for instance, drives thin, comparatively slow winds, with a mass loss rate of $\sim 10^{-14} M_\odot \text{ yr}^{-1}$ and a terminal velocity of 400 km s^{-1} . The mechanism behind this is gas pressure from coronal heating, with outward pressure driving gas within stellar atmosphere away from the star, this results in a transonic wind that quickly reaches its terminal velocity as the coronal temperature and subsequent pressure quickly drops off.

As a low mass star exits the main sequence, ballooning in size to become a red giant, the density of the stellar wind increases dramatically.

As dust condenses in the upper atmosphere of the red giant, these grains can readily adsorb photons, utilising radiation pressure to be driven away from the more luminous giant star, easily achieving escape velocity against the low surface gravity of the red giant. Gas is also driven away, coupled to the dust, this provides an efficient form of momentum transfer, allowing for an extremely dense albeit slow stellar wind

2.2.2 Stellar winds in high mass stars

In the same way that high-mass stars are many orders of magnitude brighter than their low mass counterparts despite a comparatively low increase in mass, the same can be said of the

2. BACKGROUND

density of stellar wind. A main sequence OB star typically has a mass loss rate of $10^8 \text{ M}_\odot \text{ yr}^{-1}$, 6 orders of magnitude higher than a solar mass star. This discrepancy in wind density cannot be explained by stronger coronal heating, in fact, the lack of a convective envelope ensures that coronal heating is not even feasible as a driving method! Instead we must look towards the higher luminosities that massive stars exhibit to find a suitable mechanism.

Simple radiation pressure from these stars would not be enough to explain the observed dense, highly supersonic winds emanating from these massive stars.

Resonance lines were also considered, a photon with an energy equal to the excitation energy of an ion is absorbed by that ion, gaining the momentum of this ion. The ion subsequently de-excites over a timescale on the order of 10^{-8} s , emitting a photon at a random angle relative to the radial direction, α . The resultant change in radial velocity, Δv_r , for the adsorption of a photon at the resonance frequency ν_0 is

$$\Delta v_r = v''_r - v_r = \frac{\hbar\nu_0}{mc}(1 - \cos\alpha), \quad (2.7)$$

where v''_r is the radial velocity after the absorption and emission events, and m is the ion mass. These ions are accelerated away from the star, along with the rest of the stellar wind which is coupled through Coulomb forces. The opacity of such resonance lines can be up to six orders of magnitude larger than the opacity of a Thomson scattering event (Lamers & Cassinelli, 1999). Additionally, this effect is not observed in low-mass stars, whose spectra typically peak in the visible light, while resonance lines typically have energies equivalent to UV photons (figure 2.1). O-type stars and Wolf-Rayets, however, emit much of their radiation within the UV range.

Early computations involving resonance lines from Lucy and Solomon, 1970 provided a more reasonable mass loss rate calculation, but were still off by approximately two orders of magnitude. Building off of the work by Lucy & Solomon, a vital paper in the solidification of radiative lines as the main driving mechanism behind massive star outflows was produced by Castor, Abbott and Klein¹. The CAK formalism calculated reasonably close wind velocities, while being accurate to within a factor of 3 for mass loss rates (Castor et al., 1975). Further work allowed for more accurate computations of the line driving effect, such as the mCAK prescription, the Sobolev approximation and the finite disk correction factor (Pauldrach et al., 1986).

As previously mentioned, evolved massive stars progress into a helium burning WR phase,

¹Hereafter abbreviated as CAK.

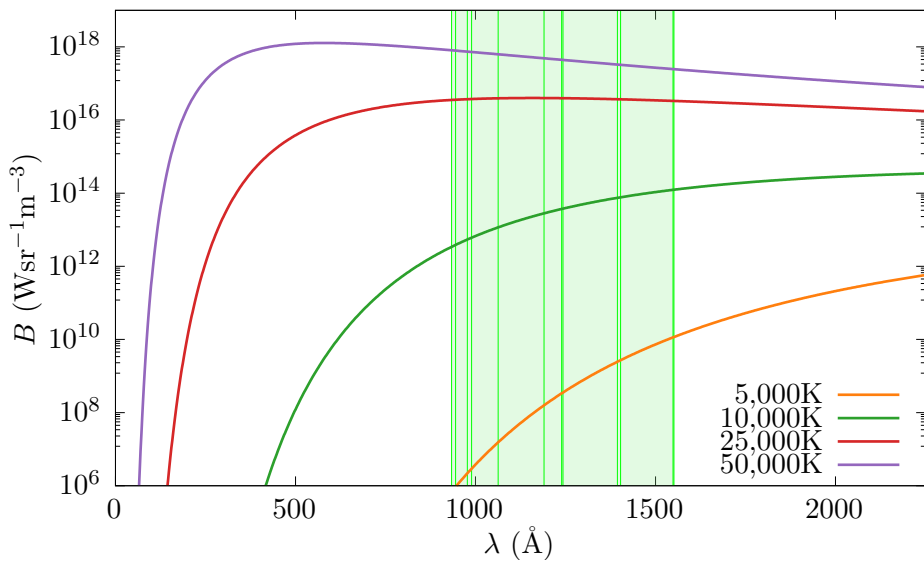


Figure 2.1: Spectral radiance against wavelength for black body objects at various effective temperatures, T_{eff} , a series of wavelengths corresponding with important resonance lines in table 1 of Lucy and Solomon, 1970 have been included. As temperature increases the spectral radiance at resonance line wavelengths dramatically increases, with a minimum of 6 orders of magnitude difference between the effective temperatures of a solar equivalent main sequence star and an O-type main sequence or Wolf-Rayet star.

2. BACKGROUND

at this point, mass loss rates due to radiative line driving are extreme, in the order of $10^{-5} M_{\odot} \text{ yr}^{-1}$. This outsized influence on the local medium can be seen in the production of ejecta nebula, such as M1-67 produced by WR 124 (figure 2.2).



Figure 2.2: Reduced Hubble WFPC2 data of the WN star WR 124, its extreme mass loss is currently producing the ejecta nebula M1-67 (Marchenko et al., 2010).

Star	\dot{M}	v_∞	Mechanism
	$M_\odot \text{ yr}^{-1}$	km s^{-1}	
Sun	10^{-14}	400	Thermal heating
Pre Main Sequence	$10^{-4} - 10^{-7}$	200-500	Rotation & magnetic fields
Red Giant	$10^{-7} - 10^{-9}$	30	Radiation pressure on dust grains
OB Star	$10^{-7} - 10^{-8}$	2500	Radiation pressure & line driving
Wolf-Rayet	10^{-5}	1500	Radiation pressure & line driving

Table 2.1: Comparison winds emitted from various types of star.

2.2.3 The CAK formalism

2.3 Interstellar Dust

2.3.1 The importance of interstellar dust

2.3.2 Interstellar dust in massive star systems

2.3.3 Radiation processes in interstellar dust

2.4 Colliding Wind Binary Systems

Colliding Wind Binaries¹, in opposition to all known laws of astrophysical nomenclature, is a easy to understand term - it is a binary system where stellar winds from the member stars undergoing collision. Unfortunately, the simplicity of the systems ends here, CWB systems are extremely complex and poorly understood as they are difficult environments to observe or simulate.

Early observations beyond visual spectrum led to the discovery of many new astrophysical phenomena, one such discovery were extremely bright persistent thermal x-ray sources, with x-ray The first classification and analysis of Colliding Wind Binary systems were independently performed by Prilutskii and Usov, 1976 and Cherepashchuk, 1976, these systems were found to contain a close binary system, consisting of an evolved WR star and an OB counterpart, as their winds collide, a strong shock forms, heating the winds to temperatures in the order of 10^8 K in

¹Abbreviated to CWBs.

2. BACKGROUND

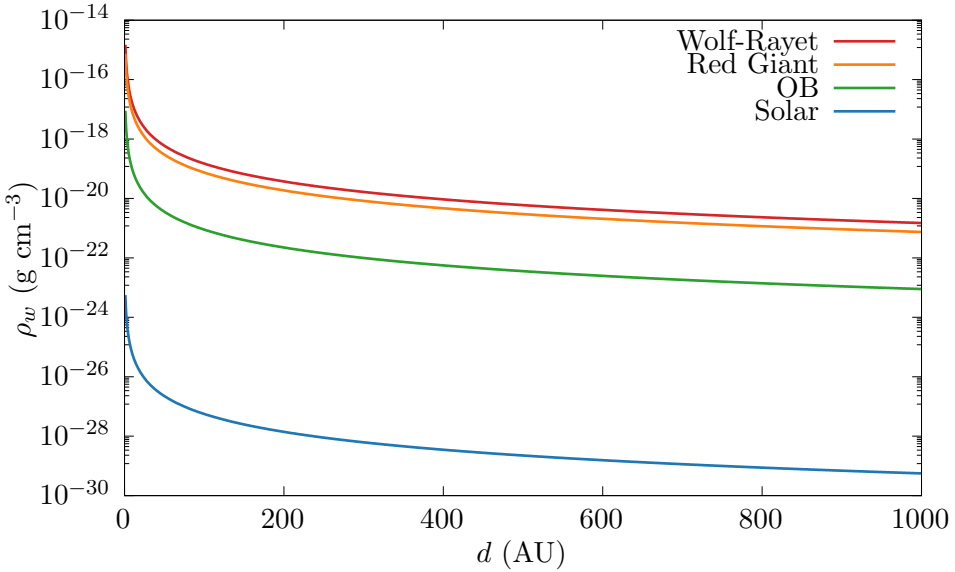


Figure 2.3: Comparison of the densities of various main sequence winds using the parameters specified in table 2.1, wind densities are estimated using the smooth wind approximation described in equation 2.6.

the immediate post-shock environment, these extreme temperatures and the large quantity of shocked material accounted for the extremely bright thermal x-ray emission. The evidence was further compounded as the variation of the x-ray flux could be attributed to orbital motion of these binary systems.

2.4.1 The Wind Collision Region

The Wind Collision Region¹ is the most violent and turbulent region of a CWB system, a region where strong shocks lead to temperatures in excess of 10^8 K. These strong shocks contain enormous amounts of mechanical energy, in the region of $10^3 L_\odot$, WCRs are engines capable of producing huge quantities radiation through multiple thermal and non-thermal mechanisms (Eichler & Usov, 1993; Grimaldo et al., 2019). Despite these extreme conditions, these regions are capable of producing amorphous carbon dust grains at a rate on the order $1 \times 10^{-8} M_\odot \text{ yr}^{-1}$. As these grains are extremely fragile, this is a conundrum that has plagued researchers in this field, as direct observation of the innermost regions of even nearby WCRs is difficult, bordering

¹WCR

on impossible, much of the work in this area involves hydrodynamical simulation.

The properties of the WCR can be described by a small number of parameters. The first of such parameters is the wind momentum ratio, η , which describes the available (Usov, 1991).

$$\eta = \frac{\dot{M}_{\text{OB}} v_{\infty}^{\text{OB}}}{\dot{M}_{\text{WR}} v_{\infty}^{\text{WR}}}, \quad (2.8)$$

This momentum ratio can also be used to estimate the distance of the apex of the WCR to each star, using the following equations:

$$r_{\text{WR}} = \frac{1}{1 + \eta^{1/2}}, \quad r_{\text{OB}} = \frac{\eta^{1/2}}{1 + \eta^{1/2}}, \quad (2.9)$$

where r_{WR} is the distance from the WR star to the WCR apex, and r_{OB} is the distance from the OB star to the WCR apex. Work by Eichler and Usov, 1993 goes further to utilise the momentum ratio to approximate the shape of the wind collision region, further out from the apex of the WCR, the region forms an approximately conical shape with an opening angle, θ_c of:

$$\theta_c \simeq 2.1 \left(1 - \frac{\eta^{2/5}}{4} \right) \eta^{-1/3}, \quad \text{for } 10^{-4} \leq \eta \leq 1, \quad (2.10)$$

2.4.2 Cooling in the WCR

Temperature range	Dominant process	Spectral region
$5 \times 10^3 \text{ K} \lesssim T \lesssim 1 \times 10^5 \text{ K}$	Forbidden lines	IR, Optical
$T \approx 1 \times 10^5 \text{ K}$	H excitation/ionisation	Optical, UV
$5 \times 10^3 \text{ K} \lesssim T \lesssim 1 \times 10^5 \text{ K}$	Resonance lines	Far UV, soft X-ray
$T \gtrsim 1 \times 10^8 \text{ K}$	Bremsstrahlung	Radio

Table 2.2: Breakdown of dominant cooling processes at various temperature ranges from Dyson, 2021, whilst H excitation/ionisation occurs over a very short temperature range, it is extremely influential, causing a global peak in the cooling rate at $\approx 10^5$ K. These temperature ranges are depicted in figure 2.4.

2. BACKGROUND

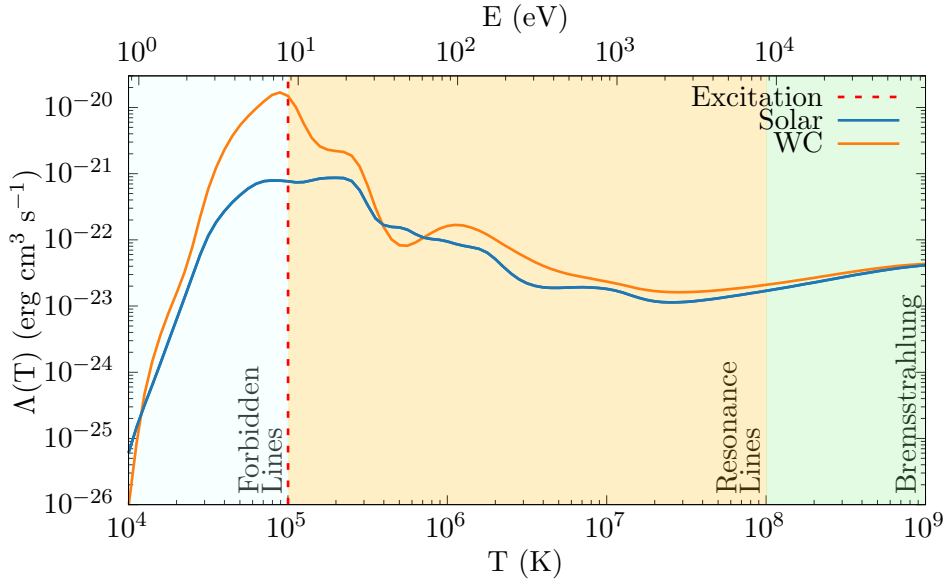


Figure 2.4: Normalised plasma cooling rates as a function of temperature and thermal energy for solar abundance and WC abundance winds. The regions where forbidden line, resonance line and bremsstrahlung emission are dominant are highlighted, with H ionisation and recombination occurring between the forbidden and resonance line sections at 10^5 K.

Cooling due to radiation emission in a hot plasma can be broken down into a variety of processes that occur over series of temperature ranges. Ions inside a plasma can become excited through collisions or photon absorption resulting in emission of photons as the ions de-excited.

Mechanisms that are significant within the warm¹ and hot gas phases include forbidden line emission, hydrogen excitation and ionisation, resonance lines and bremsstrahlung, the influence of each mechanism waxes and wanes as temperature increases, with each mechanism clearly dominant over (Dyson, 2021).

The first mechanism to be discussed is forbidden line emission². This process dominates the cooling process of cooler gas that is not fully ionised, where collisions with free electrons excite metals within the gas, causing them to de-excite through photon emission through these

¹See what I mean about the phrase “warm”?

²Like many other phenomena discussed in this thesis, this too is a misnomer, while initially assumed to be prohibited under the contemporary understanding of atomic physics, it is in fact just astrophysicists jumping the gun again.

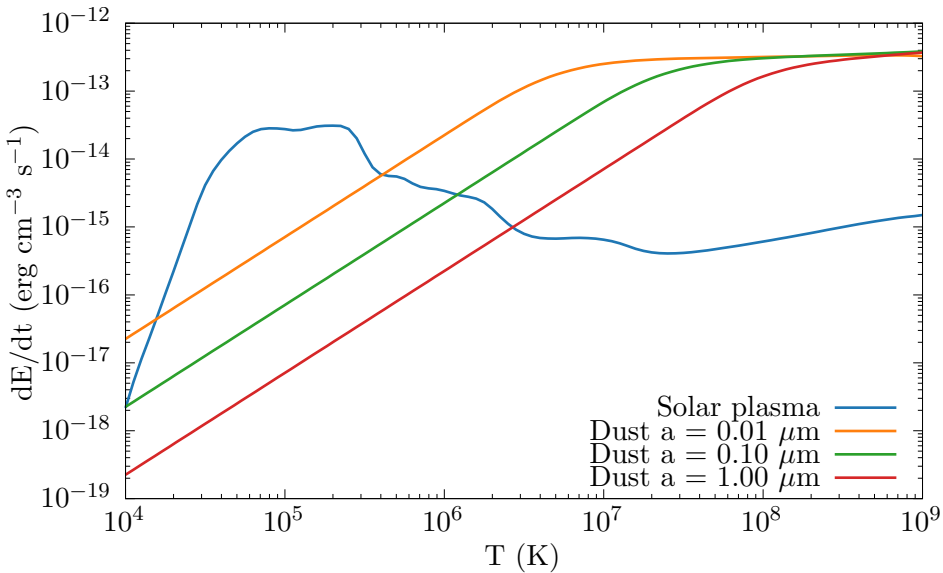


Figure 2.5: Comparison of plasma cooling to dust cooling with different grain sizes in a solar abundance gas, where $\rho_g = 10^{-20} \text{ g cm}^{-3}$ and a dust-to-gas mass ratio of 0.01.

forbidden lines. Forbidden lines themselves arise from magnetic dipole and quadrupole fine structure states within typical energy levels, despite having a much lower probability of occurring compared to conventional energy level transitions. This process dominates at these temperatures as the transition energies are significantly lower, on the order of 1 eV, as the photon is also of a comparatively long wavelength, it can more easily escape from the gas without being re-absorbed by it.

As the temperature increases there is a spike in the cooling rate of the gas as the hydrogen present begins to fully ionise, at this temperature a hydrogen ion and an electron may recombine, releasing a cascade of photons as the electron de-excites.

As the plasma heats further resonance lines can

As the particle energy reaches the range of tens of keV, bremsstrahlung¹ becomes dominant (figure 2.4). High velocity electrons are deflected by ions, emitting radiation in the process due to conservation of energy.

(Schure et al., 2009) (Rybicki & Lightman, 2004)

¹Or braking radiation when you can't remember how to spell it.

2. BACKGROUND

$$\tau_{\text{cool}} = \frac{k_B T_s}{4n_w \Lambda(T_s)}, \quad (2.11a)$$

$$\tau_{\text{esc}} = \frac{d_{\text{sep}}}{c_s}, \quad (2.11b)$$

$$\chi = \frac{\tau_{\text{cool}}}{\tau_{\text{esc}}} \approx \frac{v_{\infty,8}^4 d_{\text{sep},12}}{\dot{M}_{-7}}, \quad (2.12)$$

The presence of dust within the immediate post-shock environment significantly increases the cooling rate. Figure 2.5 compares rate of cooling due to dust emission of various types of grains to plasma cooling at solar abundances, As Λ_g and Λ_D are both proportional to ρ_g^2 , dust cooling will dominate at high temperatures so long as there is sufficient amounts of dust.

As dust grains collide with ionised gas and electrons, this imparts kinetic energy into the grains, heating them and causing them to emit infrared radiation. Assuming that there is a net accretion of ions and electrons onto the dust grains and the gas is optically thin in the infrared regime, energy is efficiently removed from the gas. At particularly high temperatures this effect can dominate over high-temperature plasma cooling processes such as bremsstrahlung, as seen in figure 2.5. Figure 2.6 compares dust grain heating rates due to electron and ion collisional excitation in a solar abundance and WC abundance flow. At lower temperatures the dust grain cooling rate is dominated by electron excitation, especially in the WC case as the ratio of free electrons to ions is significantly higher, as the WC flow is enriched by heavier elements. However, as the grain temperature increases, collisional heating due to ions becomes more prevalent as the electrons are sufficiently energetic to pass through the grain without significant energy transfer; this is referred to as the electron transparency, h_e (Dwek & Werner, 1981).

Work by Dwek and Werner, 1981 is used predominantly in this project to simulate cooling due to dust, a fast method for calculating the cooling rate due to dust was integrated into the numerical code for this project, which is elaborated on in section 3.7.3.

The heating rate of a dust grain due to collisions

$$H_{\text{coll}} = n\pi a^2 \langle Q(E, q, U) \rangle \times \langle v(E - qU) f(a, E - qU) f(a, E - qU) \rangle \text{ erg s}^{-1} \quad (2.13)$$

This can be simplified and expressed in the equation:

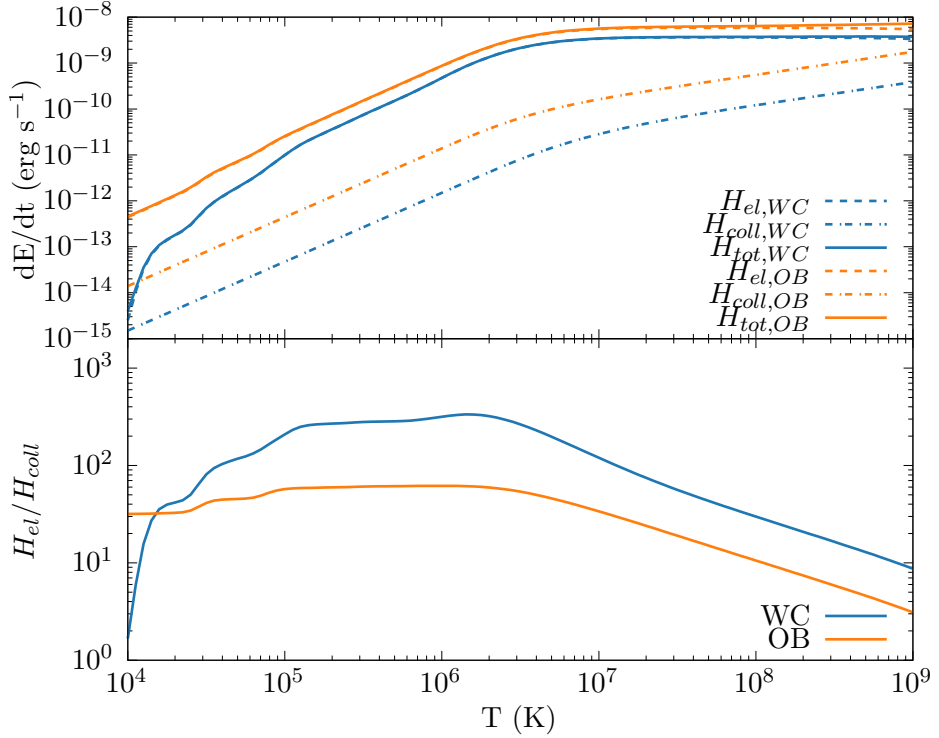


Figure 2.6: Comparison of grain heating rate due to ion collisional excitation, H_{coll} , and electron excitation, H_{el} . The dust grain has a grain radius of $5 \times 10^{-3} \mu\text{m}$ and is travelling through a gas with a density of $10^{-20} \text{ g cm}^{-3}$ with solar and WC abundances.

$$\begin{aligned}
 H_{coll} &= \left(\frac{32}{\pi m} \right)^{1/2} n \pi a^2 (k_B T)^{3/2} h(a, T) \\
 &= 1.26 \times 10^{-19} \frac{n}{A^{1/2}} a^2 (\mu\text{m}) T^{3/2} h(a, T) \text{ erg s}^{-1}
 \end{aligned} \tag{2.14}$$

2.4.3 Dust formation in CWB systems

Despite the extremely violent conditions thus far described in CWB systems, these systems appear to be extremely prolific producers of interstellar dust. Whilst single star WC systems can produce small amounts of dust in the form of amorphous carbon grains (though this could be observed to be extremely rare, pending the results of Medina et al. (2021)), binary systems have been observed to convert up to 10^{-3} of their wind masses from ionised carbon into

2. BACKGROUND

	Persistent		Variable		Episodic	
	Total	Example	Total	Example	Total	Example
WC4	1	WR19	0	—	0	—
WC5	0	—	0	—	1	WR47C
WC6	1	WR124-10	0	—	0	—
WC7	3	WR102-22	0	—	4	WR140
WC8	6	WR13	1	WR48a	3	WR122-14
WC9	45	WR104	6	WR98a	1	WR75-11
Total	56		7		9	

Table 2.3: Number of confirmed WCd systems with known spectral type and dust formation type from the Galactic Wolf Rayet Catalogue (Rosslowe & Crowther, 2015), systems with uncertain spectral types not included, while systems labelled “d” are included within the “persistent” category for their associated spectral type.

amorphous carbon dust grains, this results in a typical dust production rate of $10^{-8} M_{\odot} \text{ yr}^{-1}$, on part with a typical Asymptotic Giant Branch (AGB) star. This dust forming behaviour has only been observed in particularly energetic WC stars (predominantly WC9, with some WC7-8 examples), WN and WO systems have not been observed producing dust, this is most likely due to amorphous grains being significantly more chemically stable and resilient to effects such as sublimation and photoevaporation than water ice or silicate grains (Draine & Salpeter, 1979; Salpeter, 1977). Dust formation is also observed to form within the WCR, which can form quite beautiful pinwheel-shaped patterns, as dust streams away from the stars in the post-shock outflow.

Whilst beautiful, they are sadly an elusively rare beauty... The Galactic Wolf Rayet Catalogue¹ (Rosslowe & Crowther, 2015) has a collection of 667² known galactic WR stars, 106 of such stars are contained within a binary system, with 41 such binaries containing WC stars. Rosslowe and Crowther (2015) notes that there are a total of 42 confirmed WCd systems, approximately 35% of all WC systems, though this value is somewhat out date and includes single star systems. A more up-to-date estimate performed for this thesis using the updated dataset estimates a total of 80 WCd systems, of which 72 have well-determined spectral subtypes (table 2.3). Rosslowe and Crowther (2015) goes on to estimate that out of an estimated total of

¹The most recent version of this catalogue is available at <http://pacrowther.staff.shef.ac.uk/WRcat>

²At time of writing, with the last update being August 2020.

2.4 Colliding Wind Binary Systems

1900 galactic WR stars, approximately 300 of these stars are predicted to be dusty WC stars. Whilst this is a far cry from the number of galactic AGB stars - of which carbon-rich AGBs outnumber WCd stars by approximately 3 orders of magnitude (Ishihara et al., 2011) - these systems can still significantly impact the surrounding interstellar medium, with strong stellar feedback propagating large quantities of dust into the surrounding medium.

Table 2.3 contains an excerpt of the observed WCd systems with clearly defined spectral subtypes, most dust producing stars are either WC8 or WC9 subtypes, which are markedly cooler and less luminous than their WC4 counterparts. This reduced luminosity is potentially the driving factor for dust formation in the system. As WC8-9 systems have slower, cooler winds (Niedzielski & Skorzyński, 2002), they are more strongly influenced by post-shock cooling, allowing for greater dust formation within the WCR. A small number of these systems have somewhat variable or episodic dust production cycles, such as WR98a and WR140, which are the two systems being observed within this thesis. Furthermore, the bulk of WCd systems do appear to be in binary systems with a close periastron passage, in fact, this orbit itself appears to be a driving force behind how dust is produced in these systems, as we will later discuss.

A good starting point to understanding dust formation is to understand how the WCR can mitigate the mechanisms resulting in dust destruction, whilst aiding the processes involved in dust formation. As previously discussed, dust can be destroyed through high-velocity collisions with grains, as well as evaporation through heating or ionising radiation. These processes are mitigated through the cooling, as well as the high level of UV extinction due to the high density of the WCR. Meanwhile, the dust production rate increases within high density regions, as collisions between dust grains and gas occur at a much higher rate. The same can be said with dust grains, allowing for fast growth from gas and impinging ion accretion, and grain-grain collision as the number density of dust grains begins to increase. The accumulation of these effects would be a very fast initial growth rate, which tapers off as the post-shock region diffuses and expands, resulting in a reduction in density.

The presence of instabilities driven by cooling and other factors can lead to pockets of high density post-shock material, as high density drives dust formation, this can lead to “clumps” of highly dust-enriched post-shock stellar wind. These clumps would have additional protection from UV photons, and would also be cooled enough for dust to form, thus, the driving hypothesis for this theory is that these are regions where the bulk of dust formation would occur. As such, it is theorised in order to achieve a high rate of dust formation, a dense, highly radiative post-

2. BACKGROUND

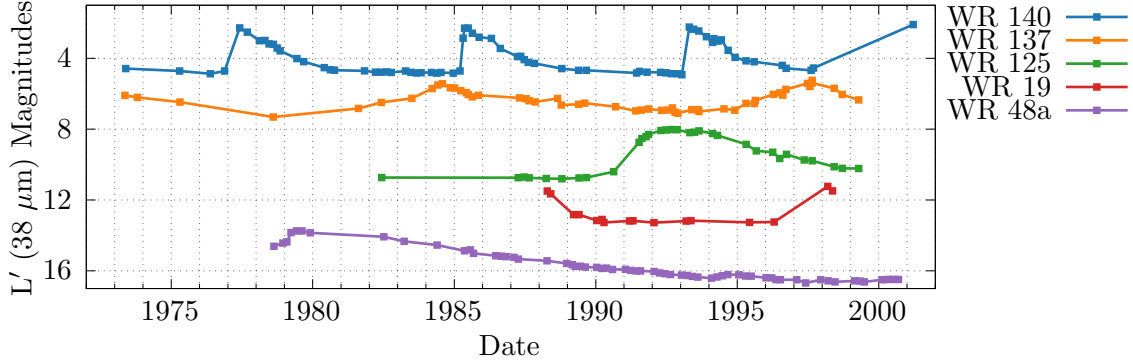


Figure 2.7: L' photometry for episodic dust making stars, data derived from Crowther (2003), and provided by PM Williams in private correspondence. WR 140 and WR 137 in particular have extremely predictable dust forming events which correspond to periastron passage in both systems.

shock WCR must be formed, as cooling in the post-shock region is dependent on separation distance, wind velocity and mass loss rate, these parameters should first be explored, with the knowledge gleaned used to direct an analysis of observed systems such as WR140.

Eccentricity appears to play an important factor in the production of dust, highly eccentric systems can vary their dust production rates significantly. Figure 2.7 shows the periodic change in mid-IR emission that can be explained as dust emission from small amorphous carbon grains, in the case of systems such as WR140 or WR125 dust production can be reduced to the point where associated emissions can drop by several magnitudes. This relation is clearly periodic, with a peak in dust production coinciding with the periastron passage of these systems. This implies that dust production is dependent on orbital separation, which will influence the degree of cooling occurring within the WCR, it could potentially also alter the wind velocity on collision, which will also influence dust production in the same manner. Further analysis of available dust producing CWB systems suggests that *all* WCd systems with circular orbits produce dust either persistently or with a degree of variability, while eccentric WCd systems are solely produce dust episodically.

2.4.4 Important WCd systems

The principle systems that are being observed in this thesis are the variable dust forming system, WR98a, and the episodic dust forming system WR140. The archetypal continuous dust forming system WR104 was also proposed for simulation, but had to be cut due to time constraints, this system will also be discussed to provide a point of comparison between the two systems.

System	\dot{M}_{WR} ($M_{\odot} \text{ yr}^{-1}$)	\dot{M}_{OB} ($M_{\odot} \text{ yr}^{-1}$)	v_{WR}^{∞} (km s^{-1})	v_{OB}^{∞} (km s^{-1})	η	χ_{\min}
WR 98a	5.0×10^{-6}	5.0×10^{-8}	900	2000	0.0222	0.7970
WR 104	3.0×10^{-5}	6.0×10^{-8}	1220	2000	0.0033	0.2430
WR 140	5.6×10^{-5}	1.6×10^{-6}	2895	3200	0.0314	2.6866

Table 2.4: Wind properties of systems simulated in this thesis.

System	Period (d)	Eccentricity (e)	M_{WR} (M_{\odot})	M_{OB} (M_{\odot})	Periastron (AU)	Apastron (AU)
WR 98a	556	~ 0	10.0	18.0	4.06	4.06
WR 104	245	0.0600	10.0	20.0	2.20	2.48
WR 140	2869	0.8993	10.31	29.27	1.53	26.9

Table 2.5: Orbital properties of systems simulated in this thesis.

WR98a

Because of this relative ease of simulation and relatively slow wind velocity for both stars in the system, WR98a was chosen to be the baseline system for the research conducted in chapter 4.

WR140

WR104

2.4.5 WR+WR systems

2.4.6 Contemporary research in extragalactic low-metallicity WCd systems

2. BACKGROUND

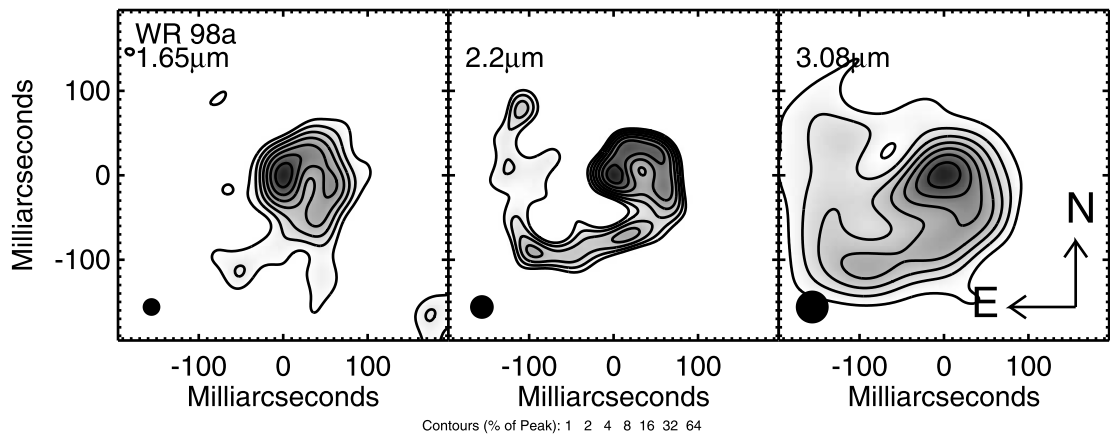


Figure 2.8: Multiwavelength aperture synthesis images of WR98a taken on June 24th 2000, at 1.65, 2.2, and 3.08 μm . Plot sourced from Monnier et al. (2007), the significant IR excess is a clear sign of ongoing dust production. The system also has a pronounced pinwheel structure most prominent at 2.2 μm .

CHAPTER 3

Methodology & Numerical Simulation

3. METHODOLOGY & NUMERICAL SIMULATION

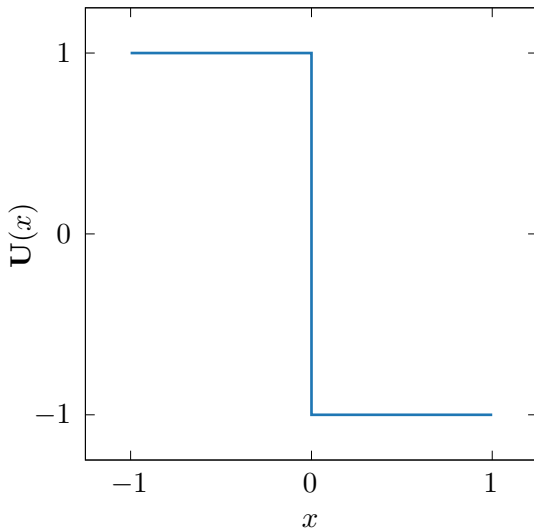


Figure 3.1: The initial conditions of a Riemann problem, where \mathbf{U} is a conserved variable.

3.1 The History & Mathematics of Numerical Simulations

The Euler equations are a specific case of the more general Navier-Stokes equations of fluid dynamics, covering the case of an inviscid fluid lacking thermal conductivity, these properties make the equations ideal for application to astrophysical fluids. At vast length scales the aggregate properties of a collection of molecules in near vacuum are essentially in-line with what is predicted by inviscid fluid dynamical equations; while the general lack of physical contact, both rare and fleeting, rules out the influence of thermal conduction and convection on the fluid at large. Astrophysical fluids at first appear strange and unintuitive compared to the more familiar fluid dynamics we have an almost innate understanding of as human beings; but if one zooms out enough and starts thinking in terms of parsecs and astronomical units, similarities begin to appear.

In a one-dimensional adiabatic case, with a fluid of density ρ , a velocity of u , a fluid pressure of P and a total energy, E , the Euler equations take the form:

3.1 The History & Mathematics of Numerical Simulations

$$\frac{\partial \rho}{\partial t} + \frac{\partial}{\partial x}(\rho u) = 0, \quad (3.1a)$$

$$\frac{\partial \rho u}{\partial t} + \frac{\partial}{\partial x}(\rho u^2 + P) = 0, \quad (3.1b)$$

$$\frac{\partial E}{\partial t} + \frac{\partial}{\partial x}[u(E + P)] = 0. \quad (3.1c)$$

As the Euler equations are a non-linear series of partial differential equations, no general analytical solution exists, to make it worse, numerical solutions aren't exactly easy either. The basest method of numerically solving such problems is Godunov's scheme (Godunov, 1959); this scheme is a finite-volume method wherein the problem is split into a series of cells, with a Riemann problem between the interfaces of each cell, an approximate solution to the Euler equations can then be made by solving all of these Riemann problems in sequence. This provides a first-order accurate approximation in a more general form, compared to the otherwise intractable set of PDEs. Whilst this piecewise method of solving many thousands of Riemann problems may provide a more generalised method of calculating fluid dynamics, performing it by hand would invoke a terrible strain on a mathematicians wrists. Godunov's scheme however, coincided with the burgeoning field of computer science,

Solving a higher-dimensional problem is a trivial extension to the original problem. In the 2-D case the number of interfaces increases to 4, with each interface being the analogous to each side of a square or rectangle, while in the 3-D case the interfaces can be thought of as the 6 faces of a cuboid. As such, the general formulation of the Euler equations becomes:

$$\frac{\partial \mathbf{U}}{\partial t} + \nabla \cdot [\mathbf{F}(\mathbf{U})] = 0, \quad (3.2)$$

where \mathbf{U} is a vector of conserved variables and $\mathbf{F}(\mathbf{U})$ is a vector of the corresponding fluxes of the conserved variables:

$$\mathbf{U} = \begin{bmatrix} \rho \\ \rho u \\ E \end{bmatrix}, \quad \mathbf{F}(\mathbf{U}) = \begin{bmatrix} \rho u \\ \rho u^2 + P \\ u(E + P) \end{bmatrix}. \quad (3.3)$$

In practise however, solving higher-dimensional problems are significantly more computationally intensive, due to the increased number of interfaces and the drastically increased number of cells required to simulate the problem.

3. METHODOLOGY & NUMERICAL SIMULATION

Approximate methods were developed to account for the exact methods computational complexity, however early methods were less exact, and could not preserve the contact surface, these methods were also markedly less stable, limiting their effectiveness. The Harten-Lax-van Leer-Contact (HLLC) solver (Toro et al., 1994) is a commonly used approximate Riemann solver that has a similar order of accuracy and robustness to an exact solver while being markedly more efficient to solve.

Godunov's method is commonly used as a base for higher-order extensions, which employ methods to reconstruct the

Piecewise linear (van Leer, 1979)

The piecewise parabolic method solves (Colella & Woodward, 1984)

3.2 The Purpose of Numerical Simulations

Numerical simulation, thanks to its generalised but calculation-intensive approximation of partial differential equations, has an enormous range of uses, especially in the field of astrophysics. In particular, numerical simulation excels in modelling over large timescales and regions that are difficult or impossible to observe. The laws of physics have remained fairly consistent over the last 13.8 billion years¹, because of this we have managed to simulate the conditions of the early universe, showing the collapse of over-dense regions of the burgeoning universe into filaments and eventually galaxies provides our only continuous look into the long-term evolution of the universe, with deep-sky observations able to catch snapshots of these effects. Regions that undergo too much extinction or that are too distant to observe can be simulated, as a reasonable estimation of the initial system parameters can be made. Numerical simulation, in a sense, fills in the gaps and weaves together the many snapshots of the universe we can make from our lone vantage point in a more uneventful part of the cosmos.

This is of course not me screwing my simulationist hat firmly onto my head and claiming that theoretical methods of astrophysics are inherently superior. Whilst an immensely versatile and useful tool in an astrophysicists arsenal, numerical simulations are entirely reliant on the understanding of the laws of physics as we know them, as well as the skill of the programmer. If a simulationist gets too far into the weeds, wielding numerical simulations like a hammer, every astrophysical problem begins to look like a nail, which creates its own problems.

¹With some earlier exceptions.

3.2 The Purpose of Numerical Simulations

Colliding Wind Binaries in particular are a class of astrophysical phenomena that truly rely on numerical modelling in order to glean further understanding from them. The WCR is particularly difficult to observe, there is no nearby prototypical WCd system, meaning observation of fine-detail features requires extremely high angular resolution telescopes to begin with, this is compounded by the relatively small size of the region of the WCR where dust is rapidly produced. Whilst observing the large-scale structure of the WCR is possible with current telescopes, and clear observation of the surrounding dust cloud is possible (such as in the case of the recently discovered Callingham et al. (2019)), observing the dust producing region is markedly more difficult. In the typical case of a dust producing region 50 AU across embedded in a WCd system at a distance of 3000 kpc an angular resolution greater than 30 μ as would be required to resolve the region, ruling out even the highest resolution instrumentation. As such, numerical simulation with a dust evolution model must be used to simulate the dust producing region, whilst the overall dust production rate from the simulation can be compared with observational estimates. This can be improved further, by the use of a radiative transfer model to model the dust production rate of the systems, however this was not feasible in the constraints of this projects timescale, but could be performed as a follow-up project.

It is a shame that CWB systems are difficult to *simulate* as well!

Numerical simulations can be vastly simplified by reducing the number of dimensions in the simulation, single object systems can be typically reduced to a 1-D spherically symmetric or 2-D cylindrically axisymmetric simulation, in the case of supernovae or jets, for instance. In the case of a CWB system with orbits however no dimensions can be reduced, a single dimension simulation will not simulate the WCR, while a 2-D axisymmetric simulation will not properly simulate the effect of orbital motion, which as we observe, is essential to determine the morphology of a WCd system. In addition to this, in order to see how dust evolves over the large length-scales of the WCR requires very large simulation domains, while accurately resolving the apex of the WCR requires a fairly high number of cells between the stars in the system (this was found to be approximately 100 cells for a typical system). The combination of these two factors is quite terrible, as the simulation is both 3-D and requires an extremely large effective resolution, enough to tax even the most capable of our available compute resources. Fortunately, mesh refinement techniques can improve this situation by drastically reducing the number of cells that need processing, simplifying our problem from “*impossibly intensive*” to “*extremely intensive*”.

3. METHODOLOGY & NUMERICAL SIMULATION

3.3 Computational Hydrodynamics

3.3.1 Comparison of hydrodynamical methods

3.3.2 The MG hydrodynamical code

The MG hydrodynamical code was utilised at the start of the project, as problem generators for CWB systems had already been written, while also being fairly well understood throughout the department. MG is a relatively easy to use hydrodynamics code many of the required features for this project, it is fairly extensible and supports MPI and AMR for fast and effective numerical simulation, it was initially estimated that this would take a little more than a year to implement the dust model, cooling models, and be on our way to running large-scale simulations – how wrong we were.

Unfortunately, the crux of the project – the advected scalar dust model – never adequately worked, either producing dust rates measurable in grams per year, or the simulation rapidly converting remapped wind into dust, despite it being too hot to do so according to our dust model. Attempts to implement the dust model through modification of the conserved variables or through a rate-based source function were made, with many different implementation attempts, none of these panned out, unfortunately, resulting in a large amount of work being discarded. Using strict constraints to prevent rigorous dust production resulted in strange looking systems, that did not behave as observations suggested. Furthermore, building a model that relies on dozens of constraints based on limited empirical data is rarely a good model, and is a bit like building a clock that doesn't move at all, so that it is at the very least right twice a day.

In addition to incompatibility with the dust model, numerous technical issues compounded this work. Mapping the wind onto the CWB also proved difficult when combined with AMR, as the provided implementation of wind remapping required a circular region with a radius of 3 coarse cells. In order to get the required separation for systems with close orbits, a very high coarse resolution would be required, massively increasing memory usage. using a source function for wind mapping allowed for more refined cells to be used, but this could also produce artefacts at level transitions, while also producing extremely hot winds as the temperature could not be correctly defined.

In general, while being very extensible in terms of being able to implement a problem generator fairly easily, low-level manipulation of the code was found to be extremely difficult due to

limited documentation and a complex, linked-list mesh structure. As such, writing workarounds and fixes to the issues described was very time-consuming, slowing progress in the project significantly. Compounding on this, iteration time was extremely long, requiring multiple hours to run a simulation to determine if the fixes worked, debugging was rendered difficult by the use of OpenMPI, and the general structure of the code rendered the setting of breakpoints difficult even in the single-threaded case. Finally, the numerical integrator was found to not be particularly stable in the face of extremely radiative cooling environments, complex multi-step cooling processes were considered and implemented, but even these could not handle such rapid cooling without breakdown if a reasonable Courant number was to be used. The solution was to artificially limit cooling to a fraction of the energy in the cell per timestep, however this reduces the simulation accuracy, and results in much slower cooling within the post-shock WCR¹.

In the end, the decision was made to switch from `MG` to the new `Athena++` hydrodynamical code. This decision was made in mid-2020, by the end of 2020 the problem generators were build, the necessary modification to the underlying code of `Athena++` were completed and the dust model was fully implemented.

3.4 The `Athena++` hydrodynamical code

The `Athena++` hydrodynamical code (<https://github.com/PrincetonUniversity/athena>) was found to be a much more suitable fit for this project. As documented in Stone et al. (2020), `Athena++` is a total re-write of the older `Athena` MHD code in C++ with a focus on implementing Adaptive Mesh Refinement, source code clarity, modularity, and generally improved performance. This clarity and modularity allows for a

As previously stated,

A problem

This problem generator is defined before compile-time, with a configuration script generating the required makefiles for `Athena++` for the specific problem, this ensures that only the required problem files are included in compilation, preventing any accidental overloading of function

¹I understand, reader, that this section reads like a series of complaints... This is because it is. I recommend that you humour me, as attempting to debug `MG` ate up more than two years of my life and was the direct cause of many, *many* sleepless nights. Thankfully this is the last time we will ever speak of it, unless you and I share a pint or two at a local pub.

3. METHODOLOGY & NUMERICAL SIMULATION

names or compiler issues, essential in a complex project with many different problem generators, this also allows for switching between different versions of a problem without complication, requiring only a quick reconfiguration and recompilation to change problem.

Multiple time-integration and spatial reconstruction methods have been implemented into **Athena++**, which requires essentially zero modification on the user's end, a startling revelation coming from other numerical codes. Time-integration method vary from a computationally simple 2nd order van Leer (van Leer, 1979) method to strong stability preserving methods (Ruuth & Spiteri, 2005) to super time-stepping Runge-Kutta-Legendre (Meyer et al., 2014) methods; changing of the time-integration method can be implemented without recompilation, and can even be changed upon restart of an in-progress simulation, which was found to be useful for if a simulation was having trouble running at a certain point. **Athena++** must be recompiled for the specific spatial reconstruction method, as the number of overlapping "ghost" cells needs to be defined at compile-time. In this project, either the 3rd order accurate strong stability preserving Runge-Kutta method (`rk3`) or the 4th order accurate, five-stage, 3 register, SSPRK method was utilised (`ssprk5_4`), depending on the instability of the simulation. The `rk3` method was found to be more than twice as fast as the `ssprk5_4` method in the case of a CWB system, though could crash in the cases of rapid cooling and dust production, if a simulation crashed multiple times the simulation would be altered to use `ssprk5_4`. The Riemann solver can also be changed at compile-time, however this was left to the default solver, the Harten-Lax-van Leer-Contact (HLLC) solver (Toro et al., 1994).

Part of

This is in comparison to the linked-list method of distribution which is used in **MG**, which is not performant in distributed multiprocessing systems such as ARC, as this can result in lots of communication of relatively small packets between nodes as a time-step is being calculated, reducing performance significantly due to bandwidth and latency constraints. This meshblock system does have drawbacks, however, time-stepping is synchronous, and bound to the width of the lowest level, this is not the case in **MG**, where multiple sub-steps are performed on lower levels, which are processed first, with the coarsest levels running on a single step. This method is much faster but can result in significant divergence from a synchronous method.

this can be slower in some cases, however in the case of a simulation such as this, with hypersonic winds and rapid cooling, a small time-step would typically need to occur anyway.

This is covered in more detail in the next section (section 3.5).

`Athena++` is highly parallel and utilises the OpenMP and OpenMPI software libraries in order

¹ Meshblocks are distributed to processor cores. In the case of a simulation that requires more cores than a single computer can provide, OpenMPI is used to distribute meshblocks between nodes in a HPC² cluster, whilst this can introduce bottlenecks due to the comparatively slow networking between nodes, this allows for thousands of cores to be used, rather than dozens.

In order to prevent numerical errors from occurring between the interfaces between meshblocks, “ghost cells”, cells from adjacent meshblocks copied into the current meshblock, are used.

3.5 Mesh Refinement

One of the problems previously discussed with modelling CWB systems is the wide range of length scales needed to appropriately simulate a system, the total dust production region can cover dozens of AU, while the WCR in order to be properly resolved needs to have a feature size between 3 and 4 orders of magnitude smaller than that. Coupled with the requirement for a 3-D model if orbits are to be considered and suddenly you find yourself looking at a simulation with a resolution with 10^9 cells or higher. In order to remain compliant with the Courant-Friedrichs-Lowy condition, the associated timestep must also be reduced, increasing the amount of computations in accordance with a fourth dimension. In the case of the more ambitious simulations in this project, a region approximately 1000 AU was defined, with an effective resolution of approximately 1.07×10^{12} cells; this sheer amount of data would be difficult to store, let alone compute, and would be far beyond the capabilities of any HPC service available to this project.

In order to resolve this resolution issue, using cells more effectively than brute-force increasing the resolution must be performed, as such, algorithms such as Adaptive Mesh Refinement (AMR) were introduced to the field of numerics with almost immediate uptake. AMR is a flexible method of mesh refinement, first discussed by Berger and Oliger (1984) and expanded upon by Berger and Colella (1989). This method starts with a “coarse” grid at the lowest defined resolution, and tests each cell against a series of conditions, such as proximity to an object in the simulation, conserved parameter or truncation error; if the cell passes any of these threshold conditions it is

¹Sadly, the engineers at Intel who worked on the Netburst architecture were [wrong](#), processors can't easily scale up to dozens of GHz, instead, multiple cores have to be used, making high performance code that much harder to write.

²High Performance Compute

3. METHODOLOGY & NUMERICAL SIMULATION

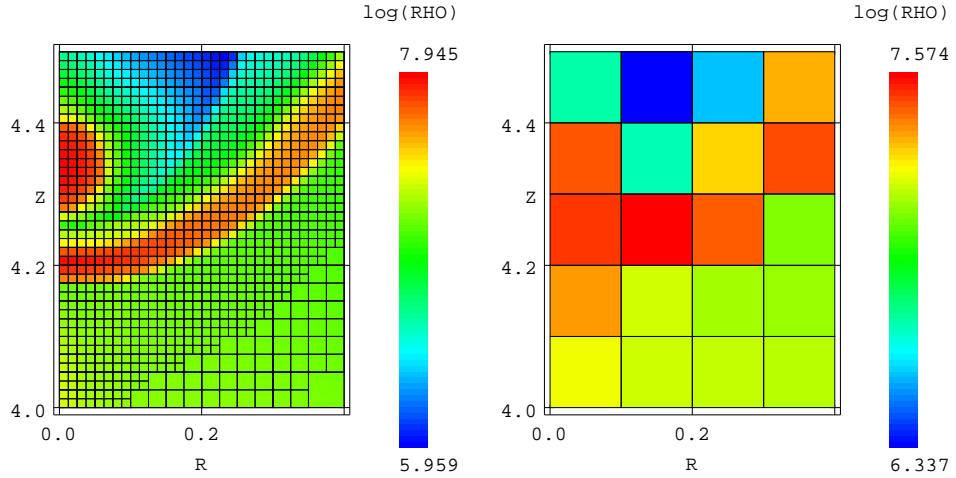


Figure 3.2: An example of adaptive mesh refinement in the MG hydrodynamical code around the OB star in a colliding wind binary problem using cylindrically symmetric coordinates. With AMR the WCR is properly resolved, while without the system cannot adequately resolve the WCR.

flagged for refinement. At the end of a simulation step, the AMR algorithm will split the cell in half along each axis, increasing the effective resolution of the cell. Conversely, a region can be flagged for de-refinement, where the cells are merged together again, if a condition was transient and is no longer being passed. Figure 3.2 shows this effect, the application of mesh refinement greatly increasing the resolution of the WCR, allowing for the space between the star and the WCR to be properly resolved, which is crucial for the physically accurate simulation of the CWB.

The benefit of this refinement on systems with only small regions requiring high resolutions is immediately apparent. In the case of the previously described system with 1.07×10^{12} cells, naively refining a region around 1.5 times the orbital separation from the barycentre with 7 refinement levels reduced the number of cells in the simulation to 1.55×10^6 cells, a 6 order of magnitude reduction in cell count and memory usage. Care must be taken, however, not to over-refine the simulation or to rapidly refine and de-refine a region. The former can be mitigated by defining a maximum refinement level, while the latter can be mitigated by defining a minimum number of timesteps required for a cell to be repeatedly flagged for refinement and de-refinement. Another issue with this method is multiple refinements per timestep for a cell, which can render the simulation unstable.

In the case of `Athena++` meshblocks are instead refined or de-refined, whilst this improves multi-threaded performance with multiple CPUs as it reduces the amount of communication required between processor nodes, this method does increase memory requirements, and is not optimal in an idealised case. Though, as these simulations are being performed on an HPC cluster this is optimal for our case. Unfortunately, despite the advantages of AMR over SMR, there is a known issue with `Athena++`¹ which prevents the use of AMR with passive scalars enabled, scalar values are not conserved properly around meshblock interfaces, which can rapidly escalate and result in physical inaccuracy and breakdown of the simulation. As there was ultimately no time to correct this bug, the decision was made to persist with using Static Mesh Refinement (SMR) for the second papers work, despite a version of the code already being written with AMR in mind.

Static Mesh Refinement operates by refining regions defined in the problem config file or code that can be refined to a higher resolution, which will progressively de-refine beyond this region until the coarse level is reached. Whilst markedly less flexible, this is still particularly useful for simulations where the resolution requirements remain approximately in the same place spatially. In the case of CWB systems this is a reasonably good approximation, as the region around the orbit of the stars can be refined to a higher resolution, while progressively de-refining further out from the barycentre. Due to the comparatively low flexibility of AMR in a block-based hydrodynamical code such as `Athena++`, this was a preferable alternative to refactoring our model to work in either `MG` or a different numerical code such as `Enzo`.

3.6 Visualisation

Data was plotted using a series of custom programmes designed to parse data as quickly as possible, the Python plotting library provided in the `Athena++` repository was modified to incorporate Delaunay triangulation, instead of interpolating data due to mesh refinement, data-points are triangulated with each other. For 3D visualisation the VisIt data visualisation tool is used.

¹<https://github.com/PrincetonUniversity/athena/issues/365>

3. METHODOLOGY & NUMERICAL SIMULATION

3.7 Simulating CWB systems

3.7.1 Assumptions

3.7.2 Wind propagation & refinement

3.7.3 Cooling in numerical simulations

As discussed in section 2.4.2, there are many cooling processes that need to be considered when simulating a complex system such as a CWB.

Sufficient cooling is in fact, essential to this dust formation process. Gas temperature in the immediate post-shock region can exceed 10^8 K, far beyond the temperatures required to adequately form dust, as any nascent grains would quickly be shattered by thermal processes. There is sufficient evidence to suggest that significant, rapid temperature loss occurs in the post-shock regime, the high metallicity of the WC wind and high number density of atoms and ions makes it the ideal region for rapid cooling due to radiative processes.

Another boundary to dust formation due to an insufficiently radiative post-shock flow is a lack of sufficient downstream density. In the case of strong, adiabatic shocks, constraints are set on the downstream gas parameters of the system, such that:

$$u_b = \frac{1}{4}u_a, \quad (3.4a)$$

$$\rho_b = 4\rho_a, \quad (3.4b)$$

$$P_b = \frac{3}{4}\rho_a u_a^2, \quad (3.4c)$$

where a is the upstream side and b is the downstream, post-shock side. As the gas density can only be a factor of 4 larger than the post-shock flow, the post shock density (even if it were at temperatures suitable for dust formation) is insufficiently dense for sufficient dust production. However, in a radiative shock behaving isothermally (where the temperature change, ΔT throughout the entire lifespan of the fluid is equal to zero), the final density, ρ_f can be approximated to:

$$\rho_f \approx \gamma M_a^2 \rho_a, \quad (3.5)$$

where M_a is the pre-shock mach number. For a shock with an initial sound speed of $M_a = 100$ the final density can exceed the pre-shock density by a factor of 10^4 !

Performing radiative cooling within a numerical simulation is computationally difficult, and trade-offs between accuracy and performance must be considered at every step of designing the simulation, as every single cell must undergo cooling. For this project, the final cooling can be out by a few percent at worst, but is fast enough to run the simulations in a reasonable amount of time without excessive memory requirements. In order to simplify the radiation calculations, radiation does not re-interact with the simulation, instead it is completely removed from the simulation. Due to this, scattering, re-adsorption and radiative transfer are not simulated at all.¹. Other methods of reducing computational cost and optimising the code are used in this project, and will be described in detail in this section.

Plasma cooling

Thus, instead of calculating the emissivity of the plasma for the current density, temperature and abundances, a lookup table is pre-calculated and loaded into the simulation at runtime. These lookup tables are generated by combining a series of lookup tables generated for pure flows of elements, and combined based on the abundance of the element within the stellar wind, hence each star in the simulation has its own unique lookup table. A typical lookup table in this project utilises logarithmically spaced temperature bins from 10^4 K to 10^9 K, with 100 bins in total, if the calculated temperature is between bins a linear interpolation step is used to improve the accuracy of the the emissivity solution. In order to calculate the energy loss within a cell, the following formulae is used:

$$\frac{dE}{dt} = \left(\frac{\rho}{m_H} \right) \Lambda_w(T), \quad (3.6)$$

where $\Lambda_w(T)$ is the normalised emissivity at the cell temperature, T. This solution is orders of magnitude faster than performing an emissivity calculation in every cell, and is essential to performing fast hydrodynamical simulations with plasma radiative cooling.

Other optimisations relied on replacing a naïve linear search with an indexing method that relied on the logarithmic spacing of the temperature bins, instead of performing a search the

¹If these are considered, your programme is now a ray-tracing programme as well as a hydrodynamical code, which is its own, even more complicated field.

3. METHODOLOGY & NUMERICAL SIMULATION

index, n , of the emissivity value stored in an array can be calculated using the formulae

$$n = \left\lfloor \frac{\log(T) - \log(T)_{\min}}{\delta \log(T)} \right\rfloor, \quad (3.7)$$

where $\log(T)$ is the log of the cell temperature, $\log(T)_{\min}$ is the minimum log temperature in the lookup table and $\delta \log(T)$ is the log spacing of the temperature bins. This speed-up is fairly significant as the average search performance changes from $\mathcal{O}(n)$ to $\mathcal{O}(1)$ time, a marked improvement over even a binary search, which would resolve in an average of $\mathcal{O}(\log n)$ time. In the case of a 100 bin array this is only a minor speed-up, but with the sheer number of calculations being performed, any optimisation to a function used multiple times per cell can significantly improve performance. In the case of larger, or multi-parameter lookup tables this method would only improve in performance, and is a good example of general optimisation in a numerics programme.

In order to integrate the energy loss rate to determine the exact amount of energy lost within a timestep, an integration method needs to be chosen, for this project, a fast, first-order Euler method with multiple sub-steps was chosen. Whilst this method is not particularly accurate or robust, it was found to be fast, and the adaptive sub-step method was found to calculate a reasonably accurate approximation of a cells change in temperature in a very small amount of time. This sub-step method is elaborated on in section 3.7.4.

Other methods of refining the emissivity value were also considered, such as fitting a local curve to the data or using a spline-based interpolation step instead of a linear step, however these were only marginally more accurate, at a significantly increased calculation time. An exact cooling method was also considered, which was found to be significantly more performant, but had a series of limitations that prevented it from being used in the codebase at this time. This exact cooling method, described by Townsend (2009), introduces a temporal evolution function (TEF), $Y(T)$, into the solution, which describes a measure of the total time required to cool from an arbitrary temperature to T . This function, as well as its inverse, need to be calculated prior to cooling being calculated, but do not have to be calculated for every cell and timestep, while solving the TEF for the cell temperature takes approximately the same amount of time as a single first order Euler method integration, whilst offering an *exact* calculation of the post-step temperature. This scheme is one of the rare example of a numerical method that is both accurate *and* fast, taking approximately the same time as a second order explicit method overall, whilst also being perfectly accurate even in highly radiative hypersonic flows. Unfortunately this

method has a number of limitations that precluded its usage in this project. First, this method would not have been able to accurately model mixed wind situations, hampering its usage cooling winds with drastically different abundances. Second, and most importantly, dust cooling could not have been modelled with this single parameter TEF method, which would have required using a two stage cooling method, as the gas temperature would not be synchronised between stages, this would have resulted in a highly inaccurate cooling solution, obviating the advantages of the exact cooling method.

Dust cooling

Dust cooling

In the case of the immediate post-shock environment where dust is present in the form of small, rarefied nascent grains, the cooling rate is greater than the plasma cooling rate due to bremsstrahlung, as seen in figure 3.3. As such, it is assumed that dust cooling plays an initial role in the initial cooling of the post-shock flow in colliding wind binaries, and should ideally be included.

Whilst a lookup table has proven to be adequate for plasma cooling, dust cooling for a given stellar wind is markedly more difficult to solve. Whilst emissivity due to radiative processes in a gas or plasma can be parametrised in terms of temperature assuming that the flow abundances remain the same, the same does not apply to dust cooling, which requires three parameters, the grain radius, density and temperature. Calculating emissivity due to dust is a markedly simpler proposition than calculating plasma emissivity, and could be performed quickly within a hydrodynamical code if only grain-atom interactions are considered. Grain-electron interactions are a markedly more complex proposition.

The complexity in grain-electron interactions lies in determining the electron transparency, h_e , which is the probability that an electron will embed in the dust grain and heat it, rather than pass through. h_e can be computed via integration by parts, however due to this occurring in the main cooling loop, this results in a nesting of integrals, which can lead to extremely time-consuming computation for individual cells. The integral could be simplified by reducing the number of bins to integrate with, however below approximately 400 bins the results can become extremely inaccurate, resulting in incorrect or even *negative* values for h_e . More complex integration methods reduce the number of steps required, but are in themselves more time consuming to calculate, leading to the same issue. Initial tests using the integral method within

3. METHODOLOGY & NUMERICAL SIMULATION

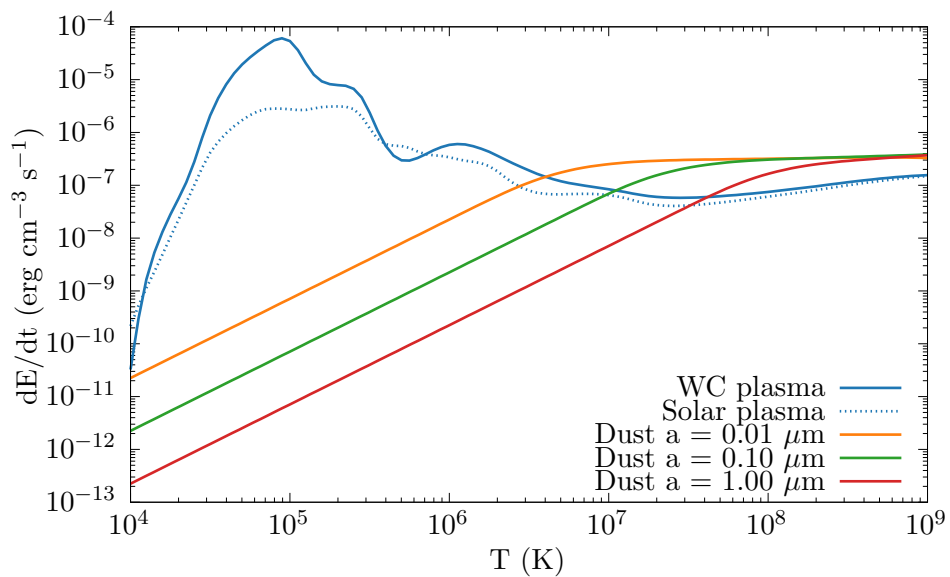


Figure 3.3: Comparison of energy loss due to plasma & dust cooling with varying grain sizes in a typical post-shock flow, where $\rho_g = 10^{-16} \text{ g cm}^{-3}$ and a dust-to-gas mass ratio of 10^{-4} . Whilst less influential at lower temperatures, dust cooling can aid cooling in the immediate post-shock environment.

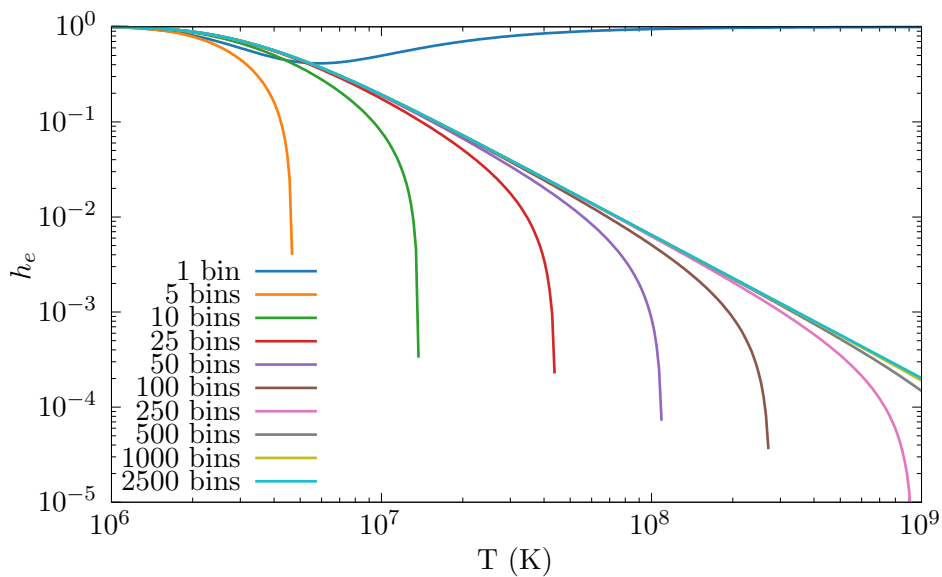


Figure 3.4: Comparison of h_e as a function of temperature for dust grains with a radius of $0.005 \mu\text{m}$, h_e is calculated via the trapezium rule with a varying number of bins, bin counts below 400 bins result in wildly inaccurate or in some case negative values for h_e , while beyond 400 bins the result is accurate and converges slowly.

3. METHODOLOGY & NUMERICAL SIMULATION

a numerical simulation led to severe slowdown as processing time for cooling took up to 90% of the overall processing time for each timestep. The effect on grain heating due to electron interactions cannot be discounted, as it can be up to an order magnitude greater than grain heating due to incident atoms. This was considered to be unacceptable in terms of performance, and as such a faster method needed to be determined.

Multiple options were considered for improving the performance of this routine. Initially, a Λ_d lookup table was considered, this consisted of a logarithmically spaced table of ρ , a , T and Λ_d values calculated by an implementation of the Dwek and Werner, 1981 prescription. A binary search for each parameter is performed, with the an offset, P_d , being calculated for each parameter,

$$P_d = \frac{P - P_0}{P_1 - P_0}, \quad (3.8)$$

these offsets are then used to perform a trilinear interpolation to calculate λ_d from the lookup table.

$$\begin{aligned} \Lambda_{00} &= \Lambda_{000} (1 - \rho_d) + \Lambda_{100}\rho_d, \\ \Lambda_{01} &= \Lambda_{001} (1 - \rho_d) + \Lambda_{101}\rho_d, \\ \Lambda_{10} &= \Lambda_{010} (1 - \rho_d) + \Lambda_{110}\rho_d, \\ \Lambda_{11} &= \Lambda_{011} (1 - \rho_d) + \Lambda_{111}\rho_d, \\ \Lambda_0 &= \Lambda_{00} (1 - a_d) + \Lambda_{10}a_d, \\ \Lambda_1 &= \Lambda_{01} (1 - a_d) + \Lambda_{11}a_d, \\ \Lambda &= \Lambda_0 (1 - T_d) + \Lambda_1 T, \end{aligned} \quad (3.9)$$

where 0 is the lookup table value lower than the parameters actual value, and 1 is the lookup table value greater than the parameters actual value. This implementation was written in the form of a series of nested loops to utilise SIMD vectorisation to improve performance.

Whilst this method is significantly faster than calculating Λ for each cell with an integration step, a $(100 \times 100 \times 100)$ lookup table requires approximately 32 MB of memory to store, and is much more time consuming to search through. As such, eliminating complexity from the binary search and reducing the number of interpolations were identified as improvements to the These optimisations were made by simplifying the lookup table into a series of smaller lookup tables

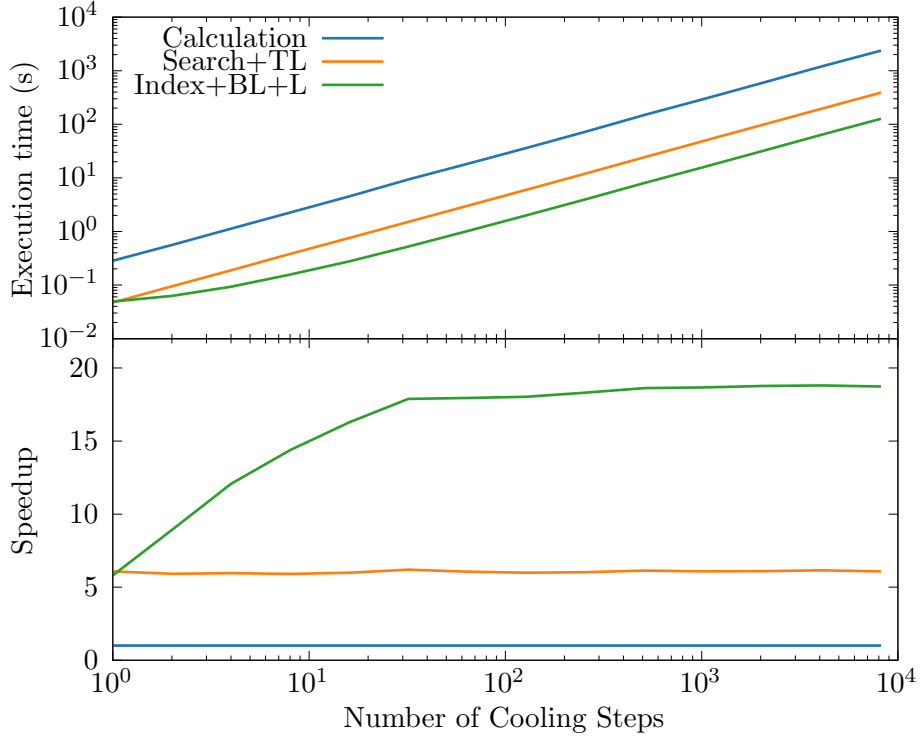


Figure 3.5: Comparison of execution time and speedup for lookup table methods.

and relying on even logarithmic spacing of the lookup table to determine the parameter indices, rather than performing a binary search for them. Additionally, as ρ and a are invariant within the cooling loop, these parameter offsets are solved separately using a bilinear interpolation, while in the cooling sub-step loop, a separate linear offset is performed to find the temperature offset, solving to find Λ_d . These optimisations resulted in this method scaling significantly better, as there is a lower total number of calculations required as the number of sub-steps increases (figure 3.5).

The second method considered for solving the h_e integral was using an approximation described by Dwek and Werner, 1981 where h_e could be described by a series of equations:

$$\begin{aligned}
 h_e(x^*) &= 1, & x^* > 4.5, \\
 &= 0.37x^{*0.62}, & x^* > 1.5, \\
 &= 0.27x^{*1.50}, & \text{otherwise,}
 \end{aligned} \tag{3.10}$$

3. METHODOLOGY & NUMERICAL SIMULATION

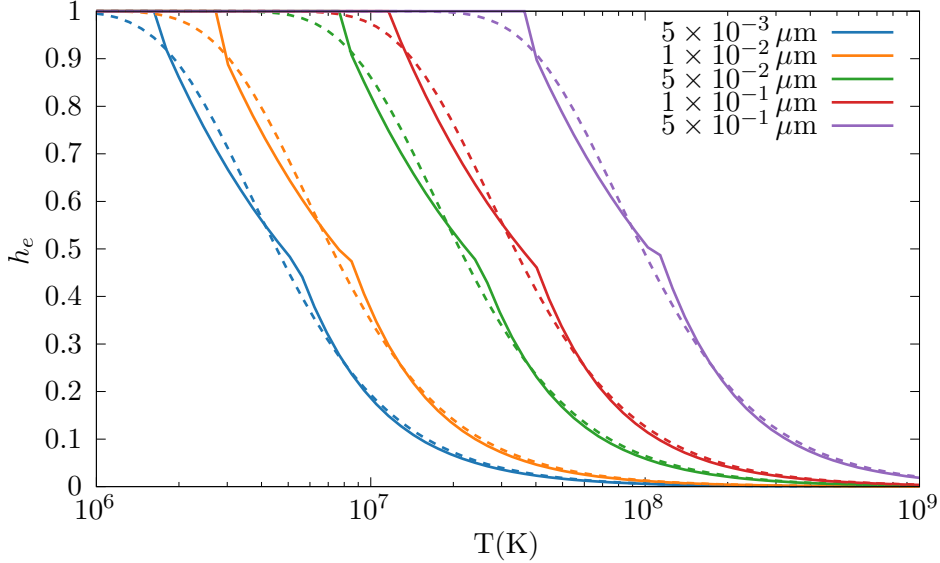


Figure 3.6: Grain transparency as a function of temperature for the estimate method described in equation 3.10 (solid lines) and a 400 bin integration method (dashed lines).

where $x^* = 2.71 \times 10^8 a^{2/3}(\mu\text{m})/T$. Whilst this is less accurate, especially in the region where one case ends and the other begins where the result begins to diverge, this method is multiple orders of magnitude faster. Figure 3.6 shows these discrepancies, in the case where electron transparency begins to decrease the approximation is out somewhat significantly, as well as mid-way through the curve, whilst at temperatures below 10^6 K the approximation and integral methods are perfectly aligned. As the grains grow hotter and the electron transparency reduces, the influence on the cooling rate due to incident electrons reduces quite drastically, meaning that extremely high accuracy is less important at these temperatures (figure 3.7). The accuracy of the approximation method is also shown in figure 3.8, the estimated value for Λ_d closely matches the integrated value aside from the smallest dust grains at very high temperatures $T > 6 \times 10^8$ K.

Table 3.1 shows the improvements to performance inherent in the estimation method; the final result is that the approximation is over 24,500% faster, the resulting dust cooling function therefore will have a minimal computational impact on the cooling loop as a whole. As this approximation was conclusively shown to not significantly effect the cooling rate due to grain heating, the approximation was chosen.

Further improvements were made to correctly determine the electron number, n_e , to calculate the cooling contribution for dust due to grain-electron collisions. the initial version of this code

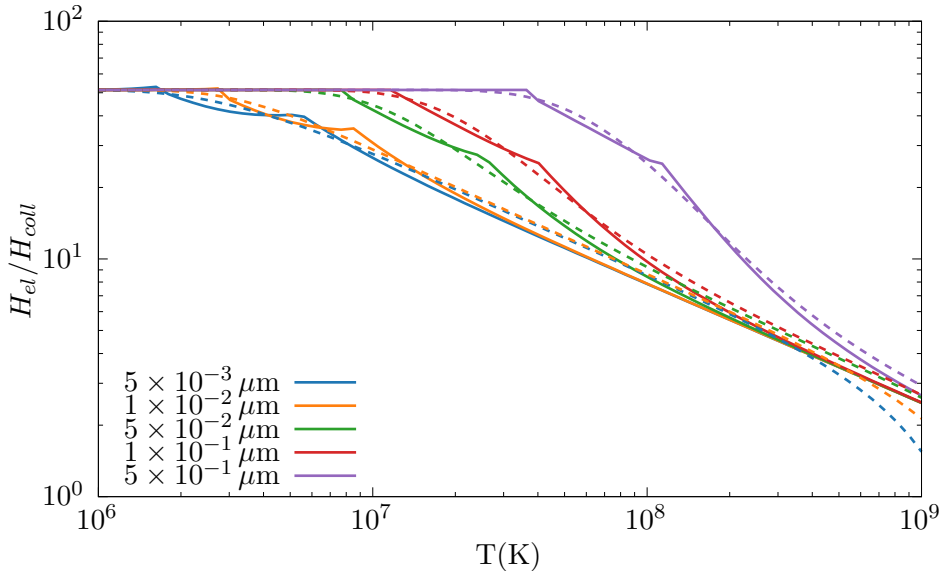


Figure 3.7: Comparison of the ratio heating rate of a dust grain due to incident electrons and incident atoms as a function of temperature for various grain sizes, whilst the result between the integration method and estimate method diverge, this is while the contribution of heating from electrons becomes less influential on the cooling rate of the grain.

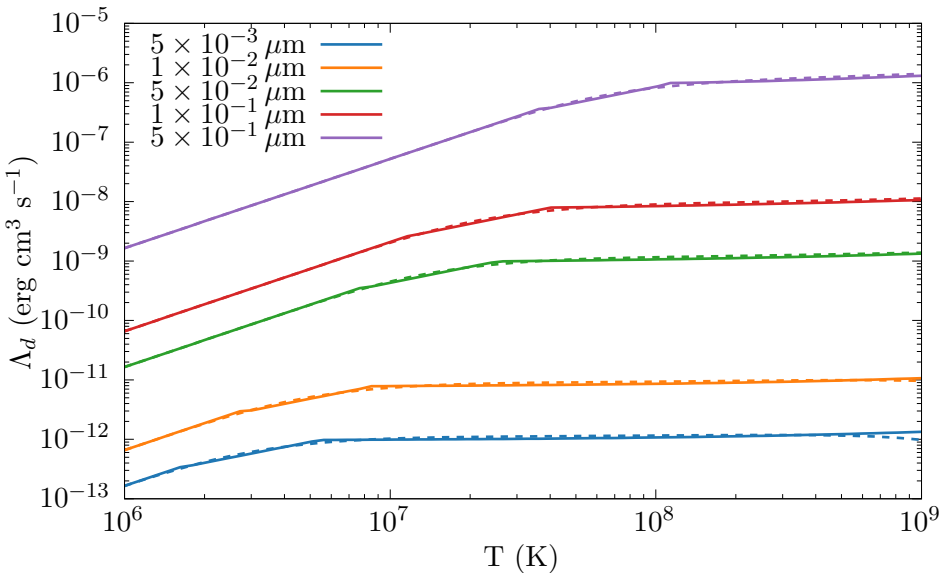


Figure 3.8: Λ_d as a function of temperature for various grain sizes, the estimate method is extremely close to the integral value aside from at the highest temperatures.

3. METHODOLOGY & NUMERICAL SIMULATION

Method	t(s)	Iter/s	Speedup
400 bin integration by parts	36.03	35,526	-
Binary search + trilinear	6.016	212,751	599%
Index calculation + bilinear + linear	1.999	640,447	1,803%
Dwek and Werner, 1981 approximation	0.147	8,693,171	24,510%

Table 3.1: Comparison of methods explored for estimating $\Lambda_d(\rho, a, T)$ in cooling code, 10^4 initial values were chosen and 128 cooling sub-steps were performed, benchmark code was compiled and run using GCC 10.3.0 with the `-O3` optimisation set on an Intel i7-7700HQ processor with a maximum clock speed of 3.8 GHz.

assumed that $n_e = 1.1n_p$, an estimate based on solar abundances, however the electron-to-ion ratio varies significantly with temperature in a WC wind, which is hydrogen depleted and as such can vary from 0 to ~ 4 between 1×10^4 and 5×10^6 K (figure 3.9). In order to solve this problem quickly for each timestep, a lookup table similar to the plasma cooling curves was used, containing the electron-ion ratio at temperatures between 10^4 and 10^8 K for each wind abundance.

3.7.4 Model implementation

In order to simulate energy loss due to radiation in **Athena++**, the conserved variable array is adjusted to remove energy from a specific cell, this is analogous to energy being removed from the system due to radiative processes. This process is assumed to be 100% efficient, re-adsorption and scattering is not simulated, as this would be very complex to simulate at every time step.

Radiative processes are part of a source function that is performed for every mesh block. The cooling routine within the source function iterates through all cells within the meshblock, calculating radiative energy loss for each cell. Within the loop, the cell parameters are loaded from the conserved variables array, and additional gas and dust parameters are calculated from these conserved variables. in particular the mean molecular mass of a cell is calculated with the formulae:

$$\mu = C\mu_{WR} + (1 - C)\mu_{OB}, \quad (3.11)$$

where μ_{WR} and μ_{OB} are the mean molecular masses of the winds and C is the wind “col-

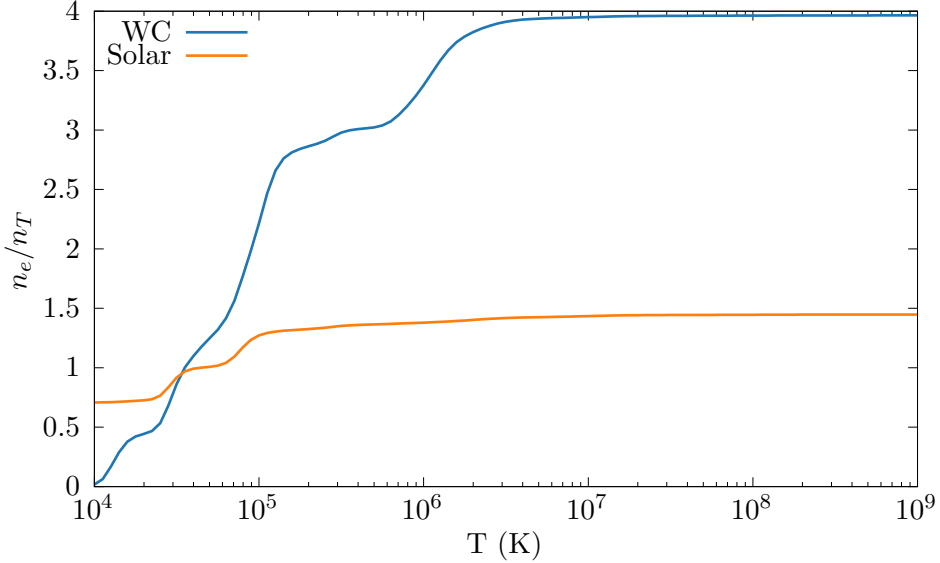


Figure 3.9: Ionisation fraction

our” scalar, the contribution of each wind to the gas density of the cell. The temperature is subsequently calculated using the ideal gas law:

$$T = \frac{P\mu m_H}{\rho k_B}. \quad (3.12)$$

At the current temperature, the cooling parameter, $\Lambda(T)$ for each wind is found from the lookup tables, and weighted in a similar manner as equation 3.11. The energy loss due to dust grains is then calculated, with the total energy loss rate within the cell defined as:

$$\dot{E} = \dot{E}_G + \dot{E}_D = \left(\frac{\rho}{m_H} \right)^2 \Lambda_G(T) + n_D \dot{E}_{\text{grain}}, \quad (3.13)$$

this energy loss rate is then multiplied by the timestep, dt , and then subtracted from the total energy within the cell.

One of the main issues with estimating the cooling rate rather than performing an exact calculation of energy loss is that the cooling rate and current temperature are coupled, this can result in wildly inaccurate final temperatures at the end of the cooling step compared with an exact integration. This is especially a concern at the expected temperatures in the post-shock, radiatively cooled environment, as the $\Lambda(T)$ is maximised at approximately 10^5 K. If

3. METHODOLOGY & NUMERICAL SIMULATION

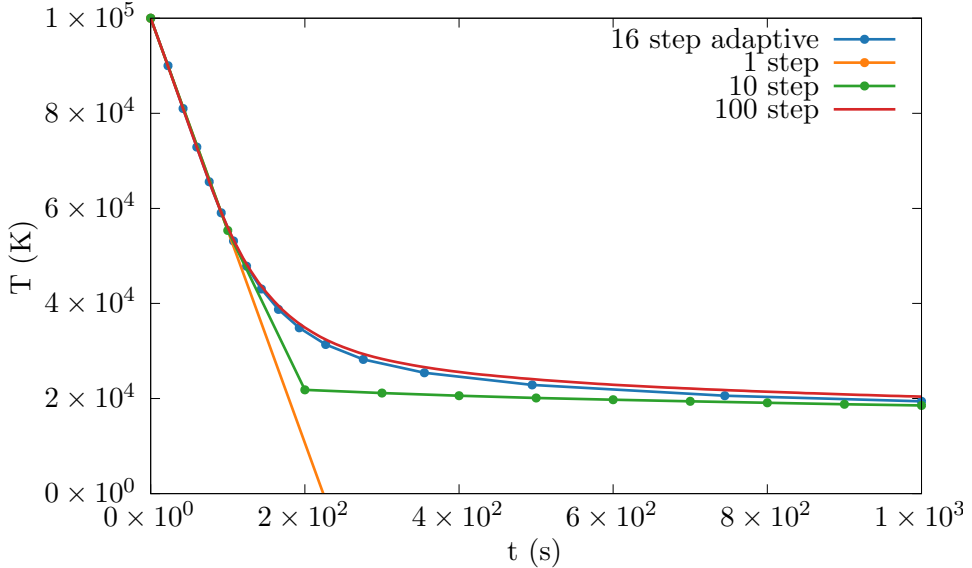


Figure 3.10: Comparison of the adaptive timestep method versus linearly spaced sub-steps for a solar abundance flow with a density of $10^{-16} \text{ g cm}^{-3}$ and an initial temperature of 10^5 K .

the timestep is too large this can result in over-estimation of the cooling. The simplest solution would be to make the time-step smaller, however this would reduce the performance of the code, as the cooling loop takes significantly less time to perform than the hydrodynamical loop. Instead, adaptive sub-stepping is used to iterate through the time-step, adjusting the maximum sub-step for an integration based on the current gas parameters, specifically the amount of energy remaining in the cell. Figure 3.10 shows the adaptive sub-stepping routine in operation, at the initial time, the cooling parameter Λ is maximised, as such the time-step is significantly lower than when the gas has cooled as is less radiative. This compares favourably to a single sub-step example, which would cause the simulation to crash due to negative temperatures, and with linearly spaced steps, which either required many more steps or were potentially unstable.

A suitably accurate maximum cooling time is calculated by first calculating the cooling time in the cell using the formulae:

$$\tau_{\text{cool}} = \frac{E_i}{\dot{E}_{\text{iter}}}, \quad (3.14)$$

where E_i is the cells internal energy and \dot{E}_{iter} is the total energy loss rate for the current iteration.

A fraction of this value is used as the sub-timestep, which is used to calculate the energy loss in that iteration.

$$dt_{\text{step}} = \kappa \tau_{\text{cool}}, \quad (3.15)$$

Another iteration of the cooling calculation is then performed, with sub-step time re-calculated, until the elapsed time is equal to the hydrodynamical timestep, dt . Throughout the simulations in this project a value of $\kappa = 0.1$ was adopted.

In order to assess the performance and accuracy of this method, a test environment was produced to simulate the radiation of a region of gas in the post-shock environment. For this test, a gas density of $10^{-16} \text{ g cm}^{-3}$ and an integration timestep of 1000 s were utilised. In order to demonstrate the flexibility of the adaptive method over the temperature ranges of a CWB simulation, initial temperatures of 10^5 , 10^6 and 10^7 K were used to demonstrate the models effectiveness in the cool, warm¹ and hot regimes of the WCR. This was compared with the exact integration method proposed in Townsend, 2009 as well as a modified version of the cooling code which uses evenly spaced sub-steps. To demonstrate the relative accuracy of the chosen cooling timescale fraction, lower values of κ were also used to demonstrate that lower values, while more accurate, were much more computationally complex.

The main limitation of a first-order Euler integration method such as this is that it converges on the correct answer slowly, and as such will be out by a few percent in the worst case so long as a sensible sub-step is used. Table 3.3 shows that while an iteration of the logarithmic index method used in this project is slightly more performant than the fast exact integration method proposed in Townsend, 2009, multiple sub-steps quickly render this performance benefit moot, in high-temperature cases with a lower gas density this method is much more accurate with fewer steps, however, as such this method was considered suitable for performing radiative cooling in the high-temperature immediate post-shock environment and lower density low-temperature WCR environment, where the bulk of this project focusses.

Whilst this is a fairly simplistic method of performing adaptive sub-stepping, it is fast, effective, and not prone to failure. An adaptive RK method and implicit method were also considered, but not utilised in the final code, as this sub-stepping procedure was intended for speed and numerical safety over accuracy.

¹See what I mean about the phrase “warm”?

3. METHODOLOGY & NUMERICAL SIMULATION

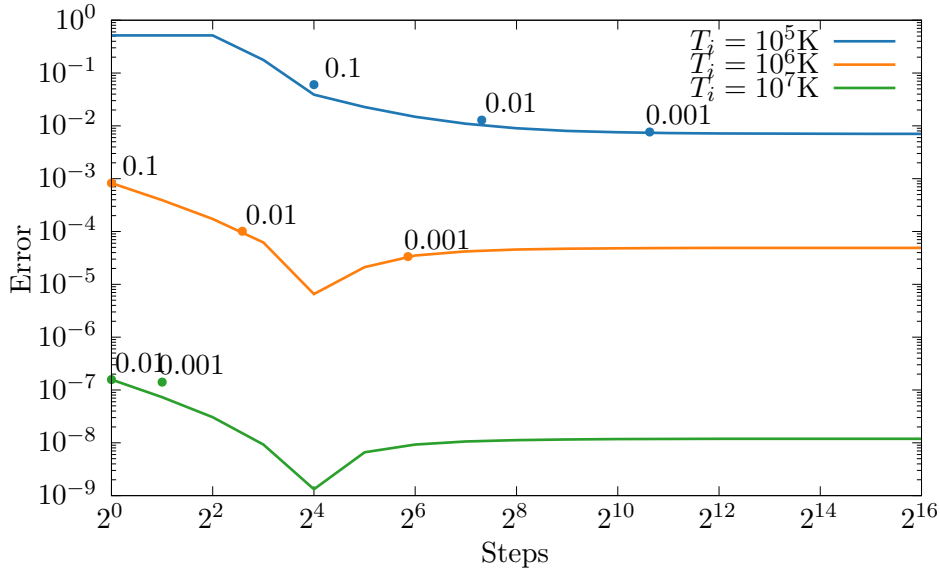


Figure 3.11: Comparison of estimated , points represent κ , in the low temperature case the answer is not particularly accurate, but with the adaptive method with $\kappa = 0.1$ the result is only out by a few percent for a small number of sub-steps.

Care is made to correctly calculate energy loss around unresolved interfaces. *Finish this!*

3.8 The BODMAS Advedted Scalar Dust Model

Binary Orbit Dust Model with Accretion and Sputtering¹

The primary focus of this project was to implement a dust model within a numerical simulation, in order to determine the growth of dust grains within the

3.8.1 BODMAS features

3.8.2 Implementation

The most processing efficient method of

This method does have its drawbacks, principally, the advected scalar method cannot simulate grain-grain or grain-gas interactions with high relative velocities, such as interactions within

¹All good theses have a laboured acronym!

3.8 The BODMAS Advected Scalar Dust Model

	$\kappa = 0.1$		$\kappa = 0.01$		$\kappa = 0.001$	
T_i	Steps	Error	Steps	Error	Steps	Error
1×10^5 K	16	6.025×10^{-2}	159	1.282×10^{-2}	1585	7.637×10^{-3}
1×10^6 K	1	8.233×10^{-4}	6	1.012×10^{-4}	58	3.359×10^{-5}
1×10^7 K	1	1.577×10^{-7}	1	1.577×10^{-7}	2	1.411×10^{-7}

Table 3.2: Accuracy of the adaptive sub-step Euler method compared with the Townsend, 2009 exact cooling method, with $\kappa = 0.1$ this method is out by 6% at worst in the low-temperature example, while very accurate at higher temperatures with only a single step needed.

	Search	Logarithmic	Townsend, 2009
τ (ns)	146	134	151
$\Delta\tau$ (ns)	8.0	1.5	0.9

Table 3.3: Comparison of performance between first order Euler integration methods and the exact integration method described by Townsend, 2009. Tests were conducted with a sample of 10^6 iterations on a 3.2 GHz M1 processor, while the code was compiled using clang 12.0.5 and the -O3 optimisation set.

the wind collision region, where

3.8.3 Contemporary dust Models

The Hendrix dust model

Perhaps the most similar contemporary dust model is the model described in Hendrix et al., 2016 - as this model is concerned with simulating the dynamics of dust within a CWB. This is not to say that these models are identical, of course, as the Hendrix model explores how dust spreads throughout the WCR of WR 98a, in order to compare with observational data using radiative transfer code.

The main differentiating factors between this model and our model are the driving mechanism and dust evolution. In the Hendrix model dust is modelled as a separate fluid, with an Epstein drag function between the wind and dust fluids; this method allows for dust kinematics that

3. METHODOLOGY & NUMERICAL SIMULATION

aren't implicitly co-moving. This is a more accurate method of modelling dust, however it requires significantly more processing time and is much more difficult to implement, requiring a numerical code that supports multiple fluids. At the start of this PhD this was considered but eventually rejected due to time constraints.

However, the Hendrix model has limitations that this model does not have, this is because the purpose of the Hendrix model is to analyse the distribution of dust within a CWB system, rather than to model the evolution of the dust itself. To this end, the Hendrix model does not calculate dust growth or destruction, and only uses a single small grain size, with the dust-to-gas mass ratio calculated based on observations of the target system, WR98a.

3.8.4 Future dust models

Due to time constraints and limitations in the code in use, only a limited set of mechanisms for dust evolution were included in this projects simulations. While the BODMAS model represents an interesting start for the modelling of dust grains in colliding wind binaries, future models could implement more complex models which incorporate additional destruction and growth mechanisms as well as

A multi-scalar model could be used to more accurately measure the growth of dust grains, rather than a single average grain size and This would be more difficult to implement than a single model but would be able to simulate the growth of grains with a large number *Athena++* and MG both have issues with a large number of scalars, as such both numerical codes may require significant modification to cope with this. A multi-fluid model with dust being physically simulated rather than assumed to be perfectly co-moving would be an ideal next step. Multiple grain size distributions could also be modelled in a similar way to the proposed multi-scalar model, however the kinematics of the dust grains could also be simulated separately. The increased inertia of more massive dust grains could result in the kinematics of the dust flow diverging from the co-moving assumption. To that end, a successor dust model would adopt a multi-fluid and drag function method, which was considered but not included for the sake of time. This multi-fluid model would also allow for more physically accurate simulation of grain-gas and grain-grain interactions, as the collision velocities would be exactly calculated rather than estimated through bulk motion properties, high speed collision of gas on dust grains in the immediate post-shock environment could also shatter grains, though modelling this as well as spalling of particles in the wind through the dust grains would be complex to simulate.

3.8 The BODMAS Advedted Scalar Dust Model

Furthermore, additional mechanisms for dust destruction, such as through photodissociation and sublimation could also be implemented, the implementation of these could be used to determine the effectiveness of the WCR in protecting nascent, still forming dust grains.

The initial grain nucleation model could also be improved, injection of extremely small grains into the simulation through the stellar remap zones was chosen as the underlying chemical process for formulation of these dust grains is poorly understood at the time of writing. The small grain nucleation model was also found to be only dependent on the initial grain radius, a_i , whilst changing the amount of grain nuclei in the WR wind does not change the amount of dust produced. As such the simulations are currently bound by a single input parameter, which can be constrained based on what is currently understood about dust grain accretion. A more complex model may require additional parameters, and as such would be highly dependent on them.

Another avenue of future research would be performing a radiative transfer simulation upon a fully advected system, in order to compare with This was initially considered at the start of the project, but was not performed due to the limited amount of time remaining at the end of the PhD. This was performed by Hendrix et al. (2016), with the resultant images emulating the sensitivity and angular resolution characteristics of UKIRT, Keck and ALMA (figure 3.12). Radiative transfer models would be used to

3. METHODOLOGY & NUMERICAL SIMULATION

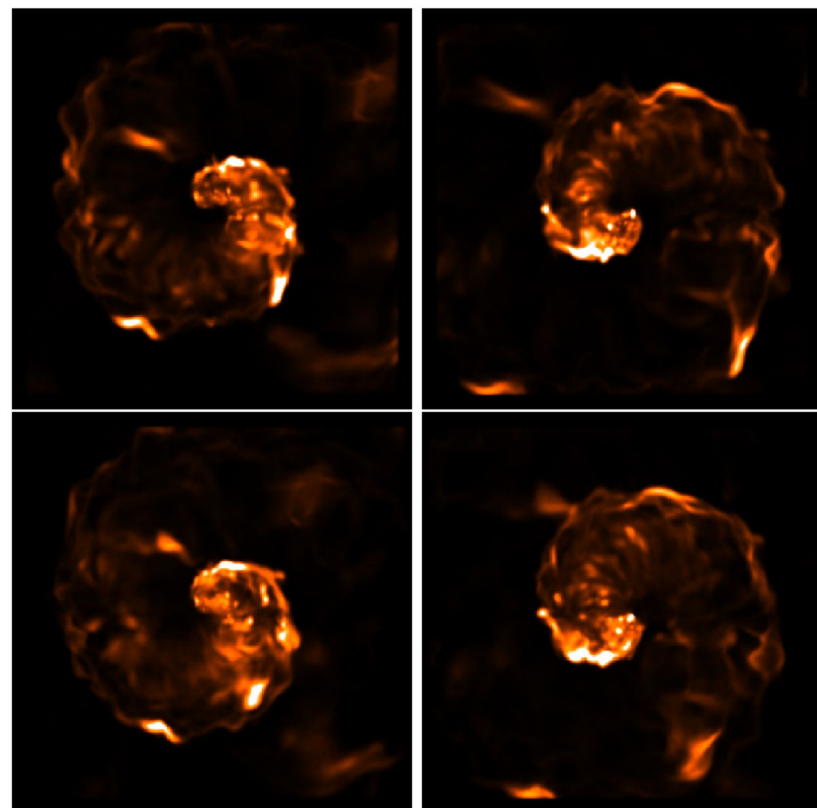


Figure 3.12: Synthetic images of WR 98a emulating the capabilities of ALMA using a radiative transfer model, reproduced from Hendrix et al. (2016).

CHAPTER 4

A Parameter Space Exploration of Dust Formation
within WCd Systems Using an Advectored Scalar Dust
Model

4. A PARAMETER SPACE EXPLORATION OF DUST FORMATION

Abstract

4.1 Introduction

Binary systems with colliding stellar winds are a fascinating phenomena capable of producing a variety of phenomena. The shocks produced from these interacting systems create some of the most luminous persistent stellar-mass X-ray sources in the night sky (Usov, 1991). Within the wind collision region the available mechanical energy rivals the radiative energy of many stars, producing shocks with temperatures up to 10^8 K.

Despite this, in particularly energetic Colliding Wind Binary (CWB) systems, dust has been observed to form. In particular, dust formation occurs around evolved Wolf-Rayet WC sub-type stars that are partnered with an OB type main sequence star, or a WR+OB binary. Allen et al. (1972) first attributed IR excess around WC systems to dust in the form of amorphous carbon grains; however, the high wind temperatures and extremely high luminosities around WC systems are such that dust grains would be readily destroyed through sublimation processes. Despite this, dust has been observed to form readily in binary systems (a WCd system), despite an additional highly luminous star and shocks that would quickly destroy dust acting upon these nascent, fragile dust grains. The exact mechanisms of dust formation as well as the evolution of dust within these systems is poorly understood. However dust formation rates can be extremely high, up to $10^{-8} M_\odot \text{ yr}^{-1}$, or approximately 0.1% of the total wind by mass.

Within different colliding wind binary systems, dust may form either continuously or periodically. Whilst the exact mechanism for this condition is not currently known, there is a strong correlation between periodicity and eccentricity, with less eccentric systems forming dust continuously, while highly elliptic systems exhibit periodic dust formation. Due to this orbital dependency, it is likely that there is an optimal dust forming separation, where dust can form in large quantities. This could be due to factors such as strong post shock cooling, which is highly dependent on the wind speed and orbital separation. Additionally, dust may be protected from the bulk of the stellar radiation due to the extremely large degree of extinction from the dense post-shock environment.

4.1 Introduction

Direct observation of dust forming CWBs and in particular the Wind Collision Region (WCR) is exceptionally difficult for a number of reasons:

- WR+OB CWB systems are extremely rare, of the 667 catalogued WR stars at time of writing, 106 have been confirmed to be in a binary system (Rosslowe & Crowther, 2015).
- A WC star is required for dust formation, no Nitrogen sub-type Wolf-Rayet (WN) have been observed to form dust. At time of writing 41 WR binaries contain WC stars.
- Not all WC+OB systems are dust producing, limiting the sample size further.
- Galactic CWB systems are comparatively distant from earth. For instance, WR 104, a well-studied system, is ~ 2.5 kpc distant. This prevents observations of these systems at a high angular resolution.
- Based on work by Zubko (1998) of CWB systems it appears that grain growth from small nucleation grains is quite rapid, this means that studying the initial grain evolution requires extremely high angular resolution observations.

For these reasons, numerical simulations are useful for modelling the growth of dust grains within this unresolved region. In order to better understand what influences dust production in a CWB system, a parameter space exploration of the wind and orbital parameters was performed. In particular the orbital separation, mass-loss rate and wind velocity were modified for both stars in order to influence the wind momentum ratio, η , and the cooling parameter, χ . The wind momentum ratio is defined as

$$\eta = \frac{\dot{M}_{\text{OB}} v_{\text{OB}}^{\infty}}{\dot{M}_{\text{WR}} v_{\text{WR}}^{\infty}}, \quad (4.1)$$

where \dot{M} is the mass loss rate of a star and v^{∞} is the terminal velocity of a star's outflow. A low value for η indicates that the winds are extremely imbalanced, with one star dominating the wind dynamics of the system. The wind momentum ratio sets for a given orbital separation, d_{sep} , the distance from each star to the apex of the wind collision

$$r_{\text{WR}} = \frac{1}{1 + \eta^{1/2}} d_{\text{sep}}, \quad (4.2a)$$

$$r_{\text{OB}} = \frac{\eta^{1/2}}{1 + \eta^{1/2}} d_{\text{sep}}. \quad (4.2b)$$

4. A PARAMETER SPACE EXPLORATION OF DUST FORMATION

In the case of a very small wind momentum ratio the primary star's wind completely envelopes the secondary stars forming an approximately conical WCR surface. The half-opening angle of this surface can be estimated by

$$\theta_c \simeq 2.1 \left(1 - \frac{\eta^{2/5}}{4}\right) \eta^{-1/3} \quad \text{for } 10^{-4} \leq \eta \leq 1, \quad (4.3)$$

to a high degree of accuracy (Eichler and Usov, 1993, but also see Pittard and Dawson, 2018). The cooling parameter, χ , compares the cooling time to the escape time from the shock region for a parcel of gas in the immediate post-shock environment. An approximation can be made using the known parameters of a system using the equation:

$$\chi = \frac{t_{\text{cool}}}{t_{\text{esc}}} \approx \frac{v_8^4 d_{12}}{\dot{M}_{-7}}, \quad (4.4)$$

where v_8 is the wind terminal velocity in units of 10^8 cm s^{-1} , d_{12} is the distance to the WCR apex in units of 10^{12} cm , and \dot{M}_{-7} is the mass loss rate in units of $10^{-7} M_\odot \text{ yr}^{-1}$ (Stevens et al., 1992). Small values of χ indicate that radiative cooling is very important, while $\chi \gg 1$ indicates an adiabatic system. Strong cooling occurs in comparatively slow, dense winds and is aided by a high metallicity. As such in many systems the post-shock WR flow will rapidly cool from the immediate post-shock temperature of 10^8 K to temperatures in the dust formation range, $\lesssim 10^4 \text{ K}$. A strongly radiating WCR can be compressed far more as it loses energy. In comparison, an adiabatic WCR is limited to a maximum density increase of a factor of 4 above the pre-shock wind density for $\gamma = 5/3$. This, combined with the reduction in gas temperature results in rapid dust growth and protection from the stellar UV radiation.

4.2 Methodology

Numerical simulations within this paper utilise the Athena++ hydrodynamical code, a highly modular modern fluid dynamics code (Stone et al., 2020). Simulations are generated in 3D and the Euler hydrodynamical equations are solved in the form:

$$\frac{\partial \rho}{\partial t} + \nabla \cdot (\rho \mathbf{u}) = 0, \quad (4.5a)$$

$$\frac{\partial \rho \mathbf{u}}{\partial t} + \nabla \cdot (\rho \mathbf{u} \mathbf{u} + P) = 0, \quad (4.5b)$$

$$\frac{\partial \rho \varepsilon}{\partial t} + \nabla \cdot [\mathbf{u} (\rho \varepsilon + P)] = \dot{E}_{cool}, \quad (4.5c)$$

where ε is the total specific energy ($\varepsilon = \mathbf{u}^2/2 + e/\rho$), ρ is the mass density, e is the internal energy density, P is the gas pressure and \mathbf{u} is the gas velocity. In order to simulate radiative losses, the parameter \dot{E}_{cool} is included, which is the energy loss rate per unit volume from the fluid due to gas and dust cooling, which is elaborated on in section 4.2.1.

Athena++ has been configured to run using a piecewise linear reconstruction method with a 4th order Strong Stability Preserving Runge-Kutta time-integration method (Spiteri & Ruuth, 2002). Athena++ was forked from the original repository and additional routines were written for a Colliding Wind Binary case. Routines were created to produce a steady outflow from a small spherical region around a set of cartesian co-ordinates as well as a function to move these co-ordinates with each time-step; these were used to simulate stellar wind outflow and orbital motion, respectively. Additionally, Athena++ was further modified to include an advected scalar dust model for simulating dust growth and destruction as well as a photon emission cooling model to approximate cooling for gas and dust particles within the fluid.

Athena++ utilises OpenMPI for parallelism, breaking the simulation into blocks, which are distributed between processors. The block size is variable, but for these simulations a block size of $32 \times 32 \times 8$ was found to be optimal. This meshblock system is also utilised in mesh refinement for increasing effective resolution. As the CWB systems are being simulated in their entirety, a very large volume needs to be simulated, while at the same time the region between the stars must be resolved with a resolution of at least 100 cells in order to adequately resolve the WCR. This difference in length scales necessitates the use of static mesh refinement (SMR) to improve the effective resolution of the simulation. A base coarse resolution of $320 \times 320 \times 40$ cells is defined for the simulations, while a region close to the binary pair operates at a higher refinement level, resulting in a resolution increase with a factor of 2^{n-1} greater than the coarse resolution, where n is the refinement level (figure 4.1). In the case of 7 levels as used in most of the simulations in this chapter, this results in an effective resolution of $20480 \times 20480 \times 2560$ cells. SMR is utilised instead of Adaptive Mesh Refinement, a more flexible conditional method, as it has proven to be more reliable within Athena++. As much of the grain evolution occurs

4. A PARAMETER SPACE EXPLORATION OF DUST FORMATION

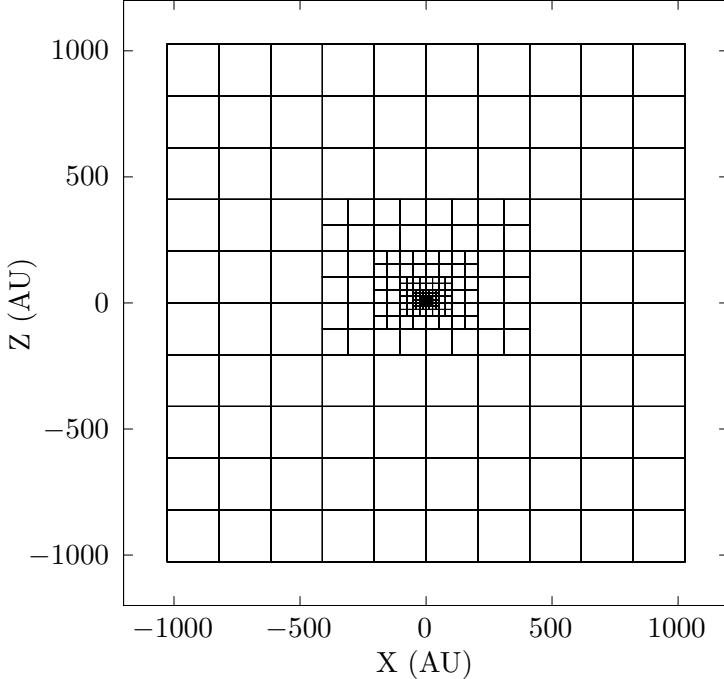


Figure 4.1: Plot of blocks used in a 7 level simulation with a block size of $32 \times 32 \times 8$ cells.
The block density increases dramatically closer to the barycentre.

a small distance from the WCR stagnation point, much of the simulation can be run at a lower resolution without affecting the simulation outcome.

The wind outflow from each star is simulated by replacing the conserved variables (density, momentum and energy) within a small region around the expected position of the stars; this region is typically on the order of 6 maximally refined cells in radius. This rewrite corresponds to a change in mass and mechanical energy imparted by an outflowing wind, such that

$$\rho_R = \frac{\dot{M}}{(4\pi r^2 v_\infty)}, \quad (4.6a)$$

$$P_R = \rho_R v_\infty, \quad (4.6b)$$

$$E_R = \frac{P_R}{\gamma - 1} + \frac{1}{2} \rho_R v_\infty^2, \quad (4.6c)$$

where v_∞ is the wind velocity as it flows radially from the center of the “remap zone”, P_R is the

remap pressure, $P_R = \rho_R k_B T_w / \mu m_H$, T_w is the wind temperature and r is the distance from the current cell to the centre of the remap zone. Orbits are calculated by moving the remap zones in a manner consistent with Keplerian dynamics, which are repositioned at the start of every timestep.

4.2.1 Gas and dust cooling

Cooling due to photon emission from atoms, ions and free electrons, as well as dust particles is simulated by removing energy from a cell at each timestep. The total energy loss is calculated by integrating the energy loss rates due to gas, plasma and dust cooling using the Euler method; in regions with very rapid cooling sub-stepping is used to improve accuracy, with the number of sub-steps being determined by comparing the substep time to the cooling timescale of the cell. Gas cooling is simulated using a lookup table method. A data file containing the gas temperature and associated normalised emissivity, $\Lambda(T)$ of the wind at that temperature is read into the simulation. In a typical cooling step, the temperature is calculated and compared with the lookup table to find the closest temperature bins that are lower and higher than the cell temperature. A linear interpolation is then performed to find an appropriate value for Λ . Energy loss can then be calculated with the formulae:

$$\frac{dE}{dt} = \left(\frac{\rho}{m_H} \right)^2 \Lambda_w(T), \quad (4.7)$$

where ρ is the gas density and m_H is the mass of a hydrogen atom. The lookup table was generated by mixing a series of cooling curves generated by MEKAL simulations of elemental gasses. These simulations were combined based on the elemental abundances of each wind, with the WC star having typical WC9 abundances and the OB star having a solar abundance. Figure 4.2 shows the cooling curves used for each star. Two lookup tables are used in the simulations, based on the elemental abundances of each star. The most significant abundances used in this projects simulations are presented in table 4.1. The cooling regime of this code ranges from 10^4 to 10^9 K. A floor temperature of 10^4 K is implemented, temperatures between $1 \times 10^4 \text{ K} < T \leq 1.1 \times 10^4 \text{ K}$ are reduced to 10^4 K as they are assumed to be either rapidly cooling or a part of the stellar wind.

A model for cooling due to emission from dust grains is also included as dust cooling is expected to play a significant role in the evolution of each system. The rate of cooling is

4. A PARAMETER SPACE EXPLORATION OF DUST FORMATION

	X(E)	
	Solar	WC9
H	0.705	0.0
He	0.275	0.546
C	3.07×10^{-3}	0.4
N	1.11×10^{-3}	0.0
O	9.60×10^{-3}	0.05

Table 4.1: Abundances used for the OB and WR stars being simulated, other elements are assumed trace when calculating radiative energy loss due to dust.

calculated using the uncharged grain case of the Dwek and Werner (1981) prescription. Grains are heated due to collisions with ions and electrons, causing them to radiate, with energy being removed from the simulation. This assumes that the region being simulated is optically thin to far infrared photons. The grain heating rate is calculated with the following formulae:

$$H = 1.26 \times 10^{-19} \frac{n}{A^{1/2}} a^2 (\mu\text{m}) T^{3/2} h(a, T), \quad (4.8)$$

where H is the heating rate due to atom and ion collisions, n is the particle number density, A is the mass of the incident particle in amu, $a(\mu\text{m})$ is the grain radius in microns, T is the temperature of the ambient gas, and $h(a, T)$ is the effective grain “heating factor”, also referred to as the grain transparency.

In the case of collisional heating with incident atoms, H_{coll} , heating rates are summated for Hydrogen, Helium, Carbon, Nitrogen and Oxygen atom collisions:

$$H_{\text{coll}} = H_H + H_{He} + H_C + H_N + H_O. \quad (4.9)$$

Other elements are not considered as they are present in trivial proportions in both winds. As a neutral grain is assumed, the grain transparency for each species is calculated with the formulae:

$$h(a, T) = 1 - \left(1 + \frac{E_0}{2k_B T}\right) e^{-E_0/k_B T}, \quad (4.10)$$

where E_0 is the initial energy required to overcome the grain’s potential and k_B is the Boltzmann

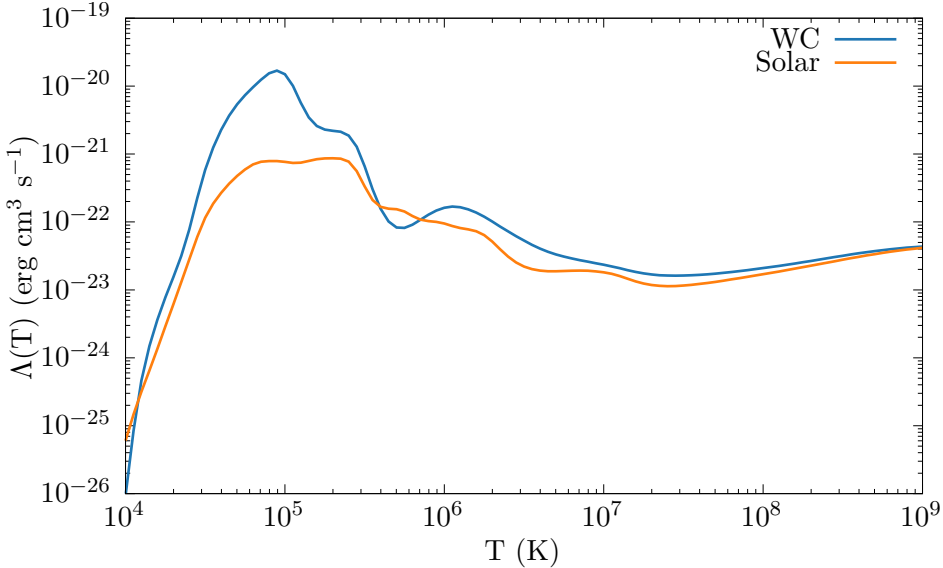


Figure 4.2: Comparison of cooling curves for calculating energy loss due to gas cooling.

constant.

Electron-grain collisional heating, H_{el} , is modelled using the same calculation for H , albeit with some differences. One major factor for calculating accurate energy loss due to electron collisions is that the electron number density needs to be accurately calculated; this is performed with a second series of lookup tables that contain the electron-to-ion ratio of each wind across a temperature range of 10^4 to 10^9 K (figure 4.3). The electron number density is found to be $n_e = \beta n_i$ where β is the electron-to-ion ratio and n_i is the ion number density. Another difference between calculating electron-grain and gas-grain cooling is calculating electron-grain transparency, which is a significantly more complex problem than calculating ion-grain transparency. An assumed full opacity proves to be extremely inaccurate at temperatures $> 10^6$ K. Electron-grain transparency is therefore calculated via an approximation described in Dwek and Werner (1981):

$$\begin{aligned} h(x^*) &= 1, & x^* > 4.5, \\ &= 0.37x^{*0.62}, & x^* > 1.5, \\ &= 0.27x^{*1.50}, & \text{otherwise,} \end{aligned} \tag{4.11}$$

where $x^* = 2.71 \times 10^8 a^{2/3} (\mu\text{m}) / T$. This approximation is approximately 4 orders of magnitude

4. A PARAMETER SPACE EXPLORATION OF DUST FORMATION

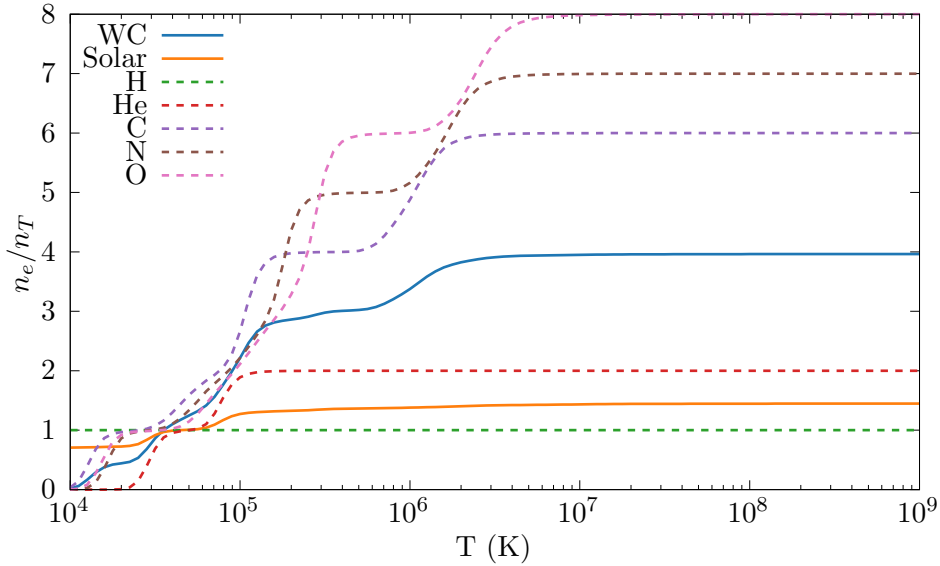


Figure 4.3: A comparison of the electron-ion ratio of both winds as the temperature changes. Included are the pure wind flows that the lookup tables are built from.

faster than using an integration method, while only being out by $\sim 8\%$ in the worst case scenario (figure 4.4). Grain-grain collisions are not modelled, as this would be difficult to calculate due to the single-fluid model in use. Further simulations utilising a multi-fluid model could allow for this to be simulated.

Finally, in order to calculate the change in energy due to dust cooling, the rate of energy change, dE/dt is calculated using the formulae:

$$\Lambda_d = \frac{H_{\text{coll}} + H_{\text{el}}}{n_H}, \quad (4.12a)$$

$$\frac{dE}{dt} = n_T n_d \Lambda_d, \quad (4.12b)$$

where Λ_d is then normalised dust emissivity, n_H is the hydrogen density, n_T is the total density and n_d is the dust density.

4.2.2 Numerical modelling of dust through advected scalars

The most important modification to Athena++ was the addition of a dust growth and destruction model to simulate the production of dust within the WCR. A series of passive scalars were

4.2 Methodology

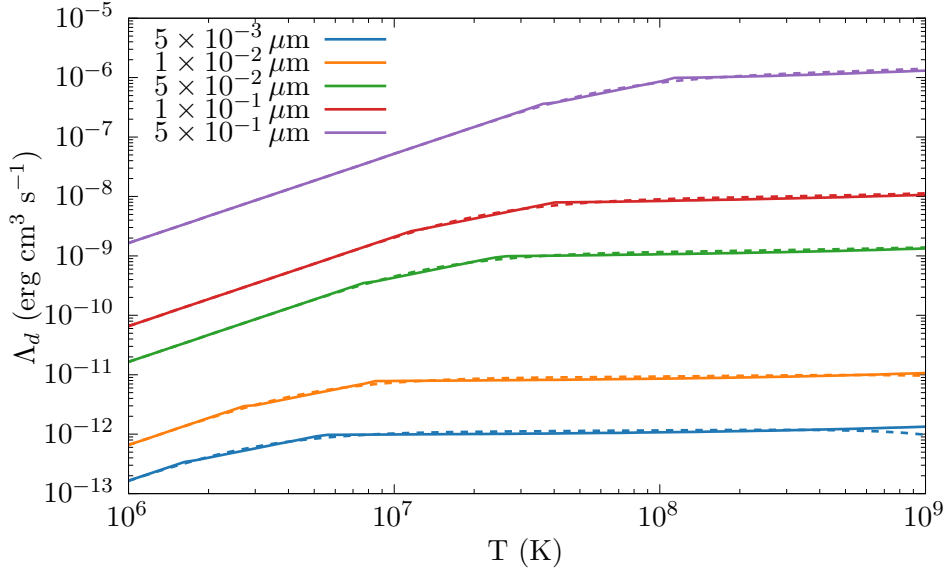


Figure 4.4: Λ_d as a function of temperature for various grain sizes. The estimate method (dashed line) is extremely close to the integral value (solid line) aside from at the highest temperatures.

used where the dust parameters described by the scalars can evolve and advect through the simulation, analogous to a co-moving fluid, which previous papers have noted is an accurate dynamical model for dust within the WCR (Hendrix et al., 2016). In these simulations, dust is stored in the form of two variables, the average grain radius, a , and the dust-to-gas mass ratio, z . From these constants the dust production rate, number density, and total dust mass can be derived. A co-moving model allows for a simplified model of dust formation. In such a model, the mean particle velocity between two particles of different size can be given as:

$$\langle u \rangle = \left[\frac{8kT}{\pi m_r} \right]^{1/2}, \quad (4.13)$$

where m_r is the familiar reduced mass between a test particle of mass m_t and a field particle of mass m_f

$$m_r = \frac{m_f m_t}{m_f + m_t}. \quad (4.14)$$

As the dust grain is significantly more massive, the reduced mass is approximately equal to the grain mass, simplifying the dynamics of the simulation in a co-moving case. Dust growth is

4. A PARAMETER SPACE EXPLORATION OF DUST FORMATION

modelled through approximating growth due to grain-gas accretion where grains co-moving with a gas perform relatively low-velocity collisions with the surrounding gas, causing it to accrete onto the surface of the dust grain (Spitzer Jr., 2008). Assuming a single average grain size the change in average grain radius is given by

$$\frac{da}{dt} = \frac{\xi_a \rho_{Gr} w_a}{4\rho}, \quad (4.15)$$

where w_a is the Maxwell-Boltzmann distribution RMS velocity, ξ_a is the grain sticking efficiency and ρ_{Gr} is the grain bulk density. The associated rate of dust density change is found to be

$$\frac{d\rho_D}{dt} = 4\pi a^2 \rho_g n_D \frac{da}{dt}, \quad (4.16)$$

where ρ_g is the gas density and n_D is the grain number density. In this paper we take $\xi_a = 0.1$ as a conservative value, though this value can rise to as high as 1 in the case of highly charged grains. A bulk density analogous to amorphous carbon grains of 3 g cm^{-3} is also used.

Dust destruction is calculated via gas-grain sputtering using the Draine and Salpeter (1979) prescription - a dust grain has a lifespan, τ , which is dependent on the grain radius. Assuming a spherical grain, the rate of change in mass and radius can be calculated such that:

$$\tau_D = 1 \text{ Myr} \times \frac{a}{n_g}, \quad (4.17a)$$

$$\frac{da}{dt} = -\frac{a}{\tau_D}, \quad (4.17b)$$

$$\frac{dm}{dt} = -1.33 \times 10^{-13} a^2 n_g n_d \rho_{Gr}, \quad (4.17c)$$

where n_g is the gas number density.

In order to propagate dust through each simulation, a small initial value for the advected scalars is set in each cell in the remap zones. A minimum grain radius of 50 \AA and minimum dust-to-gas mass ratio of 10^{-6} is imposed. Changing z_{min} does not significantly impact the final dust-to-gas mass ratio of the system as z rapidly increases within the WCR and dust growth in the WCR dominates the total production.

Parameter	WR	OB	Unit
\dot{M}	5.0×10^{-6}	5.0×10^{-8}	$M_{\odot} \text{ yr}^{-1}$
v_{∞}	1.0×10^8	2.0×10^8	cm s^{-1}
T_w	1.0×10^4	1.0×10^4	K

Table 4.2: Wind properties of the baseline system.

Parameter	Value	Unit
$M_{\text{WR}} \& M_{\text{OB}}$	10.0	M_{\odot}
d_{sep}	4.0	AU
P	1.80	yr

Table 4.3: Baseline system orbital properties.

4.3 Model Parameters

In this chapter we do not intend on modelling particular systems. Rather we intend to gain a deeper understanding of what the primary influences of dust formation are in a CWB system. A series of simulations were therefore run in order to determine how dust formation varies due to changes in orbital separation and wind momentum ratio. A baseline simulation with properties similar to WR98a with a circular orbit and identical stellar masses was created. Additionally, this baseline simulation has a momentum ratio of 0.02. Other simulations were then run with different orbital separations and/or wind momentum ratios. Another set of simulations were run where the cooling mechanisms were selectively disabled, in order to understand how radiative cooling effects the dust production rate. Tables 4.2 and 4.3 detail the wind and orbital parameters of the baseline simulation. The orbital separation is modified by changing the orbital period of the simulation, while the wind momentum ratio is modified by adjusting the mass loss ratio and wind terminal velocity for each star. Two simulation sub-sets for this were performed, simulations where the wind terminal velocities were adjusted for each star and simulations where the mass loss rates for each star were adjusted.

4.3.1 Cooling mechanisms

For this set of simulations, the influence of cooling was changed by varying how cooling works within the simulations. All simulations in this set keep the same orbital and wind parameters,

4. A PARAMETER SPACE EXPLORATION OF DUST FORMATION

Name	Plasma cooling	Dust cooling
<code>fullcool</code>	Yes	Yes
<code>plasmacool</code>	Yes	No
<code>nocool</code>	No	No

Table 4.4: Cooling series simulation parameters

which are that of the baseline system described in tables 4.2 & 4.3. One simulation has both plasma and dust cooling in operation (the `fullcool` simulation), while the other two simulations have plasma cooling only and no cooling respectively (`plasmacool` and `nocool`, table 4.4). The final, no radiative cooling simulation instead relies on adiabatic expansion for temperature change; as such, this simulation behaves as if it has a χ value for both winds that is arbitrarily high. The post-shock flow in the `nocool` model will also be unable to compress as much due to the lack of energy loss via radiative cooling. The role of these simulations is to discern whether it is cooling alone or other system parameters that affects dust production.

4.3.2 Wind momentum ratio

Another set of simulations was devised in order to assess the influence of the wind parameters on the formation of dust within a CWB. As the wind momentum ratio is dependent on both the mass loss rate and wind velocity of each star, each of these properties is modified over a course of simulations. η is varied from 0.01 to 0.04 by adjusting the wind parameters for each star. This is further subdivided by which property is modified, either the mass loss rate (table 4.5) or wind terminal velocity (table 4.6). As the cooling parameter has a much stronger dependency on v_∞ than \dot{M} , the modification of either parameter while maintaining a similar value for η allows us to determine whether the cooling parameter is the primary characteristic determining the formation of dust within WCd systems. This can be seen when comparing simulations `mdot-1` and `vinf-1`, which have similar wind momentum ratios but the cooling parameters for the WC star differ by a factor of 32. These simulations are compared to the baseline simulation, which has a radiative post-shock WCR. Whilst the simulations with $\eta = 0$ still have very imbalanced winds, they are typical of a WR+OB binary with a less intense Wolf-Rayet partner star wind. All simulations were run for a minimum of 1 orbit. As these orbits are circular, there should be no major variance of the winds after the start-up transients are fully advected, save for some fluctuations.

4.3 Model Parameters

Name	\dot{M}_{WR}	\dot{M}_{OB}	v_{WR}^∞	v_{OB}^∞	η	χ_{WR}	χ_{OB}
	$M_\odot \text{ yr}^{-1}$	$M_\odot \text{ yr}^{-1}$	cm s^{-1}	cm s^{-1}			
baseline	5.0×10^{-6}	5.0×10^{-8}	1×10^8	2×10^8	0.02	1.20	1915
mdot-1	1.0×10^{-5}	5.0×10^{-8}	1×10^8	2×10^8	0.01	0.60	1915
mdot-2	2.5×10^{-6}	5.0×10^{-8}	1×10^8	2×10^8	0.04	2.39	1915
mdot-3	5.0×10^{-6}	1.0×10^{-7}	1×10^8	2×10^8	0.04	1.20	957
mdot-4	5.0×10^{-6}	2.5×10^{-8}	1×10^8	2×10^8	0.01	1.20	3830

Table 4.5: Wind parameters for simulations varying the mass loss rate, \dot{M} .

Name	\dot{M}_{WR}	\dot{M}_{OB}	v_{WR}^∞	v_{OB}^∞	η	χ_{WR}	χ_{OB}
	$M_\odot \text{ yr}^{-1}$	$M_\odot \text{ yr}^{-1}$	cm s^{-1}	cm s^{-1}			
baseline	5×10^{-6}	5×10^{-8}	1×10^8	2×10^8	0.02	1.20	1915
vinf-1	5×10^{-6}	5×10^{-8}	2×10^8	2×10^8	0.01	19.1	1915
vinf-2	5×10^{-6}	5×10^{-8}	5×10^7	2×10^8	0.04	0.07	1915
vinf-3	5×10^{-6}	5×10^{-8}	1×10^8	4×10^8	0.04	1.20	30638
vinf-4	5×10^{-6}	5×10^{-8}	1×10^8	1×10^8	0.01	1.20	120

Table 4.6: Wind parameters for simulations varying the wind terminal velocity, v^∞ .

4. A PARAMETER SPACE EXPLORATION OF DUST FORMATION

4.3.3 Separation distance

A final series of simulations was performed with the wind parameters equivalent to the baseline model, but with differing orbital separations. The separation was altered by modifying the orbital period of each star, as stellar masses were to be kept realistic. The separation distance was varied from the baseline model of 4 AU to 64 AU (table 4.7), which has the effect of modifying the cooling parameter of each simulation without changing the wind momentum ratio; allowing us to further discern which is the dominant parameter influencing dust formation. For instance, simulation `dsep-64AU` has a cooling parameter value approaching the fast WR wind model `vinf-1`, despite having a wind momentum ratio of 0.02.

Each simulation has a coarse resolution of $320 \times 320 \times 40$ cells, with a varying number of levels, as the separation distance is doubled, the associated static mesh refinement box is halved and the number of levels is decremented. This manipulation of levels ensures that the number of cells between the stars is kept consistent, reduces memory usage and keeps the average timestep approximately the same. The simulation extent was doubled over the previous simulations, to approximately $2000 \times 2000 \times 250$ AU. Similarly to the previous set of simulations, a minimum of 1 orbit was needed for each simulation, however, as the orbital period of each simulation varies, certain simulations were able to run for a significantly longer length of time, with data for multiple orbits being obtained.

Name	P yr	d_{sep} AU	χ_{WR}	χ_{OB}	Levels	Effective Resolution
						Cells
<code>dsep-4AU</code>	1.80	4	1.20	1915	7	$20480 \times 20480 \times 2560$
<code>dsep-8AU</code>	5.06	8	2.39	3830	6	$10240 \times 10240 \times 1280$
<code>dsep-16AU</code>	14.3	16	4.79	7659	5	$5120 \times 5120 \times 640$
<code>dsep-32AU</code>	40.5	32	9.57	15319	4	$2560 \times 2560 \times 320$
<code>dsep-64AU</code>	115	64	19.1	30638	3	$1280 \times 1280 \times 160$

Table 4.7: Parameters of simulations varying separation distance.

4.3.4 Data collection

HDF5 files were generated at regular time intervals - 3D HDF5 meshes were generated every $1/100^{\text{th}}$ of an orbit, while 2D slices were produced every $1/1000^{\text{th}}$ of an orbit. These HDF5

files contain the primitive variables of the simulation, gas density, ρ , gas pressure, P and wind velocity components, v_x , v_y and v_z . These variables were then used to derive other variables such as temperature and energy. The scalars governing the dust properties were also stored for each cell, the dust-to-gas mass ratio, z and the dust grain radius, a . The wind “colour”, the proportion of gas resultant from each star, was also tracked. A value of 1.0 indicates a pure WR wind while 0.0 indicates a pure OB wind.

The volume-weighted summations of all system parameters were also collected, such as the total system mass and average grain radius, in order to derive average values, such as \bar{z} and \bar{a} from this data, the values for each can be divided by the total system mass. To calculate dust formation within the WCR, a method of determining if a cell was a part of the wind collision region was devised - the cell density would be compared to the predicted density of a single smooth wind with the wind parameters of the WC star in the system:

$$\rho_{WC} = \frac{\dot{M}_{WC}}{4\pi r^2 v_{WC}^\infty}, \quad (4.18)$$

where r is the distance from the barycentre, this threshold value was set to $1.25\rho_{SW}$. Higher threshold values were found to be inaccurate at large distances from the barycentre (figure 4.5). Other methods of detecting the Wind Collision Region such as determining wind mixing levels were not successful in general.

4.4 Results

The first set of simulations were performed in order to assess whether the implemented cooling model would influence dust formation within the WCR. This was found to be the case, figure 4.6 shows that without cooling only a marginal amount of dust formation occurs. Dust production for both radiative simulations with cooling processes were significantly higher, with the `fullcool` simulation having consistently higher dust formation rates than the `plasmacool` simulation. This is a sensible result, as figure 4.7 shows that at immediate post shock temperatures nascent dust grains present can influence immediate post-shock cooling, allowing the wind to reach temperatures low enough for dust formation faster than if only plasma cooling was simulated.

In the case of the `fullcool` simulation, a peak dust formation rate of $7 \times 10^{-9} M_\odot \text{ yr}^{-1}$ was calculated, this fluctuation appears to be due to dust forming mostly in high density instabilities

4. A PARAMETER SPACE EXPLORATION OF DUST FORMATION

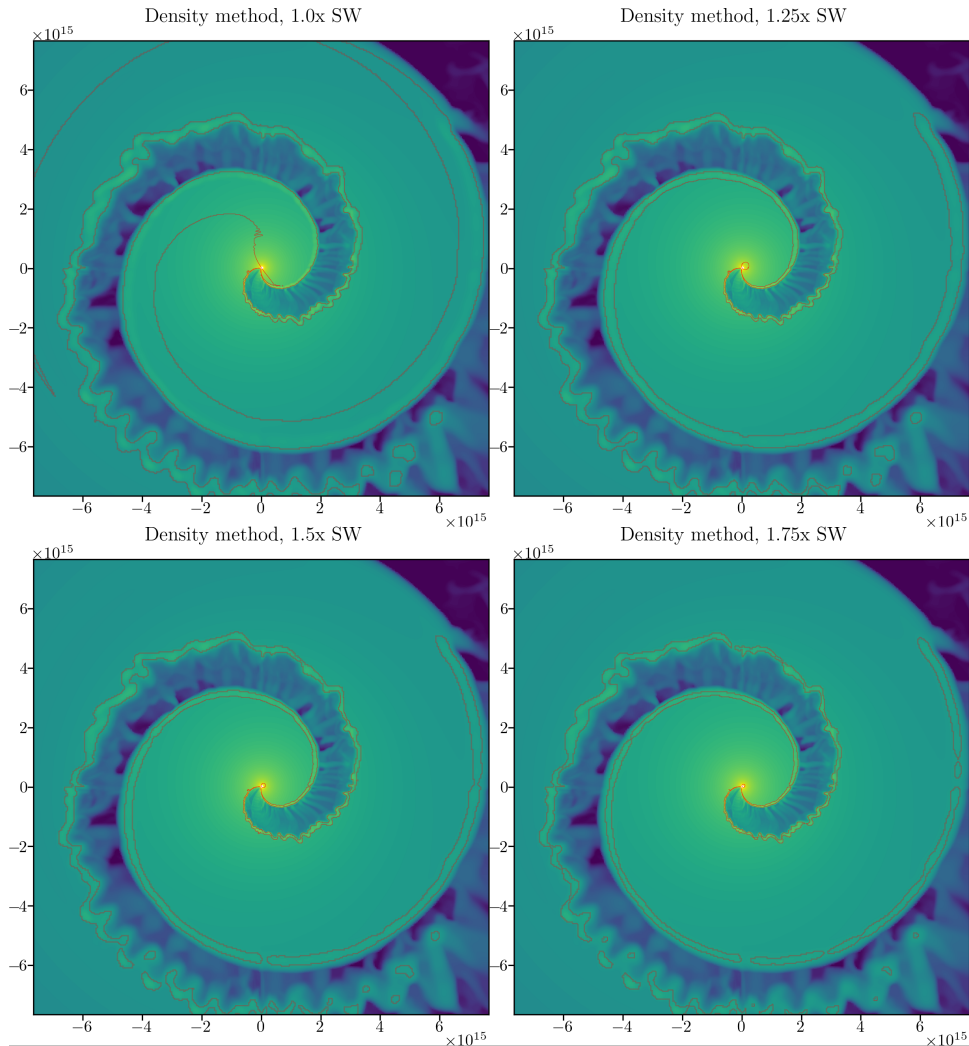


Figure 4.5: Comparison of threshold values for the over-density method of determining if a cell resides in the wind collision region. A threshold value of $1.25\rho_{\text{SW}}$ was chosen as it most accurately determined if the cell was in the post-shock region.

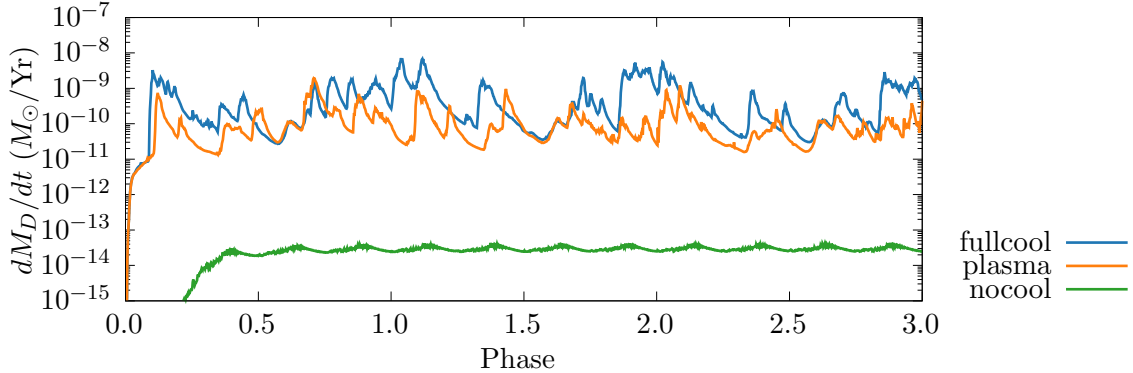


Figure 4.6: A comparison of dust formation rates as cooling mechanisms are changed. Without adequate cooling barely any dust is formed, while dust formation does increase with all cooling mechanisms enabled plasma cooling is still the dominant cooling process for dust production.

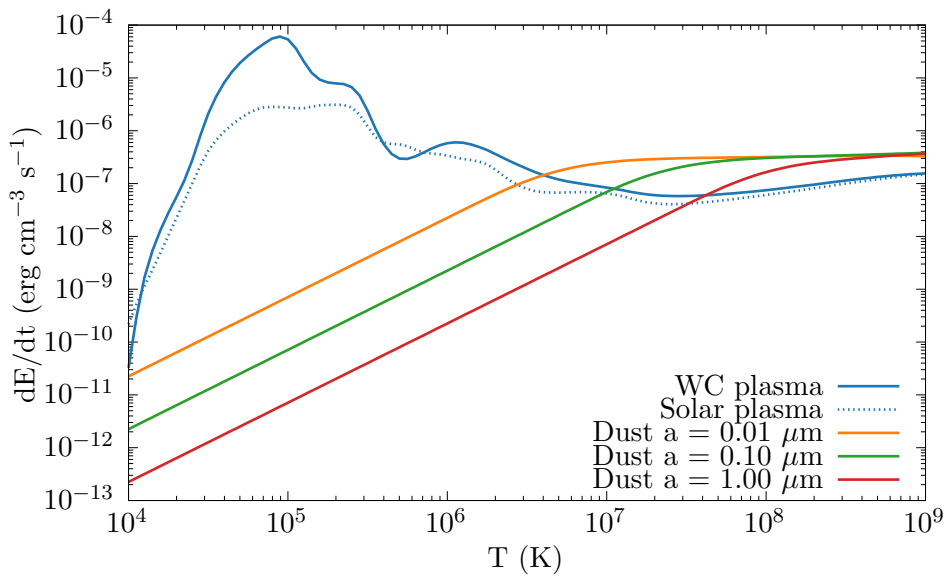


Figure 4.7: Comparison of energy loss due to plasma and dust cooling with varying grain sizes in a typical post-shock flow, where $\rho_g = 10^{-16} \text{ g cm}^{-3}$ and a dust-to-gas mass ratio of 10^{-4} is assumed. Whilst less influential at lower temperatures, dust cooling can aid cooling in the immediate post-shock environment.

4. A PARAMETER SPACE EXPLORATION OF DUST FORMATION

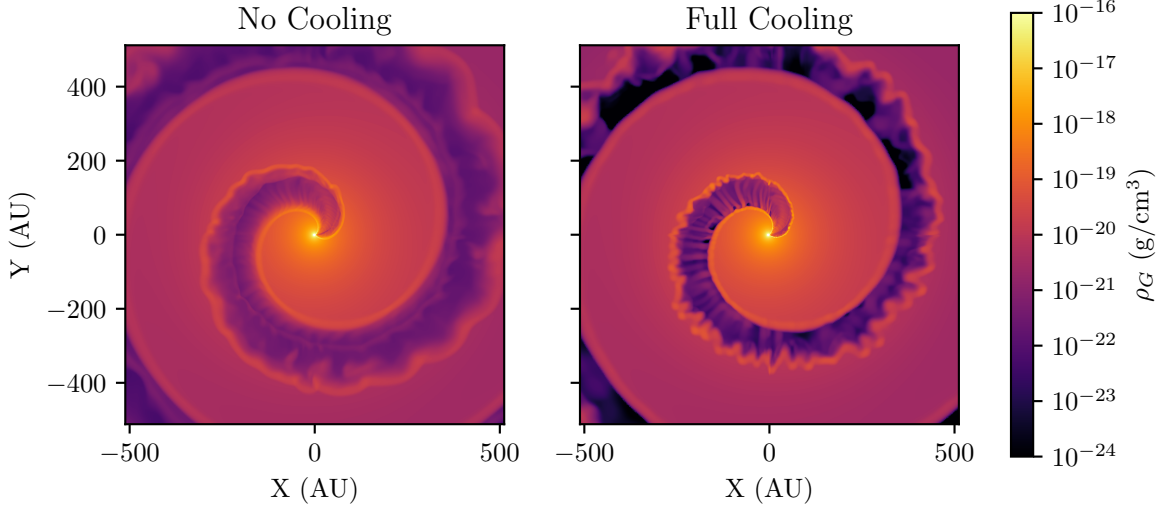


Figure 4.8: Density comparison for `nocool` and `fullcool` models, with cooling enabled instabilities are far more prevalent, with pockets of very high density material within the WCR.

(figures 4.6 & 4.8).

As cooling is significant in the post-shock WR wind, further compression occurs, resulting in much higher post-shock densities (figure 4.9). Gas rapidly cools within this post-shock region, corresponding to where energy losses were stated to be important in Usov (1991); this rapid cooling results in ideal conditions for dust formation, especially within high density instabilities. A similar effect for the OB wind is not observed, as radiative energy losses are not influential on the dynamics of the flow, due to the faster, significantly thinner stellar wind. Figure 4.10 shows that the `fullcool` simulation has a similar immediate-post shock temperature to an adiabatic model, however this region cools within an extremely short timescale, allowing the nascent dust grains to grow. Figure 4.11 shows dust clumps forming shortly after initial wind collision, these clumps rapidly convert post-shock gas to dust; however, rapid dust production tapers off as the post-shock flow becomes more diffuse. This behaviour is similar to previous models, which suggest that the bulk of dust formation occurs only a short distance from the parent stars. Temperature is also significantly more affected in the leading edge relative to the orbital motion, leading to a larger portion of dust forming in this region.

Pittard (2009) notes that in the case of colliding winds with $\eta = 1$ the trailing edge of the WCR takes part in oblique shocks with the stellar winds, while the leading edge is shadowed

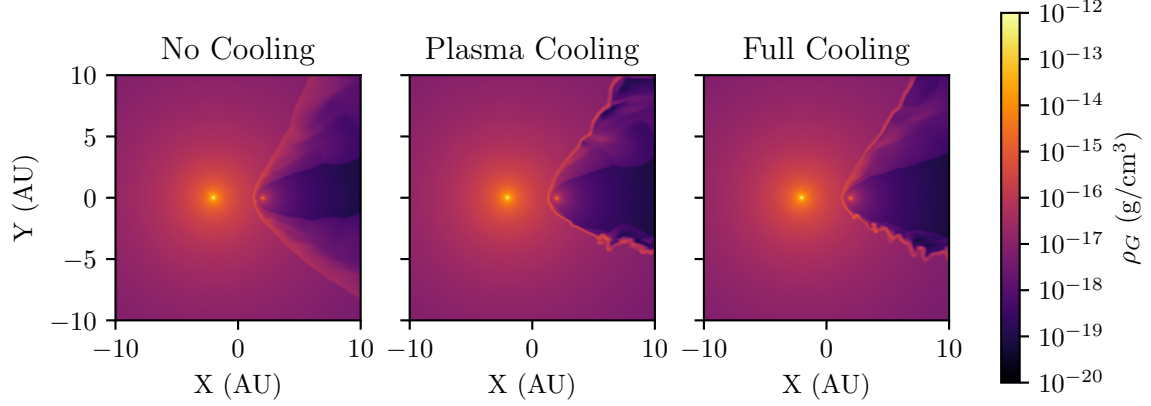


Figure 4.9: Density comparison of simulations with differing radiative processes.

Model	η	χ_{WR}	χ_{OB}	$\dot{M}_{\text{D},\text{avg}}$	$\dot{M}_{\text{D},\text{max}}$
				$M_{\odot} \text{ yr}^{-1}$	$M_{\odot} \text{ yr}^{-1}$
baseline	0.02	1.20	1915	5.38×10^{-10}	9.06×10^{-7}
plasma	0.02	1.20	1915	1.29×10^{-10}	9.06×10^{-7}
nocool	0.02	1.20	1915	2.71×10^{-14}	9.06×10^{-7}

Table 4.8: Rates of dust production for radiative simulation set.

by the upstream WCR from the colliding material. This results in a trailing edge with strong instabilities and cool, high density clumps of post-shock wind, while the leading edge has a low density flow that is not dominated by instabilities. This does not appear to occur in these low- η systems, as oblique shocks occur at a much greater distance, when the stellar wind is significantly less dense. Instead, the leading edge of the WCR appears to be much thinner and denser than the trailing edge, this is believed to be due to the leading edge interacting with the outflowing material due to the systems orbital motion, sweeping up material and obliquely shocking with the downstream WCR. Most dust formation occurs in this downstream post-shock region, as soon as it has sufficiently cooled. Furthermore, dust formation slows significantly as the post-shock wind begins to diffuse, limiting overall dust formation to a region around 100 AU from the WCR apex. This is in agreement with the research by Williams, van der Hucht, Thé et al. (1990) and Hendrix et al. (2016), which observed that there is a limited region suitable for dust formation.

4. A PARAMETER SPACE EXPLORATION OF DUST FORMATION

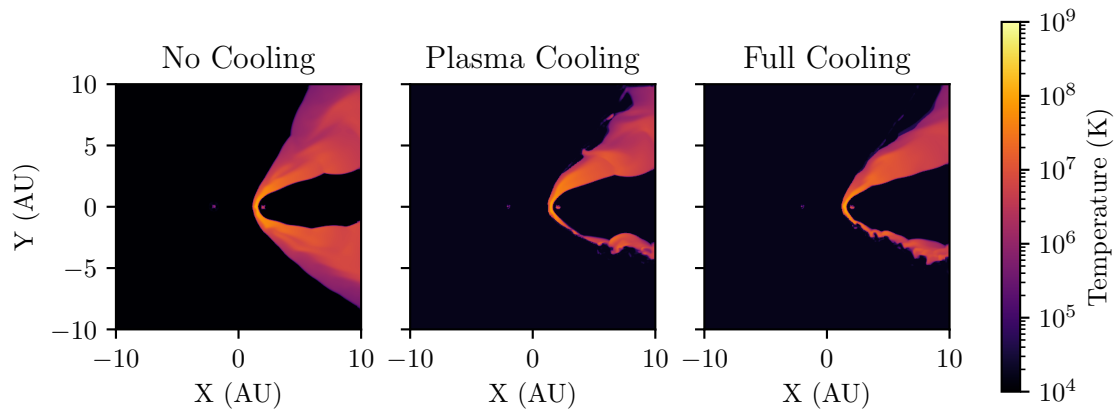


Figure 4.10: Temperature comparison of simulations with differing radiative processes.

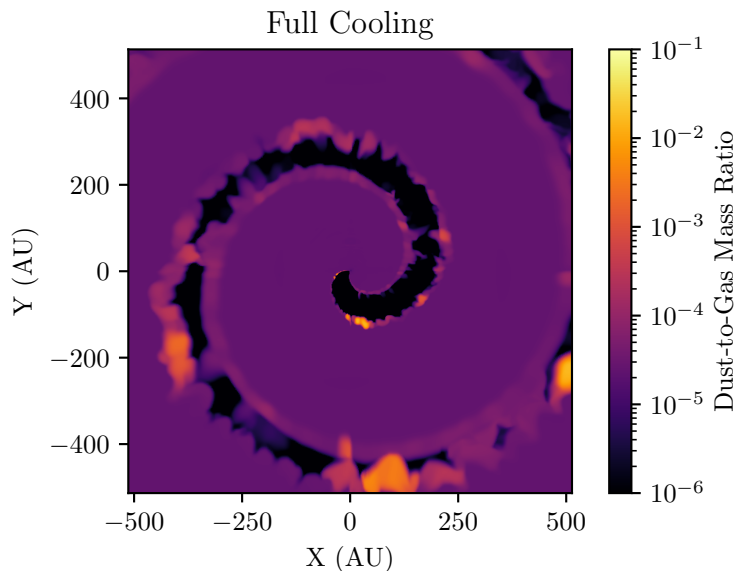


Figure 4.11: Full extent of baseline simulation, showing dust-to-gas mass ratio. Dust typically formed in clumps within instabilities, leading to variation of dust formation as the simulation progresses. Most of the dust forms in the leading arm of the WCR.

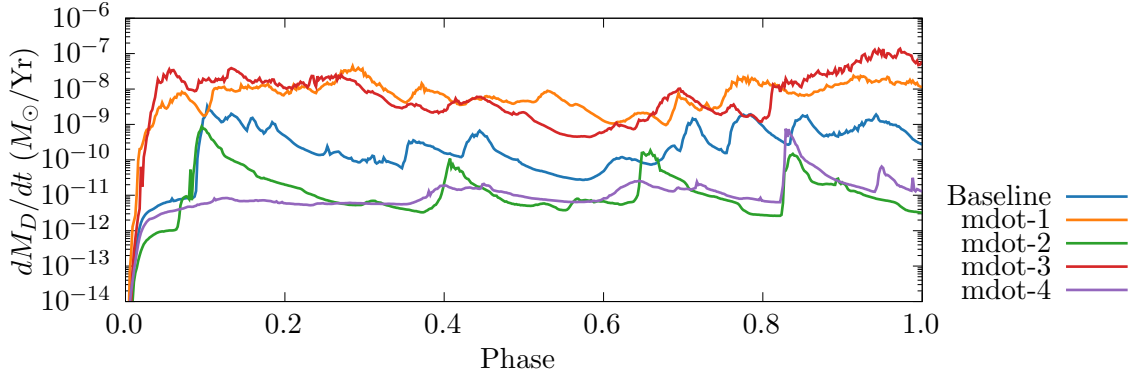


Figure 4.12: A comparison of dust production rates for simulations that vary mass loss rate, \dot{M} , simulations with either a strong primary or secondary wind produce similar levels of dust, whilst if either wind is weaker, dust production rate is reduced.

4.4.1 Mass loss rate variation

Dust formation in the mass loss variation simulations was found to be dependent on strong winds from either the WC or OB star. As can be seen in figure 4.12, the rates are stratified into similar dust production rates for simulations with increases or decreases in mass loss rates; simulations with either wind being stronger produced the most dust, while simulations with weaker winds produced approximately 3 orders of magnitude less dust than the most productive simulations. However, the heightened dust production rate does not correspond to the total mass loss rate of the system. For instance, `mdot-1` and `mdot-3` produce on average 2 orders of magnitude more dust with a combined mass loss rate with 1.99 and 1.01 times more wind than the baseline simulation. All simulations in this system have low values for χ_{WR} compared to other simulation sets, implying that cooling is not the only governing factor, and that a strong shock must also form.

4.4.2 Terminal velocity variation

Varying the wind terminal velocity appears to have an extremely strong effect on dust formation, with effects that are not solely related to cooling. The dust production rate is exceptionally high in the case of `vinf-2`, which has an extremely slow wind velocity of 500 km s^{-1} , closer to that of a typical LBV star rather than that of a WC. This very slow, dense wind is highly influenced by radiative cooling in the post-shock environment, driving thermal instabilities and leading to

4. A PARAMETER SPACE EXPLORATION OF DUST FORMATION

Model	η	χ_{WR}	χ_{OB}	$\dot{M}_{\text{D,avg}}$	$\dot{M}_{\text{D,max}}$
				$M_{\odot} \text{ yr}^{-1}$	$M_{\odot} \text{ yr}^{-1}$
baseline	0.02	1.20	1915	5.38×10^{-10}	9.06×10^{-7}
mdot-1	0.01	0.60	1915	8.79×10^{-9}	1.42×10^{-6}
mdot-2	0.04	2.39	1915	2.53×10^{-11}	5.83×10^{-7}
mdot-3	0.04	1.20	957	2.34×10^{-8}	1.17×10^{-6}
mdot-4	0.01	1.20	3830	3.81×10^{-11}	7.11×10^{-7}

Table 4.9: Rates of dust production for mass loss rate simulation set.

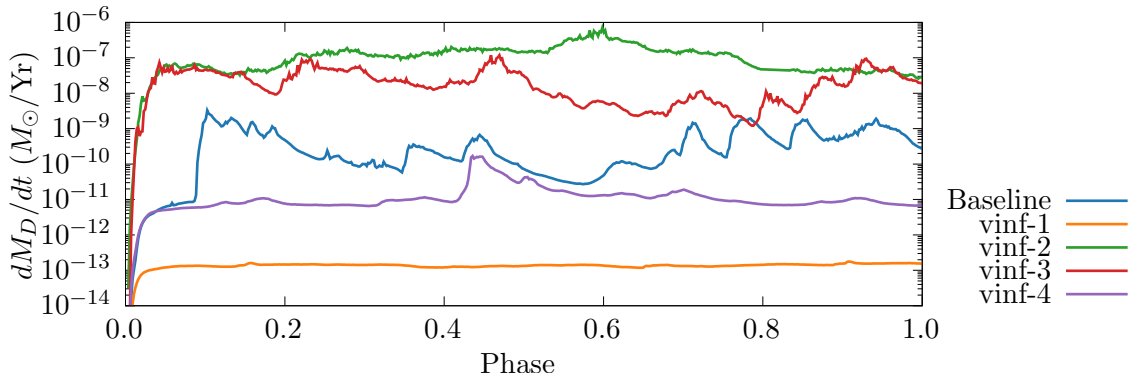


Figure 4.13: Comparison of dust production rate for simulations varying wind terminal velocity, v^{∞} . Simulations with strong wind velocity imbalance produce significantly more dust than their counterparts.

4.4 Results

high density pockets of cooled gas. This can be seen in figure 4.14, where v_{∞} -2 produces large quantities of dust near apex of the WCR on the WCR side, which is then mixed throughout the WCR. This flow is highly radiative and is quickly cooled back to the initial wind temperature. The factor of 4 wind velocity imbalance between the primary and secondary wind creates a strong velocity shear, leading to the formation of Kelvin-Helmholtz instabilities.

It should be noted that dust production in general increased outside of the WCR in the case of v_{∞} -2, this is largely due to significantly higher wind density within the WC wind, and increased formation time before wind collision. This dust would be destroyed via the photodissociation process, which is not included in this model, but would be included in future models if this avenue of research is continued. Despite this, the dust production outside of the WCR does not significantly impact the total dust production rate, and numerical analysis of dust production such as in figure 4.18 does not include dust produced outside of the wind collision region. In the case of a fast WC wind, dust production effectively ceases, with an average dust production rate of $9 \times 10^{-14} M_{\odot} \text{ yr}^{-1}$, 2 orders of magnitude less than v_{∞} -4, despite having a similar wind momentum ratio.

Simulations v_{∞} -3 and v_{∞} -4 show that when the secondary wind velocity was altered, drastic changes to the dust formation rate occurred, similar to modifying the mass loss rate of the secondary star. Instabilities due to the secondary wind appear to be the result of this, a greater secondary wind velocity would lead to a greater velocity shear along the discontinuity, resulting in Kelvin-Helmholtz instabilities in v_{∞} -3 but not in v_{∞} -4 (Stevens et al., 1992). Both v_{∞} -2 and v_{∞} -3 exhibit KH instabilities, and both have a terminal velocity ratio, $v_{\text{OB}}^{\infty}/v_{\text{WR}}^{\infty} = 4$. This would augment the already present thermal instabilities due to radiative cooling, leading to a less ordered, clumpy post-shock environment. This is found to be the case with v_{∞} -3, which has a far greater amount of dust formation within the WCR, and has a significantly more mixed wind. In figure 4.15 where v_{∞} -3 and v_{∞} -4 are directly compared, the presence of a much faster secondary wind results in a velocity shear that produces a much broader WCR, with high density pockets formed within instabilities, which appear to produce the bulk of dust, despite both simulations having an adiabatic second wind. This suggests that prolific dust formation occurs in a post-shock primary wind shaped by instabilities, produced either from strong radiative cooling, or through a strong velocity shear, leading to K-H instabilities. Radiative cooling is also important beyond thermal instabilities, reducing temperatures in the high-density immediate post shock flow so that dust can begin to form. Results appear to be stratified somewhat in terms of η , where simulations where $\eta = 0.04$ produce significantly more

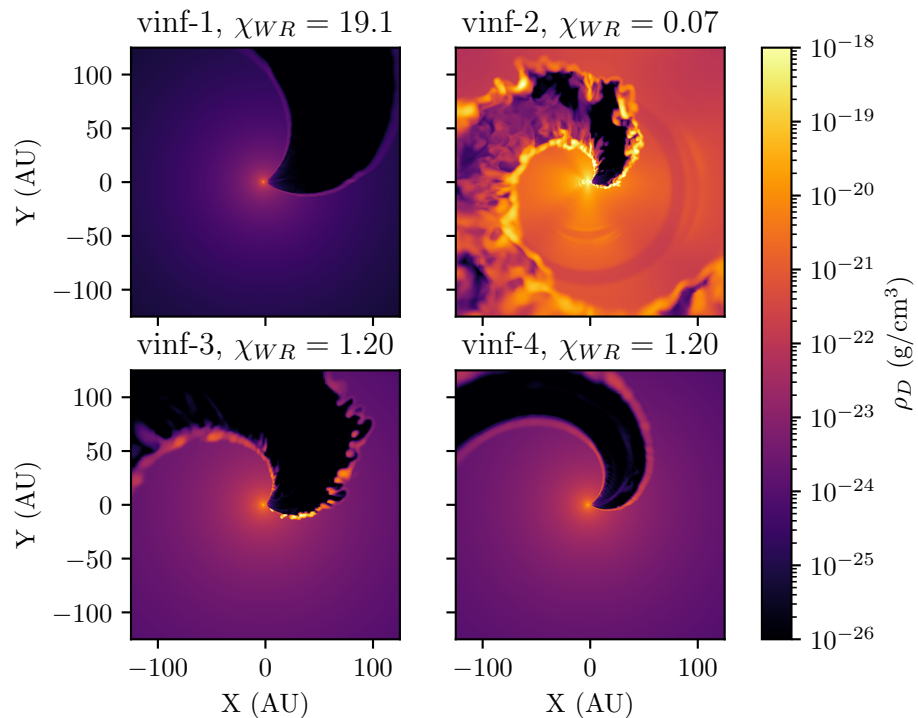


Figure 4.14: Comparison of dust density in v^∞ variation simulations, simulations with either a high OB wind velocity or low WC wind velocity produce large quantities of dust. Simulation **vinf-1**, which has a high velocity WC wind, does not produce any appreciable dust within the WCR. **vinf-1** and **vinf-4** have a smoother WCR with less instabilities as both winds have identical terminal speeds, resulting in no velocity shear.

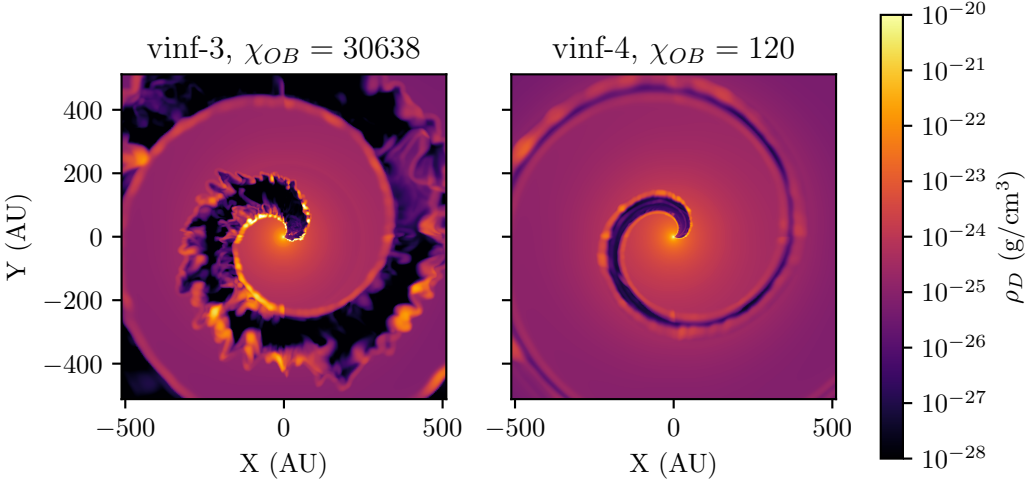


Figure 4.15: Comparison of dust density in simulations with modified OB wind terminal velocities. The simulations are fully advected with $\phi = 3.0$, dust formation and instabilities are far more pronounced in **vinf-3**, which has an OB wind velocity a factor of 4 larger than **vinf-4**.

dust than simulations with more imbalanced winds (figure 4.13). However, this dependence is different to the mass loss rate simulation subset, and the stratification is less apparent.

By directly comparing two prolific dust producing models with $\eta = 0.04$, **vinf-3** and **mdot-3**, we can see that both WCRs are dominated by instabilities. **vinf-3** in particular is more thoroughly mixed (figure 4.16). In particular, it has a much larger trailing edge that produces large quantities of dust (figures 4.17). These simulations produce approximately the same amount of dust, with **vinf-3** also consistently producing dust in the trailing edge of the WCR. From these results it is clear that the dust production rate is increased if there is a highly imbalanced wind velocity, with a slow WC and fast OB wind, as this leads to a post-shock environment governed by thin-shell and Kelvin-Helmholtz instabilities.

4.4.3 Separation variation

There is a clear correlation between separation distance and dust formation rate, with dust production drastically increasing as orbital separation is decreased (figure 4.18). This influence on the dust formation rate is non-linear, with a doubling of the separation distance increasing the dust production rate by approximately one order of magnitude. Variation of the dust

4. A PARAMETER SPACE EXPLORATION OF DUST FORMATION

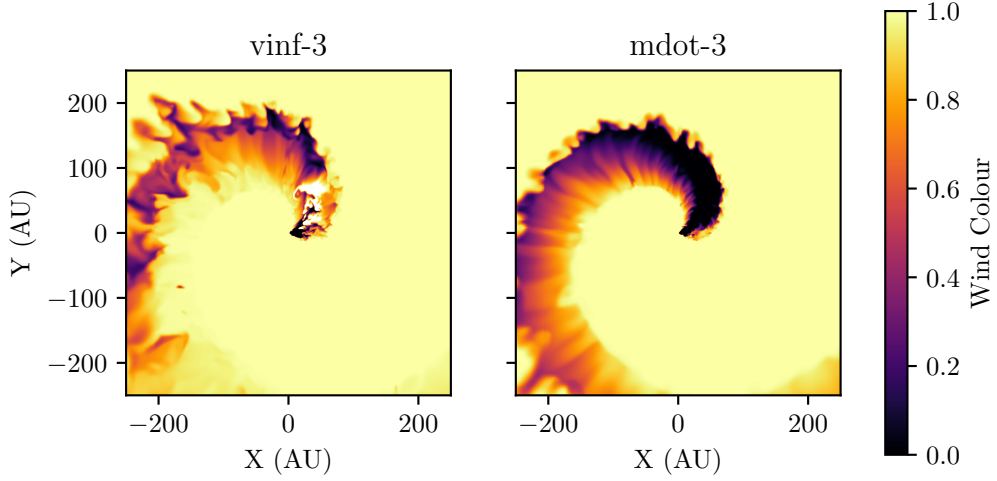


Figure 4.16: Comparison of wind colour in simulations `vinf-3` and `mdot-3`. The WR wind has a colour of 1.0 while the OB wind has a colour of 0.0. Wind mixing is significantly more pronounced, with a pronounced post-shock WR wind that appears to be strongly influenced by Kelvin-Helmholtz instabilities, due to the increased wind velocity imbalance and lower degree of cooling.

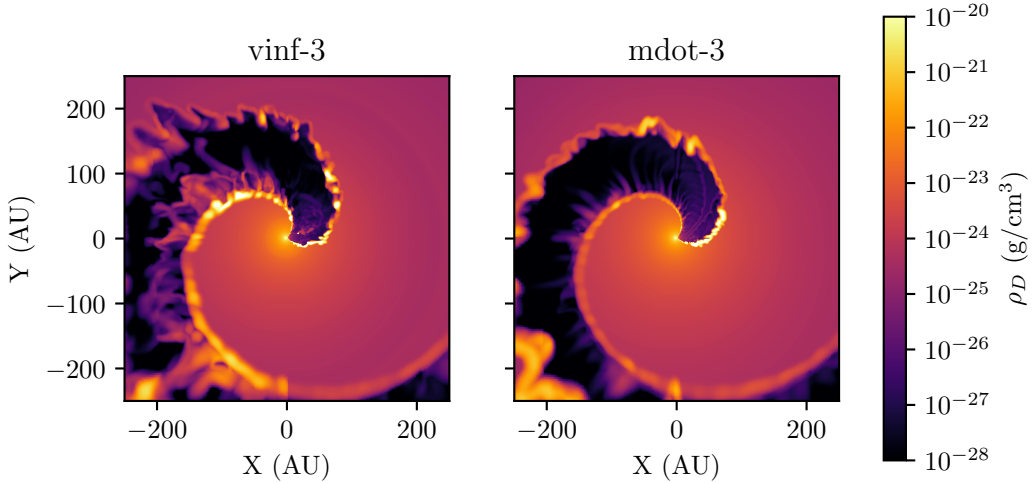


Figure 4.17: Comparison of dust density in simulations with a strong secondary wind, `vinf-3` and `mdot-3`. Dust in `vinf-3` is produced to a much higher degree in the trailing edge of the wind, and increased mixing of the wind due to Kelvin-Helmholtz instabilities has led to dust forming throughout the WCR, rather than near the apex of the WCR.

4.5 Conclusions

Model	η	χ_{WR}	χ_{OB}	$\dot{M}_{\text{D,avg}}$	$\dot{M}_{\text{D,max}}$
				$M_{\odot} \text{ yr}^{-1}$	$M_{\odot} \text{ yr}^{-1}$
Baseline	0.02	1.20	1915	5.38×10^{-10}	9.06×10^{-7}
vinf-1	0.01	19.1	1915	8.88×10^{-13}	7.11×10^{-7}
vinf-2	0.04	0.07	1915	1.17×10^{-7}	1.17×10^{-6}
vinf-3	0.04	1.20	30638	6.30×10^{-11}	1.17×10^{-6}
vinf-4	0.01	1.20	120	1.94×10^{-8}	7.11×10^{-7}

Table 4.10: Rates of dust production for terminal velocity simulation set.

Model	η	χ_{WR}	χ_{OB}	$\dot{M}_{\text{D,avg}}$	$\dot{M}_{\text{D,max}}$
				$M_{\odot} \text{ yr}^{-1}$	$M_{\odot} \text{ yr}^{-1}$
dsep-4AU	0.02	1.20	1915	5.38×10^{-10}	9.06×10^{-7}
dsep-8AU	0.01	2.39	3830	4.39×10^{-11}	9.06×10^{-7}
dsep-16AU	0.04	4.79	7659	1.77×10^{-12}	9.06×10^{-7}
dsep-32AU	0.04	9.57	15319	8.83×10^{-14}	9.06×10^{-7}
dsep-64AU	0.01	19.1	30638	2.41×10^{-14}	9.06×10^{-7}

Table 4.11: Rates of dust production for separation distance set.

production rate also appears to increase as separation distance is reduced, leading to instances where a simulation may temporarily produce more dust than a simulation with a tighter orbit, such as the case with dsep-4AU and dsep-8AU at $\phi = 0.6$ to $\phi = 0.65$. As we have previously discussed, instabilities drive slightly intermittent, but highly efficient dust formation, which would explain these fluctuations (figure 4.19).

This matches observations of episodic dust forming systems, where infrared emission due to dust is maximised at or shortly after periastron passage. This also lends further evidence that dust formation rates are not influenced solely by the momentum ratio, as this is kept constant, and instead is strongly influenced by the wind density at collision and post-shock cooling.

4.5 Conclusions

The simulations in this chapter were conducted over a fairly limited parameter space for mass loss rate and wind terminal velocity. Despite this, dust production varied by up to 6 orders of

4. A PARAMETER SPACE EXPLORATION OF DUST FORMATION

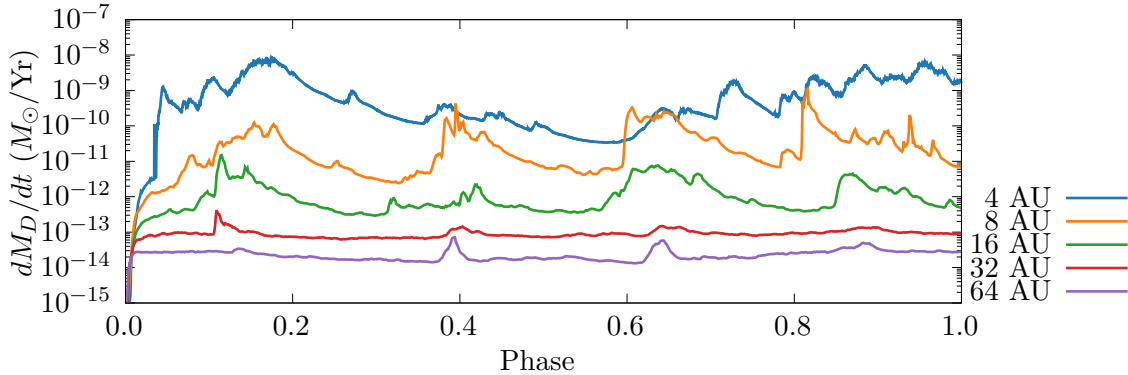


Figure 4.18: A comparison of dust formation rates versus orbital phase for a set of simulations that vary separation distance, d_{sep} . A clear inverse relationship between separation distance and dust production rate exists, most likely due to the stellar winds becoming more diffuse further from their origin stars, leading to weaker shocks and a WCR that behaves more adiabatically.

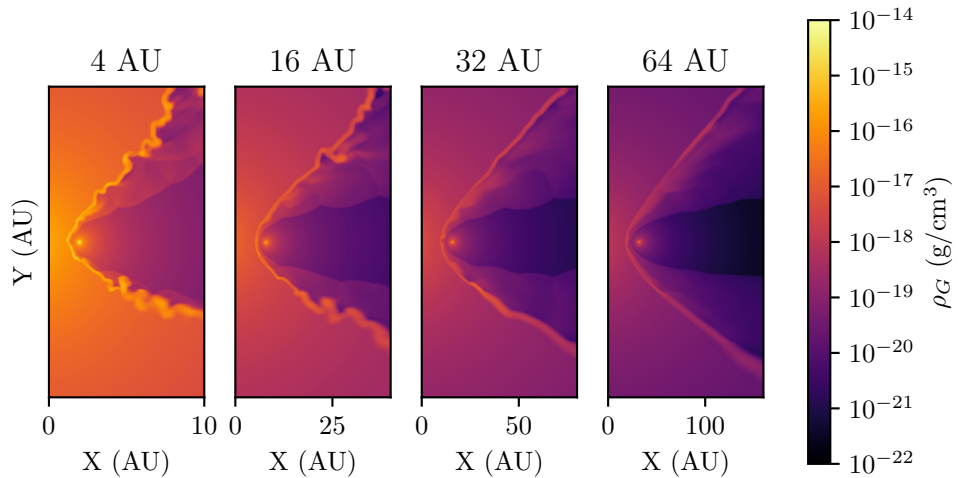


Figure 4.19: A comparison of the structures of simulations varying d_{sep} , the scale of each plot has been changed to allow for a similar feature size, as can be seen simulations with a closer separation distance have collision regions whose structure is more strongly influenced by instabilities, particularly thin-shell instabilities brought on by radiative behaviour within the WCR.

magnitude. Dust formation was found to be extremely sensitive to the wind properties of both stars, which imposes a limited range of wind parameters for dust to form efficiently. This would explain why these dust forming systems are comparatively rare, compared to the total number of systems with binary massive stars and interacting winds, and also why periodic dust forming systems have eccentric orbits. The baseline system, WR98a, has a significantly lower mass loss rate than other well-characterised WCd systems, such as WR140 and WR104. The WC star in WR 140 has a mass loss rate an order of magnitude larger than WR98a, for instance. Future research in this topic will cover these systems, to explore how closely they match observations.

4.5.1 Wind mixing within the WCR

While interaction between hydrogen and dust grains is not simulated by the dust model, Le Teuff (2002) notes that hydrogen could be a potential catalyst for amorphous carbon grain formation. Figure 4.20 shows that the wind is far more effectively mixed by instabilities if it is sufficiently radiative. An improved dust model which can calculate grain yields from chemical reactions could be used to investigate this further. Conveniently, implementation of a chemical model into Athena++ through passive scalars is a future feature in the projects roadmap. Additionally, a multi-fluid model could be used to model the dynamics of grains, as larger grains are significantly more massive than the surrounding medium, and hence have more inertia, this means they may not be necessarily co-moving in a turbulent wind environment. It should also be noted that dust formation around single WC stars has been observed, suggesting that nascent grains are formed within the WC wind, and carried into the WCR as implied by this dust model.

4.6 Summary

A parameter space exploration of Colliding Wind Binary systems undergoing dust formation has proven to yield fascinating insights into how dust forms within the WCR. Dust production within these systems is poorly understood, and with direct observations of the WCR rendered difficult by the extreme conditions of these systems, it falls on numerical simulation to elucidate the post-shock conditions. Most interesting of all is how sensitive to changing wind conditions this dust production is. This parameter space exploration, whilst quite conservative, resulted in a change in dust formation rates of up to 6 orders of magnitude. In all simulations, the bulk of dust formation was found to occur within high-density pockets formed through thin-shell

4. A PARAMETER SPACE EXPLORATION OF DUST FORMATION

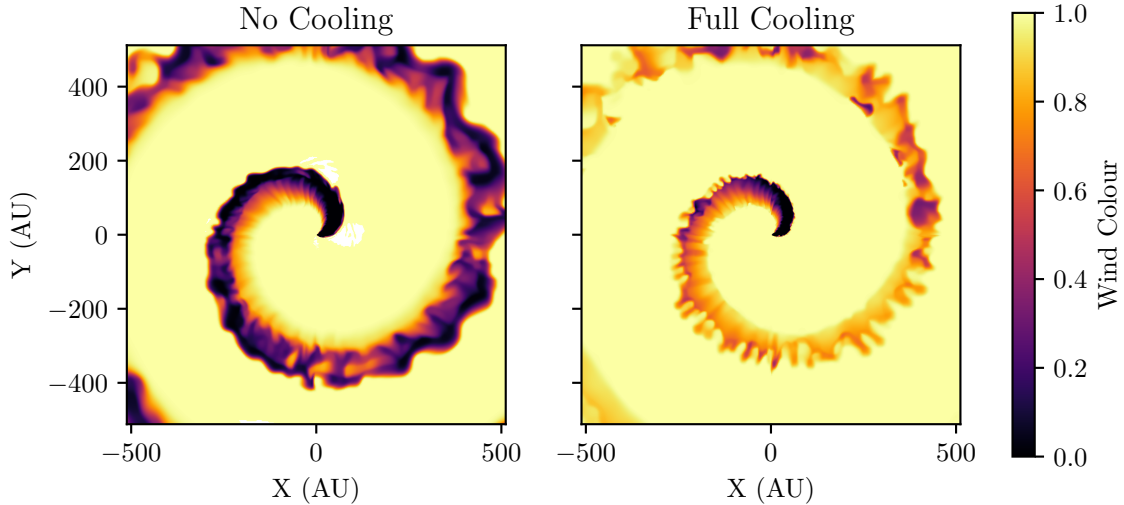


Figure 4.20: Wind “colour” for `nocool` and `fullcool` models. The WCR is more thoroughly mixed if the simulation is allowed to cool.

or Kelvin-Helmholtz instabilities, suggesting that strong cooling and a fast secondary wind are both important factors for dust production. For high levels of dust formation, an ideal system should have a slow, dense primary wind and a fast, dense secondary wind, with a close orbit. A combination of these properties ensures the formation of dense pockets of cool post-shock gas ideal for dust formation.

There is significant potential for additional research in this field. Parameter mixing was not performed, due to the simulation time required for producing many more simulations, but performing examples on more extreme systems, such as those with a LBV primary star or a WR+WR system is a potential avenue of research. Future work could introduce additional dust formation and destruction mechanisms, such as grain-grain collision or photodissociation. Modelling effects such as radiative line driving or use of a multi-fluid model could also prove fruitful. Another interesting avenue of research is the simulation of eccentric, periodic dust forming systems; simulating either an entire or a partial orbit of a system such as WR140 would be a logical next step for this project.

4.7 Acknowledgements

This work was undertaken on ARC4, part of the High Performance Computing facilities at the University of Leeds, UK.

4. A PARAMETER SPACE EXPLORATION OF DUST FORMATION

CHAPTER 5

Hydrodynamical Simulation of WR140

5. HYDRODYNAMICAL SIMULATION OF WR140

Hydrodynamical Simulations of the Periodic Dust Producing System WR140

Abstract

5.1 Introduction

Wolf-Rayet (WR) stars are evolved massive stars that consist of a hydrogen-depleted envelope and a highly radiative core, these stars are so luminous that the total emission from their cores is greater than the Eddington Limit, causing the envelope to be removed from the star in the form of a fast, dense stellar wind. Whilst these stars have wind velocities comparative to their less evolved and massive OB counterparts ($\sim 10^3 \text{ km s}^{-1}$) the mass-loss rate of these systems is many orders of magnitude larger ($\sim 10^{-5} M_\odot \text{ yr}^{-1}$).

As a majority of massive stars form in binary pairs, this can result in the fast, dense stellar wind of the WR component of the binary pair colliding with a significantly weaker stellar wind from its OB partner. This phenomena is referred to as a Colliding Wind Binary system if said phenomena plays an important role in the dynamics of the system. Observations of some of these systems have detected infrared excesses within the Wind Collision Region (WCR) which correspond with the emission from amorphous carbon dust grains. This is interesting as dust would be readily destroyed by evaporation via UV photons in the general medium, as well as the high gas temperature in the region. Instead it is believed that dust grows within the post-shock region, which rapidly cools due to the extremely high post-shock gas density. This high density region can also shield the nascent dust grains from the bulk of the photon flux from the binary stars, resulting in an ideal region for dust formation. Furthermore, this is only observed in systems where the primary star in the binary pair is a highly evolved WC9 star, this adds further complexity to the dust production problem as hydrogen depletion renders many formulation mechanisms dependent on hydrogen seeding impossible, reducing the potential yield of dust (Crowther, 2003; Williams, 2008).

Dust forming CWB systems¹ can produce upwards of $10^{-8} M_\odot \text{ yr}^{-1}$ of amorphous carbon

¹Referred to as WCd systems

dust, primarily in small grains $\sim 100 \text{ \AA}$ in radius. This can have a significant impact on the local interstellar environment in the same manner that a dust producing Asymptotic Giant Branch star can impact its surroundings. CWBd systems can be further subdivided into two types of system based on their dust emission based on their dust emission rates over time, persistently forming systems and episodically forming systems¹. Based on the observations of various WCd and WCde systems there is a strong correlation between orbital eccentricity and dust production periodicity - dust forms readily at or after periastron pass, with dust production being reduced by multiple orders of magnitude at apastron (Williams & van der Hucht, 2015).

Whilst observational data of CWBd systems does exist, and dust formation can be readily observed, the distances from Earth to these systems, combined with the high levels of extinction due to the surrounding stellar wind result in it difficult to observe the dynamics of dust formation within the WCR. Instead numerical simulation of dust growth can be performed in order to discern how dust evolves in the system, this can then be compared to observations using radiative transfer modelling of the resultant numerical grids.

5.2 Methodology

The periodic dust forming system WR140 was simulated using a fork of the Athena++ hydrodynamical code (Stone et al., 2020), a series of modifications were implemented to simulate binary system orbits, stellar wind outflows and dust evolution.

5.2.1 Hydrodynamics

3D simulations in a Cartesian coordinate system were conducted using the Athena++ hydrodynamical code, a modular and modern fluid dynamics code. The code solves a Riemann problem at each cell interface to determine the time-averaged values at the zone interfaces, and then solves the equations of hydrodynamics:

¹WCd

5. HYDRODYNAMICAL SIMULATION OF WR140

$$\frac{\partial \rho}{\partial t} + \nabla \cdot (\rho \mathbf{u}) = 0, \quad (5.1a)$$

$$\frac{\partial \rho \mathbf{u}}{\partial t} + \nabla \cdot (\rho \mathbf{u} \mathbf{u} + P) = 0, \quad (5.1b)$$

$$\frac{\partial \rho \varepsilon}{\partial t} + \nabla \cdot [\mathbf{u} (\rho \varepsilon + P)] = \dot{E}_{cool}, \quad (5.1c)$$

where ε is the total specific energy ($\varepsilon = \mathbf{u}^2/2 + e/\rho$, ρ) is the mass density, e is the internal energy density, P is the gas pressure and \mathbf{u} is the gas velocity. In order to simulate radiative losses, the parameter \dot{E}_{cool} is included, which is the energy loss rate per unit volume from the fluid due to gas and dust cooling. Spatial reconstruction using a piecewise linear method was performed, while the time-integration scheme is a third-order accurate, three-stage strong stability preserving Runge-Kutta¹ method (Gottlieb et al., 2009).

Several passive scalars are utilised to model wind mixing and dust evolution, the scalar values are transported by the fluid, for a given scalar species i , Athena++ transports the scalar through the following equation:

$$\rho \frac{dC_i}{dt} = \frac{\partial}{\partial t} (\rho C_i) + \nabla \cdot (C_i \rho \mathbf{u}) = -\nabla \cdot \mathbf{Q}_i, \quad (5.2)$$

where $\mathbf{Q}_i = -\nu_{ps} \rho \nabla C_i$ is the diffusive flux density and ν is the passive scalar diffusion coefficient (Stone et al., 2020).

Stellar winds are simulated by modifying the conserved variables in a small region around each of the stars. Winds flow from this “remap” region at the stars wind terminal velocity, v^∞ . Remap zone parameters are calculated with the formulae

$$\rho_r = \frac{\dot{M}}{4\pi r^2 v_\infty}, \quad (5.3a)$$

$$P_r = \frac{\rho_r}{\mu m_H} k_B T_w, \quad (5.3b)$$

$$E_r = \frac{P_r}{\gamma - 1} + \frac{1}{2} \rho_r v_r^2, \quad (5.3c)$$

$$p_r = \rho_r v_r, \quad (5.3d)$$

¹SSPRK (3,3)

where v_R is the wind velocity as it flows radially from the center of the “remap zone” and r is the distance from the current cell to the centre of the remap zone. This method produces radially out-flowing winds from the “star” with an expected density and velocity. This method is stable against numerical instability, while allowing for precisely controlled winds.

Line driving and stellar force effects are not simulated, which can result in divergence with the correct wind velocity as stars approach periastron passage. Additioanlly, influence from either gravitational self-interaction and interaction with the stars gravity wells is not simulated, with the stellar winds assumed to be travelling far in excess of the system escape velocity.

Adaptive Mesh Refinement was considered for this simulation, however a known issue with the Athena++ code prevented this from being possible. Passive scalars incorporated into the simulation were found to not be conserved along the interfaces between mesh blocks undergoing refinement, this meant that the simulation would behave non-physically (This bug is recorded as issue #365 on the Athena++ Github repository¹). A ring of refined cells across the orbital path was considered, but the performance improvements of this method were found to be negligible and not worth pursuing, as the block based refinement method of Athena++ would result in much redundant refinement. Instead, a static mesh is used, where a region around the stars at $\phi = 0.95$ is refined to the maximum level, with a gradual de-refinement away from this refinement region.

5.2.2 Dust model and cooling

The dust model in this paper simulates dust growth and destruction through collisions between carbon atoms and dust grains. These grains are simulated in the form of advected scalars in each cell in the numerical grid which propagate with the same hydrodynamical rules as the stellar wind; as such dust can be described as co-moving with the interstellar wind. The two scalars in use are z , the dust-to-gas mass ratio within the cell, and a , the average grain radius. Using these parameters in addition to the local wind parameters, the dust can be adequately described and evolved with time.

A number of assumptions are made in this dust model, for instance, the dust grains are assumed to be spherical, with a uniform density of 3 g cm^{-3} . Dust grains are assumed to have a single size in a region, as well as a constant number density, as such, this model does not

¹<https://github.com/PrincetonUniversity/athena/issues/365>

5. HYDRODYNAMICAL SIMULATION OF WR140

simulate grain agglomeration and fracturing. Additional mechanisms for dust formation and destruction could also be implemented such as grain-grain agglomeration and photoevaporation. Furthermore, a multi-fluid model with drag force coupling could also be implemented, however this is beyond the scope of this paper.

Dust is grown through grain accretion using formulae described by (Spitzer Jr., 2008). Dust grains grow via collisions with the surrounding gas, as gas accretes onto these grains the associated density is subtracted from the gas density. The growth rate is such that:

$$\frac{da}{dt} = \frac{\xi_a \rho_{Gr} w_a}{4\rho}, \quad (5.4a)$$

$$\frac{\rho_D}{dt} = 4\pi a^2 \rho n_D \frac{da}{dt}, \quad (5.4b)$$

where w_a is the Maxwell-Boltzmann distribution RMS velocity, ξ_a is the grain sticking efficiency, ρ_{Gr} is the grain bulk density, ρ is the gas density, a is the dust grain radius, and n_D is the grain number density. For these simulations, the grain sticking factor has been set to 10%, while for low temperature collisions a sticking factor of 100% can be proven, grain sticking in a more energetic, hot regime could significantly reduce the probability of sticking.

Dust destruction is calculated via gas-grain sputtering using the Draine & Salpeter prescription - a dust grain has a lifespan, τ , which is dependent on the grain radius, as the grain loses radius proportional to its loss in mass; assuming a spherical grain, the rate of change in mass and radius can be calculated through the following equation:

$$\tau_D = 1 \text{ Myr} \times \frac{a}{n_g}, \quad (5.5a)$$

$$\frac{da}{dt} = -\frac{a}{\tau_D}, \quad (5.5b)$$

$$\frac{dm}{dt} = -1.33 \times 10^{-13} a^2 n_g n_d \rho_{Gr}, \quad (5.5c)$$

5.2.3 Simulated systems

WR 98a is a typical dusty CWB system that was primarily chosen for simulation as it is one of the only CWB systems whose dust dynamics have been simulated in an academic paper (Hendrix et al., 2016). The model utilised in Hendrix et al. was a dual-fluid model with an

5.2 Methodology

Parameter		Citation
P (d)	2895	Thomas et al. (2021)
e	0.8993	Thomas et al. (2021)
$d_{\text{sep,peri}}$ (AU)	1.53	Thomas et al. (2021)
η	0.031	
χ_{\min}	2.69	

Table 5.1: Parameters for the WR140 system

Parameter	WC9	O4-5	Citation
M (M_{\odot})	10.31	29.27	Thomas et al. (2021)
\dot{M} ($M_{\odot} \text{ yr}^{-1}$)	5.6×10^{-5}	1.6×10^{-6}	Williams, van der Hucht, Pollock et al. (1990)
v^{∞} (km s $^{-1}$)	2860	3200	Williams, van der Hucht, Pollock et al. (1990)
X(H)	0.000	0.705	
X(He)	0.546	0.275	
X(C)	0.400	0.003	

Table 5.2: Parameters for the WR140 system

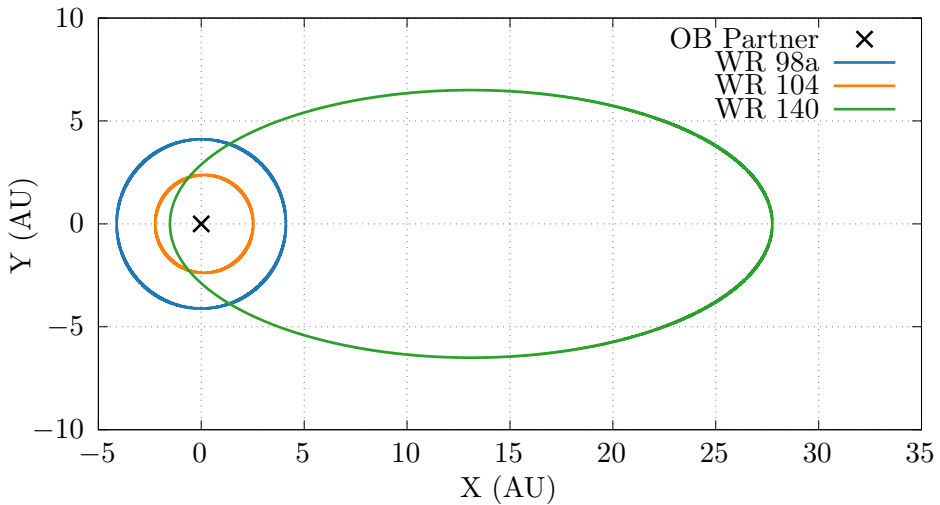


Figure 5.1: Orbital paths for each system, a co-ordinate transform is applied such that the orbitally dominant OB partner is always at co-ordinate (0,0). WR 140 has a significantly more eccentric orbit, as well as a much longer orbital period.

5. HYDRODYNAMICAL SIMULATION OF WR140

Epstein drag function in order to detail how dust flows through the system itself. As such, this model does not simulate dust accretion or cooling, and only deposits dust grains with a single set grain radius and a fixed dust production rate of $\phi = 0.0763$. However, this still provides a useful point of comparison to evaluate this paper's dust model against an established model with concrete data. Furthermore, a simplified version of WR 98a was used to test the dust model and was used as a basis to explore the parameter space of dusty CWB systems by varying wind parameters and orbital separation. The parameters detailed in table 2.4 are adopted from Hendrix et al., similarly to this paper a perfectly circular orbit is assumed.

WR 104 is an archetypical dust forming binary system that is extensively observed, with multiple papers on the dynamics and formation of dust in the system.

WR 104 represents the high end of dust formation in CWB systems, with a high dust formation rate in the order of $3 \times 10^{-7} M_{\odot} \text{yr}^{-1}$, the close separation of the binary system combined with the high mass loss rate results in a much lower value of χ for the WR wind, suggesting very strong cooling in the post-shock wind collision region. As such this system is more difficult to simulate, as a higher resolution and lower Courant number are required in order to reliably simulate the post-shock cooling effect. The orbital and wind parameters of this system were derived from Soulain et al., 2018 and Harries et al., 2004.

WR 140 was simulated for this experiment as it represents an archetypical episodic CWB system, whose infrared dust emission peaks around periastron passage. WR 140 deviates from WR 98a and WR 104 by being extremely eccentric, which significantly effects the cooling parameter as the orbit progresses (figure 5.2). Additionally, the minimum value for χ is significantly larger than the other systems, and hence cooling would be less dominant on the dynamics of the WCR, even at periapsis. Though these simulations do not calculate wind acceleration due to radiative line driving, both stellar winds are expected to be accelerated close to their terminal wind velocities (Lamers & Cassinelli, 1999). However, this discrepancy should be noted when considering the results of this paper. The orbital and wind parameters of this system were derived from work by Monnier et al., 2011, Usov, 1991, as well as Thomas et al., 2021.

5.2.4 Radiative transfer modelling

5.3 Results

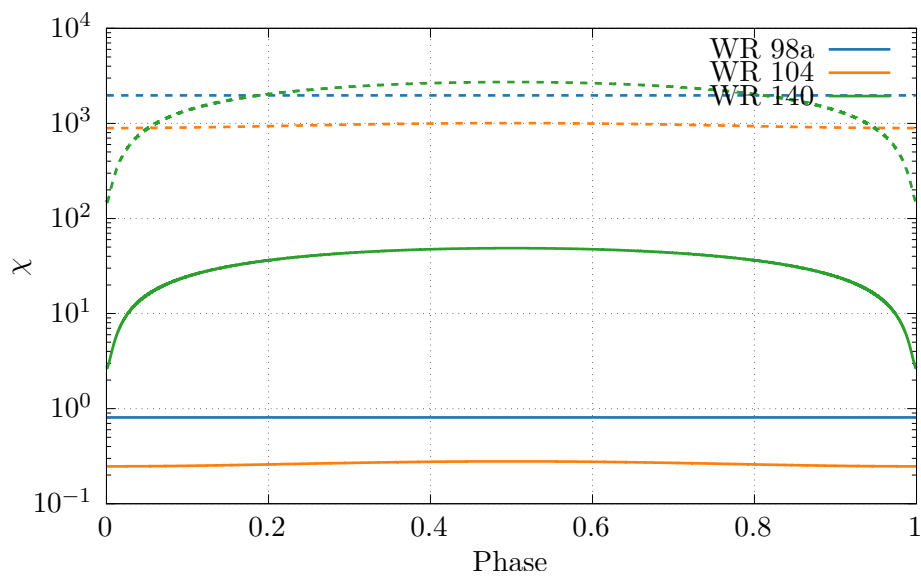


Figure 5.2: Change in WR cooling parameter χ over a single orbit, solid lines represent the primary WC star, while dashed lines represent their OB partners. The dynamics of the WCR for WR 98a and WR 104 is dominated by cooling throughout their entire orbits, while WR 140 is adiabatic for most of its orbit. Additionally OB stars have significantly higher cooling parameters, and thus their flows behave adiabatically.

5. HYDRODYNAMICAL SIMULATION OF WR140

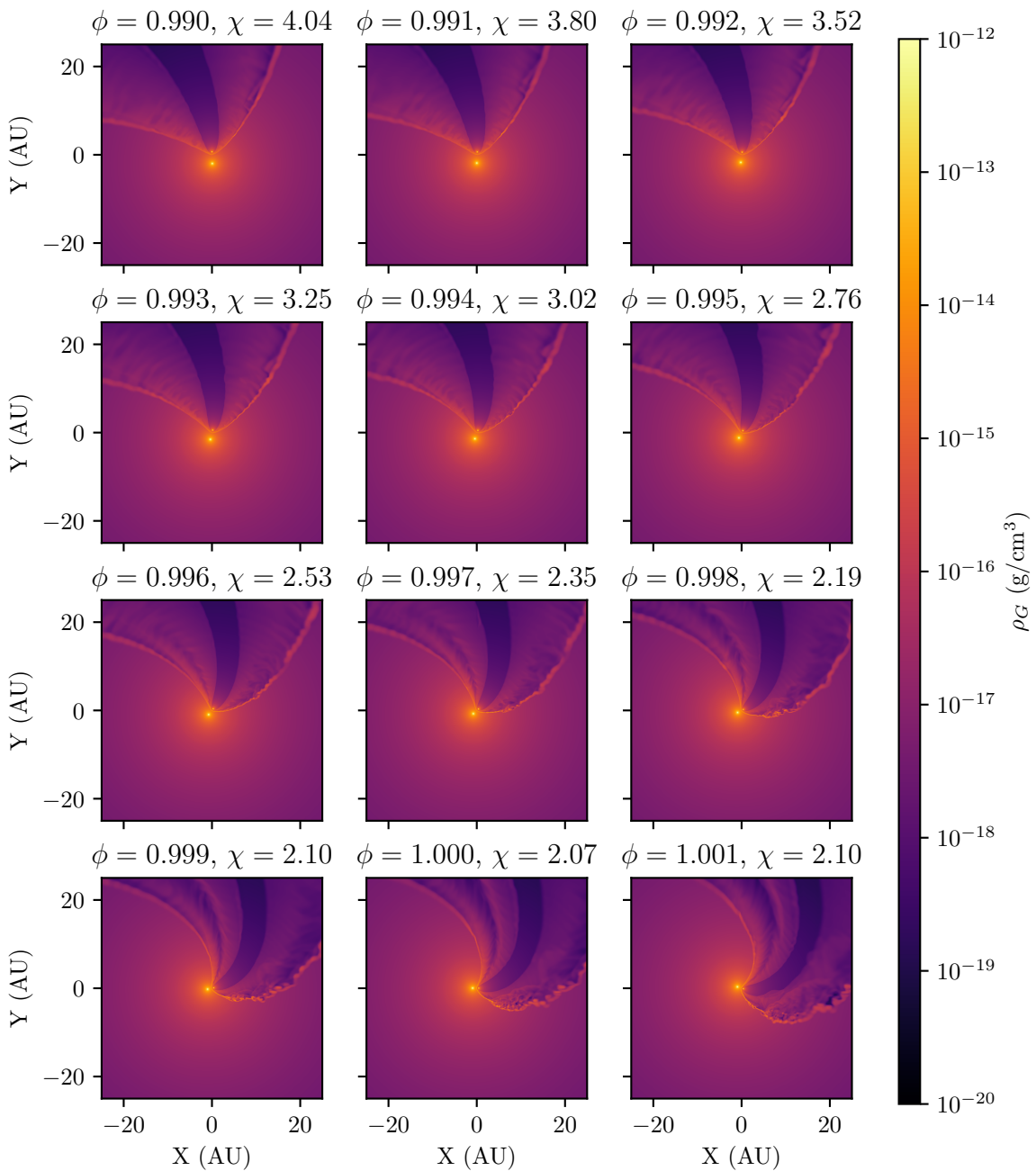


Figure 5.3: Density plot of WR140 periastron passage. Approaching periastron the system becomes increasingly driven by instabilities, with a clear separation between primary and secondary wind collision regions on the trailing edge.

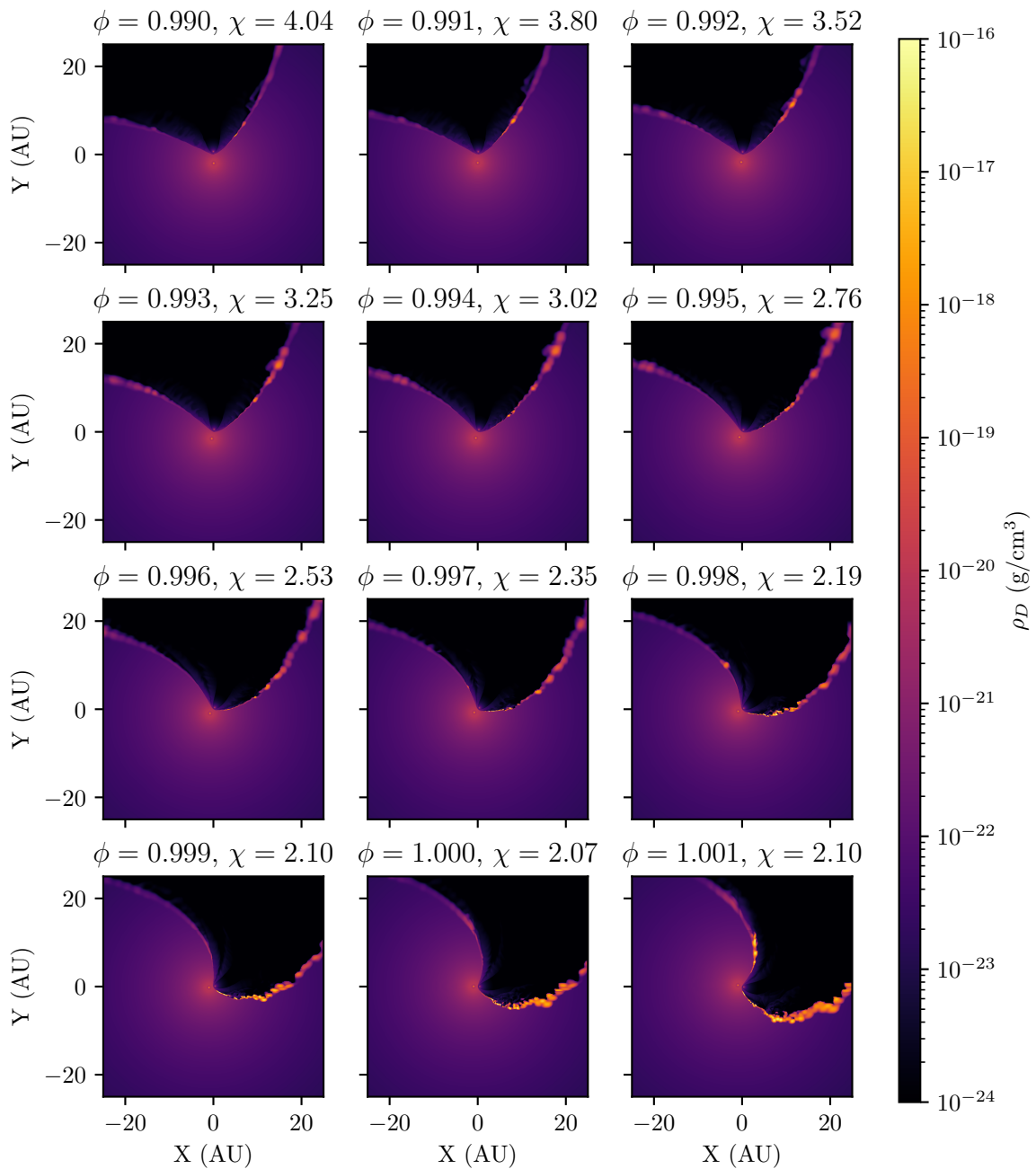


Figure 5.4: Dust density plot of WR140 periastron passage. As the system approaches periastron the amount of dust within the WCR drastically increases, while tapering off at a slow rate.

5. HYDRODYNAMICAL SIMULATION OF WR140

CHAPTER 6

An Exploration on the Influence of Wind Velocity of
Dust formation in WCd Systems

6. INFLUENCE OF WIND VELOCITY ON DUST FORMATION

6.1 Introduction

6.2 Methodology

6.3 Model Parameters

6.4 Results

6.4 Results

Model	v_{WR}^{∞} cm s $^{-1}$	v_{OB}^{∞} cm s $^{-1}$	η	χ_{WR}	χ_{OB}
sim-1-wr	2.00×10^8	2.00×10^8	0.010	19.149	1915
sim-2-wr	1.36×10^8	2.00×10^8	0.015	4.060	1915
sim-3-wr	1.03×10^8	2.00×10^8	0.019	1.332	1915
sim-4-wr	8.26×10^7	2.00×10^8	0.024	0.557	1915
sim-5-wr	6.91×10^7	2.00×10^8	0.029	0.273	1915
sim-6-wr	5.94×10^7	2.00×10^8	0.034	0.149	1915
sim-7-wr	5.21×10^7	2.00×10^8	0.038	0.088	1915
sim-8-wr	4.63×10^7	2.00×10^8	0.043	0.055	1915
sim-9-wr	4.18×10^7	2.00×10^8	0.048	0.036	1915
sim-10-wr	3.80×10^7	2.00×10^8	0.053	0.025	1915
sim-11-wr	3.49×10^7	2.00×10^8	0.057	0.018	1915
sim-12-wr	3.22×10^7	2.00×10^8	0.062	0.013	1915
sim-13-wr	2.99×10^7	2.00×10^8	0.067	0.010	1915
sim-14-wr	2.79×10^7	2.00×10^8	0.072	0.007	1915
sim-15-wr	2.62×10^7	2.00×10^8	0.076	0.006	1915
sim-16-wr	2.47×10^7	2.00×10^8	0.081	0.004	1915
sim-17-wr	2.33×10^7	2.00×10^8	0.086	0.004	1915
sim-18-wr	2.21×10^7	2.00×10^8	0.091	0.003	1915
sim-19-wr	2.10×10^7	2.00×10^8	0.095	0.002	1915
sim-20-wr	2.00×10^7	2.00×10^8	0.100	0.002	1915

Table 6.1: WR parameters

6. INFLUENCE OF WIND VELOCITY ON DUST FORMATION

Model	v_{WR}^{∞} cm s $^{-1}$	v_{OB}^{∞} cm s $^{-1}$	η	χ_{WR}	χ_{OB}
sim-1-ob	1.00×10^8	1.00×10^8	0.010	1.197	120
sim-2-ob	1.00×10^8	1.47×10^8	0.015	1.197	564
sim-3-ob	1.00×10^8	1.95×10^8	0.019	1.197	1721
sim-4-ob	1.00×10^8	2.42×10^8	0.024	1.197	4112
sim-5-ob	1.00×10^8	2.89×10^8	0.029	1.197	8403
sim-6-ob	1.00×10^8	3.37×10^8	0.034	1.197	15407
sim-7-ob	1.00×10^8	3.84×10^8	0.038	1.197	26079
sim-8-ob	1.00×10^8	4.32×10^8	0.043	1.197	41520
sim-9-ob	1.00×10^8	4.79×10^8	0.048	1.197	62975
sim-10-ob	1.00×10^8	5.26×10^8	0.053	1.197	91833
sim-11-ob	1.00×10^8	5.74×10^8	0.057	1.197	129630
sim-12-ob	1.00×10^8	6.21×10^8	0.062	1.197	178045
sim-13-ob	1.00×10^8	6.68×10^8	0.067	1.197	238900
sim-14-ob	1.00×10^8	7.16×10^8	0.072	1.197	314164
sim-15-ob	1.00×10^8	7.63×10^8	0.076	1.197	405950
sim-16-ob	1.00×10^8	8.11×10^8	0.081	1.197	516516
sim-17-ob	1.00×10^8	8.58×10^8	0.086	1.197	648263
sim-18-ob	1.00×10^8	9.05×10^8	0.091	1.197	803739
sim-19-ob	1.00×10^8	9.53×10^8	0.095	1.197	985633
sim-20-ob	1.00×10^8	1.00×10^9	0.100	1.197	1196783

Table 6.2: OB parameters

CHAPTER 7

Final Notes and Conclusions

7. FINAL NOTES AND CONCLUSIONS

7.1 Conclusions

7.1.1 Causes of dust formation in WCB systems

7.1.2 The role of eccentricity in dust formation

7.2 Future Study

7.2.1 More complex models

7.2.2 Further simulations of observed systems

7.2.3 Radiative transfer

7.2.4 WR+WR systems

7.2.5 Next generation telescopes

7.3 Other Observations

7.3.1 *Doctorate Strangelove or: How I Learned to Stop Worrying and Love Numerics*

7.3.2 Join the physics department, see the world

7.3.3 Paul Erdős was probably onto something

7.3.4 Carinae Strain: PhD research in a time of pandemic

7.3.5 WR 104 as a local GRB candidate

7.3.6 Research software acknowledgements

GNU Parallel Tange (2021)

Visit Childs et al. (2012)

NumPy Harris et al. (2020)

7.3 Other Observations

Astropy Astropy Collaboration et al. (2013) Astropy Collaboration et al. (2018)

Matplotlib Hunter (2007)

7. FINAL NOTES AND CONCLUSIONS

APPENDIX A

Astrophysical Shocks

A. ASTROPHYSICAL SHOCKS

APPENDIX B

Software Carpentry

B. SOFTWARE CARPENTRY

B.1 Amdahl's Law

B.2 Version Control

BIBLIOGRAPHY

Book Citations

- Carroll, B. W. & Ostlie, D. A. (2014). *An Introduction to Modern Astrophysics* (Second international). Pearson. (Cited on page 4)
OCLC: 868368508.
- Dyson, J. E. (2021). *The physics of the interstellar medium* (Third edition.). CRC Press. (Cited on pages 15, 16).
- Lamers, H. J. & Cassinelli, J. P. (1999). *Introduction to stellar winds*. Cambridge University Press. (Cited on pages 10, 96).
- Oswalt, T. D. & Barstow, M. A. (Eds.). (2013). *Planets, Stars and Stellar Systems*. Springer Netherlands. <https://doi.org/10.1007/978-94-007-5615-1>. (Cited on page 8)
- Ryan, S. G. & Norton, A. J. (2010). *Stellar evolution and nucleosynthesis*. Cambridge University Press. (Cited on page 7)
OCLC: ocn437083016.
- Rybicki, G. B. & Lightman, A. P. (2004). *Radiative processes in astrophysics*. Wiley. (Cited on page 17)
OCLC: 255501661.
- Salaris, M. & Cassisi, S. (2005). *Evolution of Stars and Stellar Populations*. (Cited on page 6).
- Spitzer Jr., L. (2008, November 20). *Physical Processes in the Interstellar Medium*. John Wiley & Sons. (Cited on pages 66, 94).
- Vink, J. S. (Ed.). (2015). *Very Massive Stars in the Local Universe* (Vol. 412). Springer International Publishing. <https://doi.org/10.1007/978-3-319-09596-7>. (Cited on page 7)
- Ward-Thompson, D. & Whitworth, A. P. (2011). *An Introduction to Star Formation*. Cambridge University Press. <https://doi.org/10.1017/CBO9780511974021>. (Cited on pages 5, 7)

BIBLIOGRAPHY

Journal Citations

- Allen, D. A., Swings, J. P. & Harvey, P. M. (1972). Infrared photometry of northern Wolf-Rayet stars. *Astronomy and Astrophysics*, 20, 333–336 (cited on page 56).
- Berger, M. J. & Colella, P. (1989). Local adaptive mesh refinement for shock hydrodynamics. *Journal of Computational Physics*, 82(1), 64–84. [https://doi.org/10.1016/0021-9991\(89\)90035-1](https://doi.org/10.1016/0021-9991(89)90035-1) (cited on page 33)
- Berger, M. J. & Oliger, J. (1984). Adaptive mesh refinement for hyperbolic partial differential equations. *Journal of Computational Physics*, 53(3), 484–512. [https://doi.org/10.1016/0021-9991\(84\)90073-1](https://doi.org/10.1016/0021-9991(84)90073-1) (cited on page 33)
- Callingham, J. R., Tuthill, P. G., Pope, B. J. S., Williams, P. M., Crowther, P. A., Edwards, M., Norris, B. & Kedziora-Chudczer, L. (2019). Anisotropic winds in a Wolf-Rayet binary identify a potential gamma-ray burst progenitor. *Nature Astronomy*, 3(1), 82–87. <https://doi.org/10.1038/s41550-018-0617-7> (cited on page 29)
- Castor, J. I., Abbott, D. C. & Klein, R. I. (1975). Radiation-driven winds in Of stars. *The Astrophysical Journal*, 195, 157. <https://doi.org/10.1086/153315> (cited on page 10)
- Cherepashchuk, A. M. (1976). Detectability of Wolf-Rayet binaries from X-rays. *Soviet Astronomy Letters*, 2, 138 (cited on page 13).
- Colella, P. & Woodward, P. R. (1984). The piecewise parabolic method (PPM) for gas-dynamical simulations. *Journal of computational physics*, 54(1), 174–201 (cited on page 28).
- Crowther, P. A. (2003). Dust Formation around Wolf-Rayet Stars. *Astrophysics and Space Science*, 285(3), 677–685. <https://doi.org/10.1023/A:1026157126395> (cited on pages 22, 90)
- Crowther, P. A. (2007). Physical Properties of Wolf-Rayet Stars. *Annual Review of Astronomy and Astrophysics*, 45(1), 177–219. <https://doi.org/10.1146/annurev.astro.45.051806.110615> (cited on pages 7, 8)
- Draine, B. T. & Salpeter, E. E. (1979). Destruction mechanisms for interstellar dust. *The Astrophysical Journal*, 231, 438–455. <https://doi.org/10.1086/157206> (cited on page 20)
- Draine, B. & Salpeter, E. (1979). Destruction mechanisms for interstellar dust. *The Astrophysical Journal*, 231, 438–455 (cited on page 66).
- Dwek, E. & Werner, M. W. (1981). The Infrared Emission From Supernova Condensates. *The Astrophysical Journal*, 248, 138. <https://doi.org/10.1086/159138> (cited on pages 18, 42, 43, 46, 62, 63)

JOURNAL CITATIONS

- Eichler, D. & Usov, V. (1993). Particle acceleration and nonthermal radio emission in binaries of early-type stars. *The Astrophysical Journal*, *402*, 271–279. <https://doi.org/10.1086/172130> (cited on pages 14, 15, 58)
- Godunov, S. K. (1959). A difference scheme for numerical solution of discontinuous solution of hydrodynamic equations. *Math. Sbornik*, *47*, 271–306 (cited on page 27).
- Gottlieb, S., Ketcheson, D. I. & Shu, C.-W. (2009). High Order Strong Stability Preserving Time Discretizations. *Journal of Scientific Computing*, *38*(3), 251–289. <https://doi.org/10.1007/s10915-008-9239-z> (cited on page 92)
- Grimaldo, E., Reimer, A., Kissmann, R., Niederwanger, F. & Reitberger, K. (2019). Proton Acceleration in Colliding Stellar Wind Binaries. *The Astrophysical Journal*, *871*, 55. <https://doi.org/10.3847/1538-4357/aaf6ee> (cited on page 14)
- Harries, T. J., Monnier, J. D., Symington, N. H. & Kurosawa, R. (2004). Three-dimensional dust radiative-transfer models: The Pinwheel Nebula of WR 104. *Monthly Notices of the Royal Astronomical Society*, *350*(2), 565–574. <https://doi.org/10.1111/j.1365-2966.2004.07668.x> (cited on page 96)
- Hendrix, T., Keppens, R., van Marle, A. J., Camps, P., Baes, M. & Meliani, Z. (2016). Pinwheels in the sky, with dust: 3D modelling of the Wolf-Rayet 98a environment. *Monthly Notices of the Royal Astronomical Society*, *460*(4), 3975–3991. <https://doi.org/10.1093/mnras/stw1289> (cited on pages 51, 53, 54, 65, 75, 94)
- Ishihara, D., Kaneda, H., Onaka, T., Ita, Y., Matsuura, M. & Matsunaga, N. (2011). Galactic distributions of carbon- and oxygen-rich AGB stars revealed by the AKARI mid-infrared all-sky survey. *Astronomy & Astrophysics*, *534*, A79. <https://doi.org/10.1051/0004-6361/201117626> (cited on page 21)
- Le Teuff, Y. H. (2002). A Model of Dust Formation in Clumpy Wolf-Rayet Winds. *260*, 223 (cited on page 85).
- Lucy, L. B. & Solomon, P. M. (1970). Mass Loss by Hot Stars. *The Astrophysical Journal*, *159*, 879. <https://doi.org/10.1086/150365> (cited on pages 10, 11)
- Marchenko, S. V., Moffat, A. F. J. & Crowther, P. A. (2010). Population I Wolf-Rayet Runaway Stars: The Case of WR124 and its Expanding Nebula M1-67. *The Astrophysical Journal*, *724*, L90–L94. <https://doi.org/10.1088/2041-8205/724/1/L90> (cited on page 12)
ADS Bibcode: 2010ApJ...724L..90M
- Medina, E. M., Richardson, N. & Chené, A. (2021). Are all WCd stars binaries? An IGRINS search for companion stars. *53*, 215.07 (cited on page 19).

BIBLIOGRAPHY

- Meyer, C. D., Balsara, D. S. & Aslam, T. D. (2014). A stabilized Runge-Kutta-Legendre method for explicit super-time-stepping of parabolic and mixed equations. *Journal of Computational Physics*, 257, 594–626. <https://doi.org/10.1016/j.jcp.2013.08.021> (cited on page 32)
ADS Bibcode: 2014JCoPh.257..594M
- Monnier, J. D., Tuthill, P. G., Danchi, W. C., Murphy, N. & Harries, T. J. (2007). The Keck Aperture-masking Experiment: Near-Infrared Sizes of Dusty Wolf-Rayet Stars. *The Astrophysical Journal*, 655(2), 1033. <https://doi.org/10.1086/509873> (cited on page 24)
- Monnier, J. D., Zhao, M., Pedretti, E., Millan-Gabet, R., Berger, J.-P., Traub, W., Schloerb, F. P., ten Brummelaar, T., McAlister, H., Ridgway, S., Sturmann, L., Sturmann, J., Turner, N., Baron, F., Kraus, S., Tannirkulam, A. & Williams, P. M. (2011). First Visual Orbit for the Prototypical Colliding-wind Binary WR 140. *The Astrophysical Journal Letters*, 742, L1. <https://doi.org/10.1088/2041-8205/742/1/L1> (cited on page 96)
- Neugent, K. & Massey, P. (2019). The Wolf-Rayet Content of the Galaxies of the Local Group and Beyond. *Galaxies*, 7(3), 74. <https://doi.org/10.3390/galaxies7030074> (cited on page 8)
- Niedzielski, A. & Skorzynski, W. (2002). Kinematical Structure of Wolf-Rayet Winds. I.Terminus Wind Velocity. *Acta Astronomica*, 52, 81–104 (cited on page 21)
ADS Bibcode: 2002AcA....52...81N.
- Pauldrach, A., Puls, J. & Kudritzki, R. P. (1986). Radiation-driven winds of hot luminous stars. Improvements of the theory and first results. *Astronomy and Astrophysics*, Vol. 164, p. 86-100 (1986), 164, 86 (cited on page 10).
- Pittard, J. M. (2009). 3D models of radiatively driven colliding winds in massive O+O star binaries - I. Hydrodynamics. *Monthly Notices of the Royal Astronomical Society*, 396(3), 1743–1763. <https://doi.org/10.1111/j.1365-2966.2009.14857.x> (cited on page 74)
- Pittard, J. M. & Dawson, B. (2018). Colliding stellar winds structure and X-ray emission. *Monthly Notices of the Royal Astronomical Society*, 477(4), 5640–5645. <https://doi.org/10.1093/mnras/sty1025> (cited on page 58)
- Prilutskii, O. F. & Usov, V. V. (1976). X rays from Wolf-Rayet binaries. *Soviet Astronomy*, 20, 2 (cited on page 13).
- Rosslowe, C. K. & Crowther, P. A. (2015). Spatial distribution of Galactic Wolf-Rayet stars and implications for the global population. *Monthly Notices of the Royal Astronomical Society*, 451(3), 2733–2746. <https://doi.org/10.1093/mnras/stv150> (cited on page 13)

JOURNAL CITATIONS

- Society*, 447(3), 2322–2347. <https://doi.org/10.1093/mnras/stu2525> (cited on pages 20, 57)
- Ruuth, S. J. & Spiteri, R. J. (2005). High-Order Strong-Stability-Preserving Runge-Kutta Methods with Downwind-Biased Spatial Discretizations. *SIAM Journal on Numerical Analysis*, 42(3), 974–996 (cited on page 32).
- Salpeter, E. E. (1977). Formation and Destruction of Dust Grains. *Annual Review of Astronomy and Astrophysics*, 15(1), 267–293 (cited on page 20).
- Schure, K. M., Kosenko, D., Kaastra, J. S., Keppens, R. & Vink, J. (2009). A New Radiative Cooling Curve Based on an Up-To-Date Plasma Emission Code. *Astronomy & Astrophysics*, 508(2), 751–757. <https://doi.org/10.1051/0004-6361/200912495> (cited on page 17)
- Spiteri, R. J. & Ruuth, S. J. (2002). A New Class of Optimal High-Order Strong-Stability-Preserving Time Discretization Methods. *SIAM Journal on Numerical Analysis*, 40(2), 469–491. <https://doi.org/10.1137/S0036142901389025> (cited on page 59)
- Stevens, I. R., Blondin, J. M. & Pollock, A. M. T. (1992). Colliding winds from early-type stars in binary systems. *The Astrophysical Journal*, 386, 265–287. <https://doi.org/10.1086/171013> (cited on pages 58, 79)
- Stone, J. M., Tomida, K., White, C. J. & Felker, K. G. (2020). The Athena++ Adaptive Mesh Refinement Framework: Design and Magnetohydrodynamic Solvers. *The Astrophysical Journal Supplement Series*, 249(1), 4. <https://doi.org/10.3847/1538-4365/ab929b> (cited on pages 31, 58, 91, 92)
- Thomas, J. D., Richardson, N. D., Eldridge, J. J., Schaefer, G. H., Monnier, J. D., Sana, H., Moffat, A. F. J., Williams, P., Corcoran, M. F., Stevens, I. R., Weigelt, G., Zainol, F. D., Anugu, N., Le Bouquin, J.-B., ten Brummelaar, T., Campos, F., Couperus, A., Davies, C. L., Ennis, J., ... Zurmühl, U. (2021). The orbit and stellar masses of the archetype colliding-wind binary WR 140. *Monthly Notices of the Royal Astronomical Society*, 504(4), 5221–5230. <https://doi.org/10.1093/mnras/stab1181> (cited on pages 95, 96)
- Toro, E. F., Spruce, M. & Speares, W. (1994). Restoration of the contact surface in the HLL-Riemann solver. *Shock Waves*, 4(1), 25–34. <https://doi.org/10.1007/BF01414629> (cited on pages 28, 32)

BIBLIOGRAPHY

- Townsend, R. H. D. (2009). An Exact Integration Scheme for Radiative Cooling in Hydro-dynamical Simulations. *The Astrophysical Journal Supplement Series*, 181(2), 391–397. <https://doi.org/10.1088/0067-0049/181/2/391> (cited on pages 38, 49, 51)
- Usov, V. V. (1991). Stellar wind collision and dust formation in long-period, heavily interacting Wolf-Rayet binaries. *Monthly Notices of the Royal Astronomical Society*, 252(1), 49–52. <https://doi.org/10.1093/mnras/252.1.49> (cited on pages 15, 56, 74, 96)
- van Leer, B. (1979). Towards the ultimate conservative difference scheme. V. A second-order sequel to Godunov's method. *Journal of Computational Physics*, 32(1), 101–136. [https://doi.org/10.1016/0021-9991\(79\)90145-1](https://doi.org/10.1016/0021-9991(79)90145-1) (cited on pages 28, 32)
- Williams, P. M. (2008). Dust formation by colliding-wind binaries. 33, 71–76 (cited on page 90).
- Williams, P. M. & van der Hucht, K. A. (2015). The colliding-wind WC9+OB system WR 65 and dust formation by WR stars, 275–278 (cited on page 91).
- Williams, P. M., van der Hucht, K. A., Pollock, A. M. T., Florkowski, D. R., van der Woerd, H. & Wamsteker, W. M. (1990). Multi-frequency variations of the Wolf-rayet system HD 193793 - I. Infrared, X-ray and radio observations. *Monthly Notices of the Royal Astronomical Society*, 243, 662–684 (cited on page 95)
ADS Bibcode: 1990MNRAS.243..662W.
- Williams, P. M., van der Hucht, K. A., Thé, P. S. & Bouchet, P. (1990). A Dust Shell around the Early Type Wolf-Rayet Star WR:19. *Monthly Notices of the Royal Astronomical Society*, 247, 18P (cited on page 75).
- Zubko, V. G. (1998). On the physical model of dust around Wolf-Rayet stars. *Monthly Notices of the Royal Astronomical Society*, 295(1), 109–118. <https://doi.org/10.1046/j.1365-8711.1998.29511348.x> (cited on page 57)

Software Citations

- Astropy Collaboration, Price-Whelan, A. M., Sipőcz, B. M., Günther, H. M., Lim, P. L., Crawford, S. M., Conseil, S., Shupe, D. L., Craig, M. W., Dencheva, N., Ginsburg, A., VanderPlas, J. T., Bradley, L. D., Pérez-Suárez, D., de Val-Borro, M., Aldcroft, T. L., Cruz, K. L., Robitaille, T. P., Tollerud, E. J., ... Astropy Contributors. (2018, September). *The astropy project: Building an open-science project and status of the v2.0 core package*. arXiv: 1801.02634 [astro-ph.IM]. <https://doi.org/10.3847/1538-3881/aabc4f>. (Cited on page 107)

OTHER CITATIONS

- Astropy Collaboration, Robitaille, T. P., Tollerud, E. J., Greenfield, P., Droettboom, M., Bray, E., Aldcroft, T., Davis, M., Ginsburg, A., Price-Whelan, A. M., Kerzendorf, W. E., Conley, A., Crighton, N., Barbary, K., Muna, D., Ferguson, H., Grollier, F., Parikh, M. M., Nair, P. H., ... Streicher, O. (2013, October). *Astropy: A community Python package for astronomy*. arXiv: 1307.6212 [astro-ph.IM]. <https://doi.org/10.1051/0004-6361/201322068>. (Cited on page 107)
- Harris, C. R., Millman, K. J., van der Walt, S. J., Gommers, R., Virtanen, P., Cournapeau, D., Wieser, E., Taylor, J., Berg, S., Smith, N. J., Kern, R., Picus, M., Hoyer, S., van Kerkwijk, M. H., Brett, M., Haldane, A., del Río, J. F., Wiebe, M., Peterson, P., ... Oliphant, T. E. (2020). Array programming with NumPy. *Nature*, 585(7825), 357–362. <https://doi.org/10.1038/s41586-020-2649-2> (cited on page 106)
- Hunter, J. D. (2007). Matplotlib: A 2D graphics environment. *Computing in Science & Engineering*, 9(3), 90–95. <https://doi.org/10.1109/MCSE.2007.55> (cited on page 107)
- Tange, O. (2021, September). *GNU parallel 20210922 ('vindelev')*. <https://doi.org/10.5281/zenodo.5523272>. (Cited on page 106)

Other Citations

- Childs, H., Brugger, E., Whitlock, B., Meredith, J., Ahern, S., Pugmire, D., Biagas, K., Miller, M., Harrison, C., Weber, G. H., Krishnan, H., Fogal, T., Sanderson, A., Garth, C., Bethel, E. W., Camp, D., Rübel, O., Durant, M., Favre, J. M. & Navrátil, P. (2012, October). *VisIt: An end-user tool for visualizing and analyzing very large data*. (Cited on page 106).
- Soulain, A., Millour, F., Lopez, B., Matter, A., Lagadec, E., Carbillet, M., Camera, A., Lamberts, A., Langlois, M., Milli, J., Avenhaus, H., Magnard, Y., Roux, A., Moulin, T., Carle, M., Sevin, A., Martinez, P., Abe, L. & Ramos, J. (2018, June 22). *The SPHERE view of Wolf-Rayet 104*. arXiv: 1806.08525 [astro-ph]. Retrieved October 23, 2018, from <http://arxiv.org/abs/1806.08525>. (Cited on page 96)